2018

Contributions to Tsunami Detection by High Frequency Radar

Patrick J. Moran
University of Rhode Island, patrick_moran@my.uri.edu

CONTRIBUTIONS TO TSUNAMI DETECTION BY HIGH FREQUENCY RADAR

BY

PATRICK J. MORAN

A THESIS SUBMITTED IN PARTIAL FULFILLMENT OF THE

REQUIREMENTS FOR THE DEGREE OF

MASTER OF SCIENCE

IN

OCEAN ENGINEERING

UNIVERSITY OF RHODE ISLAND

2018

MASTER OF SCIENCE THESIS

OF

PATRICK J. MORAN

APPROVED:

Thesis Committee:

Major Professor Stéphan Grilli

Annette Grilli

Jason Dahl

Tetsu Hara

Nasser H. Zawia

DEAN OF THE GRADUATE SCHOOL

UNIVERSITY OF RHODE ISLAND

2018

ABSTRACT

This thesis is comprised of three separate manuscripts, detailing recent work into the detection of Tsunamis in coastal waters using High Frequency (HF) coastal radar systems. The overarching focus of the three manuscripts is the development and performance analysis of a tsunami detection technique from using synthetic radar data and synthetic, simulated tsunamis, to using recorded raw radar data combined with synthetic tsunamis, and the comparison of this work against another published method. The proposed detection algorithm tests for fluctuations in correlations of HF measurements of the sea surface, and has been named the "Time Correlation Algorithm" or TCA. The first two manuscripts are published journal papers, with the third currently being edited for submittal.

Tsunami detection by High Frequency Radar beyond the continental shelf II: Extension of time correlation algorithm and validation on realistic case studies

The first manuscript covers work based on a realistic case study, a simulated radar signal and two simulated tsunamis are used in order to validate the operation of the TCA modeled on an existing radar system in Tofino Canada and realistic tsunami threats to the area. The TCA is defined as correlations between radar cells connected along an intersecting wave ray, shifted in time by the long wave propagation time along the ray, c equal to $\sqrt{gh}$. The correlation is taken over a long time window, on the order of 10-15 minutes, in order to capture a meaningful portion of the tsunami wave, and average out the correlation values of smaller period waves. The correlation in the radar signal between cells is expected to be a near uniform value of one when no tsunami is present, this is due to the general lock of other naturally occurring oceanic waves or patterns with the same period of tsunamis. The first synthetic tsunami was modeled on a M_w 9.1 far-field source

based in the Semidi Subduction Zone (SSZ). It was demonstrated that the TCA is able to detect extremely small currents, less than 10 cm/s, in the presence of strong, random background currents, up to 35 cm/s. The second was a near field submarine mass failure (SMF) tsunami located just off of the coast of the modeled radar station.

Tsunami detection by High Frequency Radar in British Columbia: performance assessment of the Time-Correlation Algorithm for synthetic and real events

Manuscript two continues the development of the TCA, by replacing the simulated radar signal with recorded radar data from the WERA station in Tofino CA which the simulated signal was based on, and expanding to a third tsunami source. The new tsunami source is a potential meteo-tsunami which occurred on October 14, 2016, and provides an opportunity or detection of a real tsunami event (albeit in an offline *a posteriori* analysis). When applied to the raw data it was found that the radar signal itself exhibited a high level of self correlation, thought to be an artifact from the signal processing software; namely range-gating and beam forming. A new slightly modified TCA was therefore developed which contrasts the average correllation along a portion of a wave ray against the correlation of the same portion, taken one hour prior. This modified version of the TCA demonstrated detection of the simulated SSZ tsunami and SMF tsunami using the recorded radar signal from several different days, representative of using varying oceanic and meteorological conditions to test the robustness of the algorithm. An initial detection threshold for the method was also determined, and using a few days of data the method for determining a more robust confidence in detection was demonstrated. The major conclusions are the function of the TCA on real data, and with a variety of different, realistic threats to the area.

Tsunami Detection by High Frequency Radar: Comparison of Time Correlation Algorithm and Q-Factor Algorithm

The final manuscript compares the TCA with another published detection method, the "Q-Factor" algorithm. The Q-Factor uses the measurements recorded by coastal radar stations in the from of traditionally radially inverted currents. These currents are derived from the Doppler spectra of the backscattered radar signal. By using an empirically derived pattern recognition algorithm, the Q-Factor tests for fluctuations in surface currents across bathymetry bands indicative of a tsunami. In this manuscript the raw radar data and simulated tsunami sources used to test the TCA are again used to provide a direct comparison of the two. Additionally several aspects from the TCA are borrowed to generate a modified Q-Factor and test whether a hybridization of the two methods results in any performance improvements. Its concluded that the TCA operates more reliably over a variety of meteorological, oceanic, and operating conditions, although a more thorough analysis (especially of signal quality) must be completed before true conclusions can be drawn. The Q-Factor is also unable to detect the SMF, demonstrating an important limitation of the system, something that must be taken into account with local threats when considering an algorithm to be used in a specific area.

ACKNOWLEDGMENTS

I would like first and foremost to thank my major professor, Dr. Stéphan Grilli for taking me on as a master's student and providing me with the opportunity to further my education. Your guidance throughout my work on this project, starting from an undergraduate in senior capstone and continuing on as a graduate student has helped myself further my abilities as an Engineer, a Scientist, and a person. I would also like to extend a very special thank to Dr. Charles Guérin, with whom I worked verily closely with on this project and have learned a great deal from. Thank you to my committee members, Dr. Annette Grilli, Dr. Jason Dahl, and Dr. Tetsu Hara, all of whom I have either attended class with or developed a personal relation with during my time at URI and I am very thankful for this.

I would also like to thank Dr. Tania Insua and Ocean Networks Canada for support in this project, and Dr. Grilli for you tireless work securing these funds. Further thanks to Dr. Thomas Helzel for providing the software used to process the radar data, without which this project would have been impossible.

To all of my close friends and fellow students with whom I have laughed with, worked with, and were helped by throughout my collegiate career, endless thanks. Especially Chris, Cam, Wendy, Scott, Lauren, Fatima, Boma, Matt, and Chris. Thank you also, Gail Paolino, for all of your help and guidance through the mind boggling administrative processes.

A special thank you to Adam, Ken and Eugene, all of whom have provided support and guidance in my young professional career.

Finally the warmest of thank you's to my parents and brothers, your unwavering support, belief, and encouragement have lead me to become who I am today.
- Patrick J. Moran Jr.

PREFACE

This thesis, submitted in partial fulfillment of the requirements for the degree of Master of Science in Ocean Engineering was assembled in manuscript format. A total of three manuscripts combine for the thesis. A brief overview of each manuscript follows, including the candidate's contributions, and relevant publication information.

Manuscript 1 was published in Pure and Applied Geophysics in 2017 (Doi 10.1007/s00024-017-1619-6). Manuscript formatting has been changed in order to meet university guidelines, however the content is unchanged. P. Moran aided in the generation of several figures and responses to edits from the initial submission, as well as in the generation of new wave rays for algorithm testing. Existing code was built upon during this work. Additionally sensitivity to a variety of parameters, including wave ray source direction, and cell spacing along wave rays was tested.

Manuscript 2 has been accepted for publication in Ocean Dynamics as of September 2017. Again formatting has been changed in accordance with university guidelines, however the content is unchanged. Using previous simulations P. Moran aided in the analysis of and application of the detection algorithm to raw radar data. Sensitivity to a variety of parameters, such as detection range, cell spacing, and integration time were also inspected.

Manuscript 3 is being prepared for submission to the Natural Hazards Journal. Formatting will be changed from university guidelines to conform with that required by the journal. P. Moran developed a suite of code for the operation of the Q-Factor, including initial setup in an arbitrary location with arbitrary radar parameters, to testing the method. Code was built upon from existing examples from the work in the first manuscripts.

TABLE OF CONTENTS

Page

LIST OF FIGURES

Figure **Page**

LIST OF TABLES

MANUSCRIPT 1

Tsunami detection by High Frequency Radar beyond the continental shelf II: Extension of time correlation algorithm and validation on realistic case studies

Published in Pure and Applied Geophysics, 2017. DOI

10.1007/s00024-017-1619-6

By

Stéphan T. Grilli[1], Charles-Antoine Guérin[2], Micheal Shelby [1], Annette R. Grilli [1], Patrick Moran [1], Samual Grosdidier [3], and Tania L. Insua 4

Abstract

In past work, tsunami detection algorithms (TDAs) have been proposed, and successfully applied to offline tsunami detection, based on analyzing tsunami currents inverted from High-Frequency (HF) radar Doppler spectra. With this method, however, the detection of small and short-lived tsunami currents in the most distant radar ranges is challenging due to conflicting requirements on the Doppler spectra integration time and resolution. To circumvent this issue, in Part I of this work, we proposed an alternative TDA, referred to as Time Correlation (TC) TDA, that does not require inverting currents, but instead detects changes in patterns of correlations of radar signal time series measured in pairs of cells located along the main directions of tsunami propagation (predicted by geometric optics theory); such correlations can be maximized when one signal is time-shifted by the pre-computed long wave propagation time. We initially validated the TC-TDA based on numerical simulations of idealized tsunamis in a simplified geometry. Here, we further develop, extend, and apply the TC algorithm to more realistic tsunami case studies. These are performed in the area West of Vancouver Island, BC, where Ocean Networks Canada recently deployed a HF radar (in Tofino, BC), to detect tsunamis from far- and near-field sources, up to a 110 km range. Two case studies are considered, both simulated using long wave models: (i) a far-field seismic, and (ii) a near-field landslide, tsunami. Pending the availability of radar data, a radar signal simulator is parameterized for the Tofino HF radar characteristics, in particular its signal-to-noise ratio with range, and combined with the simulated tsunami currents to produce realistic time series of backscattered radar signal from a dense grid of cells. Numerical experiments show that the arrival of a tsunami causes a clear change in radar signal correlation patterns, even at the

most distant ranges beyond the continental shelf, thus making an early tsunami detection possible with the TC-TDA. Based on these results, we discuss how the new algorithm could be combined with standard methods proposed earlier, based on a Doppler analysis, to develop a new tsunami detection system based on HF radar data, that could increase warning time. This will be the object of future work, which will be based on actual, rather than simulated, radar data.

1.1 Introduction

Major tsunamis can be enormously destructive and cause large numbers of fatalities along the world's increasingly populated and developed coastlines (Ioualalen et al., 2007; Grilli et al., 2013; Kânoğlu et al., 2015). While the brunt of the tsunami impact cannot be easily attenuated, loss of life, however, can be mitigated or even eliminated by providing early warning to coastal populations. Warnings can be issued based on the early detection and assessment of the mechanisms of tsunami generation (e.g., seismicity) as well as detection of tsunami waves as soon as possible after generation. The latter is particularly important when the tsunami source is located nearshore and thus its propagation time to the coast is short. This is the case, for instance, for: (i) co-seismic tsunamis generated in nearshore subduction zones (SZ; e.g., Andaman SZ, Japan Trench, Puerto Rico Trench, Cascadia SZ,...) (Titov et al., 2005; Grilli et al., 2007; Grilli et al., 2010; Grilli et al., 2013; Cherniawsky et al., 2007; Tang et al., 2016); (ii) submarine mass failures (SMFs) that can be triggered on or near the continental shelf slope by moderate seismic activity [e.g., (Fine et al., 2005; Tappin et al., 2008; Grilli et al., 2015)]; or (iii) meteo-tsunamis generated on continental shelves by fast moving elongated low pressure systems (e.g., derechos) (Thomson et al., 2009; Lipa et al., 2014).

For nearshore sources of all types, the detection of offshore propagating tsunamis can be made in deep water at bottom-mounted pressure sensors (so-called

DART buoys), and based on this a warning can be issued for far-field locations [e.g., (Bernard and Titov, 2016)]; and even for local communities if local DARTs are available (Tang et al., 2016). The detection of onshore propagating tsunamis from nearshore sources can similarly be made over the continental shelf using bottom pressure sensors or tide gauges. These instruments, however, only measure the tsunami locally (i.e., they make a point-based measurement) and may not survive the impact of large tsunamis. Additionally detection made at such sensors often takes place too late (i.e., too close to shore) to be useful in early warning systems; this means that seismic-, SMF-, or meteo-tsunamis from nearshore sources will often be detected too late. When an earthquake is the triggering mechanism, an early warning can still be issued based on detecting seismic waves, which travel much faster than the tsunami, particularly in shallow water and, based on these, on estimating the earthquake parameters and the likelihood for tsunami generation. But for non-seismically induced nearshore SMF- or meteo-tsunamis, a timely warning (i.e, sufficiently before the tsunami impacts the coast) requires a detection as soon as possible after wave generation. This is particularly true when the continental shelf is narrow, such as along the West coast of the US and Canada. In the latter area, for instance, (Anderson and Gow, 2004) and (Anderson, 2015) concluded that there is a strong need to deploy new sensing technologies and, based on these, to implement early warning systems for tsunamis from local sources that could impact the coast of British Columbia. This in part motivated the present work, in which we study and model tsunami detection by High Frequency (HF) radars.

Nearly 4 decades ago, (Barrick, 1979) proposed to use shore-based HF radars to detect incoming tsunami waves. But it is only recently that these ideas have been further developed and, in particular, supported by numerical sim-

ulations [e.g., (Lipa et al., 2006; Heron et al., 2008; Dzvonkovskaya et al., 2009; Gurgel et al., 2011)], and actual HF radar measurements, such as made during the large Tohoku 2011 tsunami in: (i) Japan (Hinata et al., 2011; Lipa et al., 2011; Lipa et al., 2012a); (ii) Chile (Dzvonkovskaya, 2012); and (iii) Hawaii (Benjamin et al., 2016). When these measurements were made, however, no real time Tsunami Detection Algorithms (TDAs) were operational in the radar systems, and tsunami currents were only identified in *a posteriori* analyses of the recorded radar data. More recently, weaker tsunamis (Lipa et al., 2012b) and even some of non-seismic origin (Lipa et al., 2014) were similarly detected in *a posteriori* re-analyses of radar data, that identified the tsunami current signature. According to a recent review by (Lipa et al., 2016), 21 cases of offline detections of tsunamis based on radar data have been made since 2011.

The standard method used for estimating ocean surface currents from HF radar data, whether tsunami generated or otherwise, is based on the Doppler shift that they induce on the radar signal, proportionally to their magnitude. Time series of radial surface currents (i.e., projected on the radar line-of-sight) are typically "inverted" this way over a grid of radar cells covering a sweep area of tens to hundreds of km in the radial direction (standard cell sizes are one to a few km in each direction). TDAs based on radial surface currents inverted by HF radars have been proposed in some of the studies referred to above, which identify the oscillatory nature of tsunami currents in space and/or in time, and some are operational at a few radar locations. These will be referred to in the following as "Doppler Method" (DM) TDAs.

To issue an early warning, it is desirable for such HF-radar-based TDAs to detect incoming tsunamis as far from shore as possible (i.e., at far-ranges). Typically, far-field coseismic tsunamis are long period waves (tens of min) with weak

currents in deep water (centimeters per second), whose magnitude gradually increases on the continental slope and shelf due to shoaling. Near-field SMF- or meteo-tsunamis, by contrast, may have larger currents from the onset, but are much shorter period waves (5-10 min). Based on these characteristics, the maximum range at which a DM-TDA can reliably detect a tsunami is function of two main factors:

1. The resolution of currents inverted from the radar Doppler spectrum is inversely proportional to the integration or windowing time T_w; thus, detecting weak currents requires using longer integration times. However, tsunami currents oscillate at the tsunami period T_t, which requires $T_t \gg T_w$; otherwise, increasing T_w to detect weak currents at distant ranges will make the time-averaged tsunami currents increasingly small as to become undetectable. For typical values of T_w used in HF radars (say 5-10 min), this requirement can more easily be met for the longer period coseismic tsunamis than for the shorter period SMF- or meteo-tsunamis.

2. To reliably detect surface currents, the radar signal-to-noise ratio (SNR) must be sufficiently large; however, for a given radar system, the SNR decreases with range, which can be compensated to some extent by increasing T_w (Forget, 2015); this, however, conflicts with the earlier requirement leading to a practical limit to the maximum tsunami detection range.

Hence, in general, unless the continental shelf is wide and shoaling increases current magnitude, it is difficult using a DM-TDA to detect weak and short-lived tsunami currents in the far-ranges, where the SNR is low; however, this is typically required to issue an early warning (i.e., detecting incoming tsunami currents in deeper water when they are only a few cm/s). [Note, that (Lipa et al., 2012a) reported the detection of weak tsunami currents, on the order of 5-10 cm/s, in an actual case,

Grid	SW corner (Lat/Lon)	N_x x N_y grid cells	Resolution (actual)	Resolution ($\sim$ m)
G0	(10.00,-180.00)	1950 x 1560	2 min (S)	3,600
G1	(44.00,-129.01)	700 x 600	0.6 min (S)	1,089
G2	(46.99, -127.52)	766 x 900	360 m (C)	360
G3	(48.25, -126.90)	1800 x 1200	90 m (C)	90

Table 1.1: Parameters of nested grids used in FUNWAVE-TVD/NHWAVE simulations, in which G0 is a spherical (S) grid with 100 km thick sponge layers on the outside boundary, and G1, G2 and G3 are spherical (S) or Cartesian (C) grids centered on the WERA radar sweep area in Tofino, BC (Figs. 2.1a and 1.2a). G1-G3 simulations are performed by one-way coupling.

but this was in the near-ranges and using a relatively long integration time (4 min).]

To overcome this limitation, particularly for near-field SMF- and meteo-tsunamis, (Grilli et al., 2016) proposed a new type of TDA that does not require inverting currents from radar Doppler spectra, but instead is based on observing changes in patterns of correlations between time series of radar signal measured at pairs of radar cells; hence this is referred to as "Time Correlation" (TC) TDA. To maximize such correlations: (i) the pairs of cells are selected along the same wave ray, i.e.,"an envelope of instantaneous directions of tsunami propagation"; and (ii) one of the time series is time-shifted by the tsunami propagation time along the ray, from the first to the second cell. Assuming linear long wave and geometric ray theories, both wave rays and tsunami propagation times are only depth-dependent; hence, these can be pre-calculated for a given radar sweep area of known bathymetry and for a variety of incident tsunami directions. As we shall demonstrate in applications of the TC-TDA, a change in signal correlation pattern from flat to peaked will indicate the arrival of a tsunami, since no other geophysical phenomenon can be responsible for an oscillatory current propagating at the long wave speed from very deep to shallow water. It should be stressed that, unlike a DM-TDA, the TC-TDA does not provide a direct estimate of tsunami magnitude,

but merely indicates that a tsunami is approaching; hence, an operational TDA system would likely combine both types of algorithms (this will be elaborated on in the paper discussion).

(Grilli et al., 2016) validated the TC-TDA for idealized tsunami wave trains propagating over a simplified seafloor bathymetry, in a direction normally incident to shore. Here, to more realistically assess its performance, the algorithm is extended and applied to both arbitrary bathymetry and realistic tsunami wave trains from far- and near-field sources. The selected study area is the the West Coast of Vancouver Island, BC (Canada), where Ocean Networks Canada (ONC) recently installed a shore-based 13.5 MHz WERA HF radar (in Tofino (TF), BC), which has a 85-110 km measuring range depending on ocean/atmospheric conditions (Fig. 2.1b). Given a proper TDA, this radar could provide an early warning of tsunami arrival, in combination with other instruments that are part of the operational hydro-physical observatory NEPTUNE. This observatory, which connects instruments deployed on the seafloor off of Tofino, via a network of fibre optics, has already been successful at detecting the arrival of far-field tsunamis (Thomson et al., 2011; Rabinovich et al., 2013; Fine et al., 2013).

The TF radar became operational in April 2016, but no data was available when most of the present work was carried out. Hence, similar to (Grilli et al., 2016), in this paper we use a radar simulator to simulate the radar signal as a function of computed tsunami currents, but here the simulator is parameterized for the characteristics and over the same sweep area and cells as the Tofino WERA HF radar (Fig. 2.1b); additionally, late in the project, some radar data was obtained, based on which realistic values of the SNR were estimated and used in the simulator. [The use of actual radar signal modified by superposing a simulated tsunami current will be addressed in future work (Guérin et al., 2017).]

Tsunami currents produced by two realistic tsunami sources (a far-field coseismic and a near-field SMF source) are modeled using state-of-the-art long wave models, and wave rays are computed for a number of incident directions by solving the geometric optic equation; these simulations are performed using high-resolution bathymetry in the radar sweep area.

In the following, we first detail the selection of the two tsunami sources and simulations of their tsunami generation and propagation, as well as the computation of tsunami wave rays and travel times. We then summarize the principles of estimation of ocean surface currents by HF radars and present the equations and calibration of the radar signal simulator. Finally, we report on the application of the DM- and TC-TDAs to the detection of both tsunamis in the selected area.

1.2 Selection of tsunami sources and simulations of tsunami currents

The performance of the TC-TDA is assessed by simulating tsunami-induced currents over the TF radar sweep area (Fig. 2.1b), for two realistic tsunami sources. Once space-averaged over each radar cell, these currents are used in the HF radar simulator, parameterized for the characteristics of the Tofino radar, and the TDA is applied to simulated time series of radar signal.

Due to the high tsunami hazard in this area, there have been many studies performing simulations of far- and near-field historical [e.g., Alaska 1964, (Myers and Baptista, 2001)] or future hypothetical [Cascadia SZ; e.g., (Whitmore, 1993; Cherniawsky et al., 2007; Fine et al., 2008; Insua et al., 2015)] tsunamis off of Vancouver Island, but these were mostly from large coseismic sources. Although this would likely cause the worst case scenario, we did not select a near-field Cascadia SZ source in this work, because it would be triggered very close to shore and associated with large seismicity, hence providing immediate warning of its occurrence. Instead, we selected a large far-field seismic

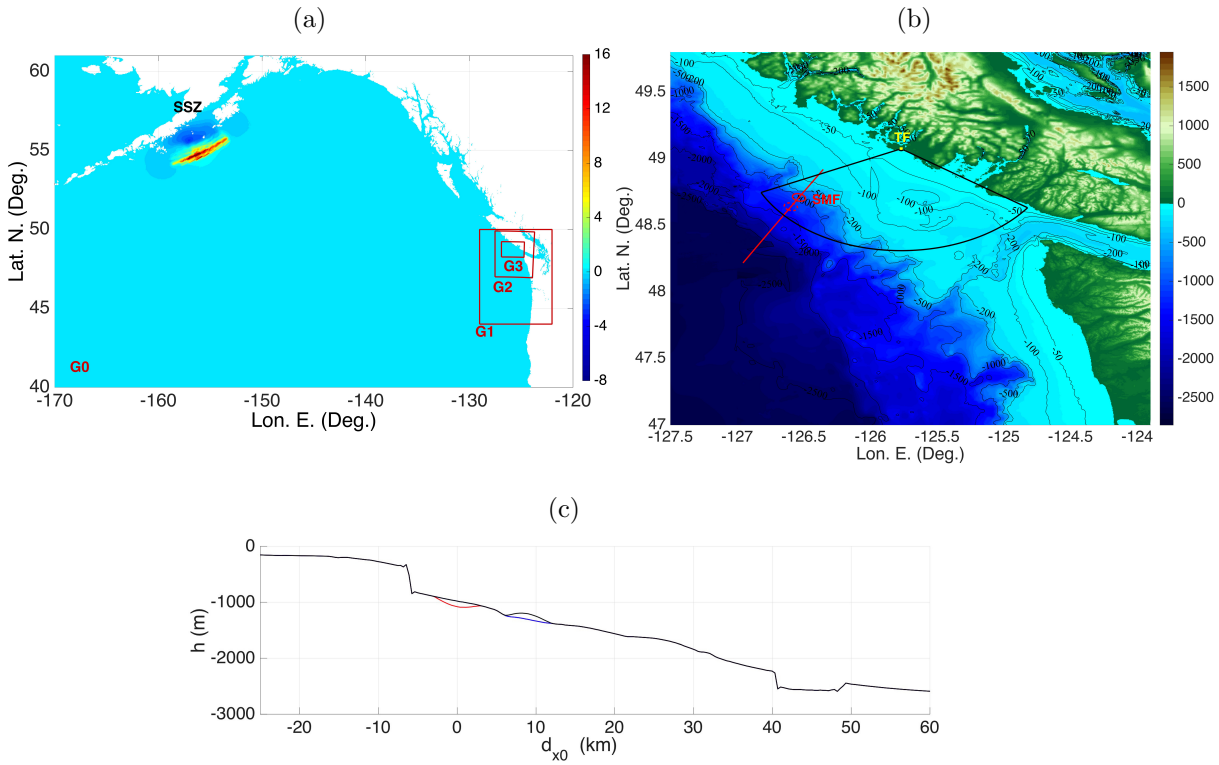

Figure 1.1: (a) Zoom-in on 2 arc-min grid G0 footprint in Pacific Ocean, with initial surface elevation (color scale in meter) of M_w 9.1 SAFRR seismic source in the Semidi Subduction Zone (SSZ); red boxes mark boundaries of FUNWAVE-TVD/NHWAVE nested grids, off of Vancouver Island, BC: G1 (0.6 arc-min), G2 (360 m), and G3 (90 m) (Table 1.1). (b) Zoom-in on area of grid G2 off of the WERA HF radar deployment site in Tofino (TF; ■); (black line) WERA radar typical measurement/sweep area (85 km radius); color scale and black contours are bathymetry (< 0) and topography (> 0) in meter; the solid red ellipse ($w = 8$ by $b = 6$ km) and transect mark initial footprint and direction of motion (209 deg. clockwise from N) of a $V_s = 1.68$ km^3 SMF tsunami source (at 48.70822 Lat. N. and -126.53669 Lon. E.), and the dashed ellipse marks its final location ($s_f = 9$ km downslope). (c) (black line) Bathymetric transect in direction of SMF motion, with: (red line) initial and (blue line) final SMF cross-sections (maximum thickness: $T = 0.1$ km); distance d_{x0} is measured from the SMF initial center of mass location.

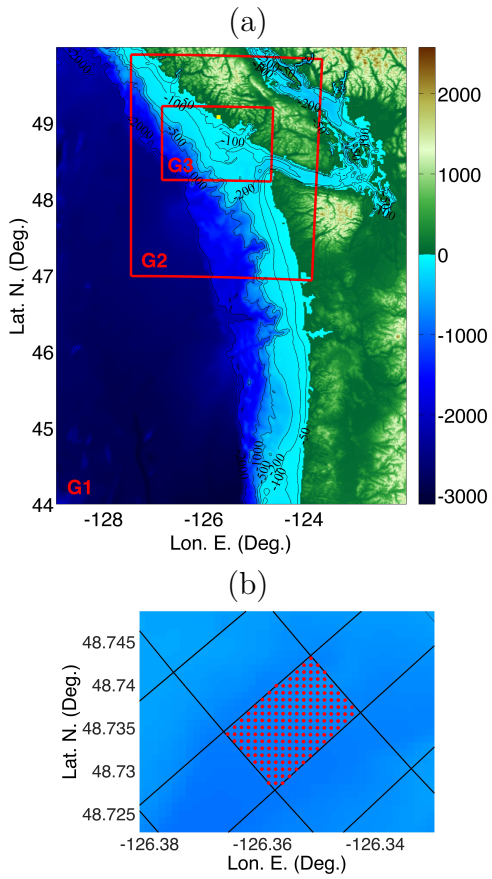

Figure 1.2: (a) Footprints and bathymetry of nested grids G1, G2 and G3 used in FUNWAVE-TVD/NHWAVE simulations (Fig. 2.1a; Table 1.1) centered on radar location at Tofino, BC (■). (b) Zoom-in onto a few radar cells in sweep area (Figs. 2.1b, 1.8), with marked locations (•) of FUNWAVE-TVD's or NHWAVE's G3 grid cells contained within one radar cell. [Color scale and black contours are bathymetry (< 0) and topography (> 0) in meter.]

source in the Semidi Subduction Zone (SSZ; Fig. 2.1a), with the same magnitude M_w 9.1 as the Tohoku 2011 event, which was designed by the SAFRR (Science Application for Risk Reduction) group to cause maximum impact in northern California (Kirby et al., 2013b). Even moderate local earthquakes from the Cascadia SZ could trigger many SMFs on the continental slope and shelf break (McAdoo and Watts, 2004). In recent work, (Yelisetti et al., 2014) in fact identified sizable paleo-SMFs (with one of up to 0.33 km^3 volume in 2,300 m depth)

that failed as rigid slumps on the continental slope off of TF, whose triggering may have been facilitated by the presence of gas hydrates. Hence, our second tsunami source is a near-field SMF located on the continental slope, 70 km off of Tofino (Fig. 2.1b), whose siting and parameters are detailed below.

1.2.1 Simulations of tsunami generation and propagation

Far-field seismic source

The initial surface elevation of he M_w 9.1 SSZ source, shown in Fig. 2.1a, was obtained from (Kirby et al., 2013b) (source labeled "KirbyAlaskaPeninsulaTotal"; see http://atom. giseis.alaska.edu). Tsunami propagation for this source is simulated with the two-dimensional (2D) model FUNWAVE-TVD, a Boussinesq long wave model with extended dispersive properties, which is fully nonlinear in Cartesian grids (Shi et al., 2012) and weakly nonlinear in spherical grids (Kirby et al., 2013a). This model was efficiently parallelized for use on a shared memory cluster (over 90% scalability is typically achieved), which allows using large grids (such as here the G0 grid shown in Fig. 2.1a, which has over 3 million cells; see details below). FUNWAVE (its earlier version) and FUNWAVE-TVD have been widely used to simulate tsunami case studies [e.g., (Grilli et al., 2007; Grilli et al., 2010; Grilli et al., 2013; Grilli et al., 2015; Ioualalen et al., 2007; Tappin et al., 2008; Tappin et al., 2014; Abadie et al., 2012; Tehranirad et al., 2015)]. Since 2010, the authors have applied this model and related methodology to compute tsunami inundation maps along the US East Coast, under the auspice of the US National Tsunami Hazard Mitigation Program (NTHMP) (see, e.g., work and maps at: http://chinacat.coastal.udel.edu/nthmp.html). Both spherical and Cartesian versions of FUNWAVE-TVD have been validated through rigorous benchmarking, for both the prediction of nearshore surface elevations and currents, and

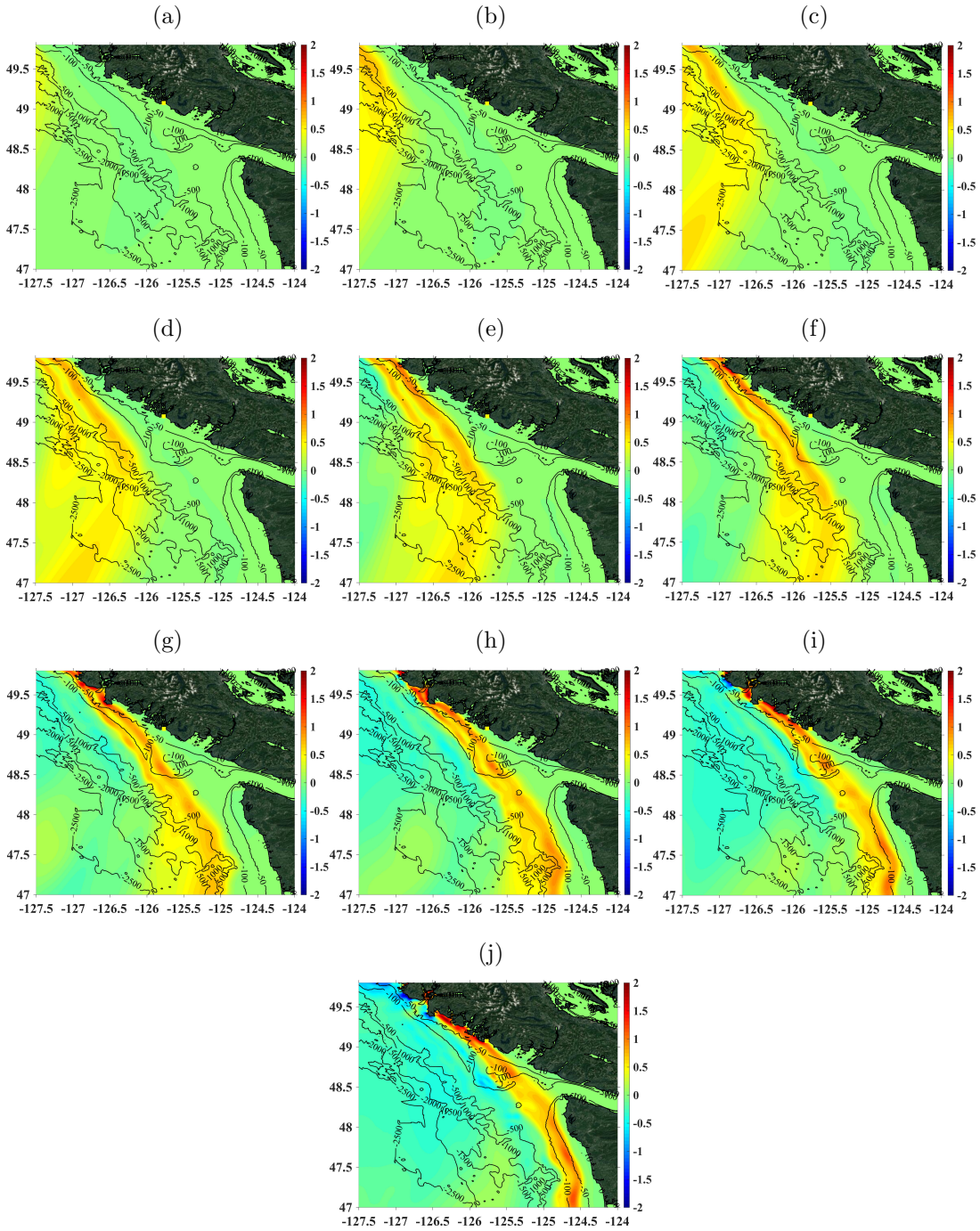

Figure 1.3: Instantaneous surface elevations (color scale in meter) simulated in grid G2 off of Tofino (■) with FUNWAVE-TVD, for M_w 9.1 SSZ source (Fig. 2.1a), at $t =$ (a) 5400 (1h30'); (b) 5700 (1h35'); (c) 6000 (1h40'); (d) 6300 (1h45'); (e) 6600 (1h50'); (f) 6900 (1h55'); (g) 7200 (2h); (h) 7500 (2h5'); (i) 7800 (2h10'); and (j) 8100 s (2h15').

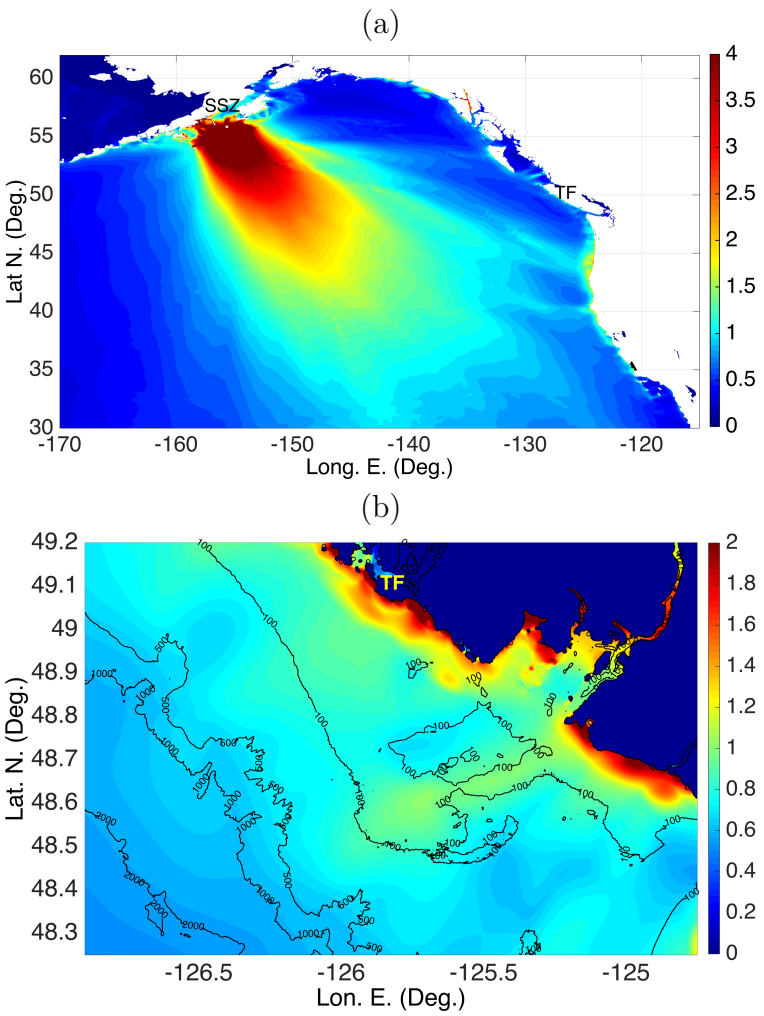

Figure 1.4: Maximum surface elevation (color scale in meter) during simulations with FUNWAVE-TVD of M_w 9.1 SSZ source (Fig. 2.1a), in grid: (a) G0 (only the zoomed-in area is shown); and (b) G3 (TF marks the HF radar deployment site in Tofino, BC); labeled black lines are depth contours in meter.

and approved for NTHMP work (Tehranirad et al., 2011; Horrillo et al., 2014; Lynett and thirty-seven alii, 2017). Following the standard practice, simulations of seismic tsunami sources are initialized with an initial surface elevation and no-velocity.

Four levels of nested grids are used in the simulations, with the coarser one G0, a 2 arc-min resolution spherical coordinate grid, covering a large area of the Pacific Ocean, and G1, G2, and G3, a series of spherical and Cartesian nested grids centered on Tofino, BC, with increasing resolution of 0.6 arc-min ($\sim$1,089 m), 360 m, and 90 m, respectively (Figs. 2.1a and 1.2a; Table 1.1). To eliminate reflection, 100 km thick sponge layers are specified along the outside boundary of grid G0. Simulations in finer nested grids are then performed by one-way coupling. In this method, time series of surface elevations and depth-averaged currents are computed for a large number of stations/numerical wave gauges defined within a coarser grid, along the boundary of the finer grid used in the next level of nesting. Computations are fully performed in the coarser grid and then restarted in the finer grid using the station time series as boundary conditions. As these include both incident and reflected waves computed in the coarser grid, this method closely approximates open boundary conditions. It was found that a 3-4 reduction in nested grid size yielded good accuracy in tsunami simulations, which is the case for grids used here (Table 1.1).

Bathymetric/topographic data for the 2 arc-min resolution G0 and 0.6 arc-min G1 grid is interpolated from NOAA's 1 arc-min ETOPO-1 data. Bathymetry for the 270 m and 90 m resolution grids (G2 and G3) is based on the 3 arc-sec data provided for the coast of BC by NOAA's Marine Geology and Geophysics (MGG), wherever available. This higher-resolution data was also used in grids G0 and G1, instead of ETOPO-1 data, in the area overlapping with grid G2. Another MGG

3 arc-sec dataset (the Northwest Pacific data set) is used for areas facing the US coast not covered by the BC bathymetry. Since the MGG BC dataset only includes bathymetry, topography for grids G2 and G3 is based on ETOPO-1 data, which clearly is too coarse to accurately simulate coastal inundation. This, however, is acceptable, since the present work is not concerned with predicting tsunami inundation and runup, but instead focuses on detecting the tsunami offshore, at a significant distance away from the shoreline.

Fig. 1.3 shows snapshots of free surface elevations computed in grid G2, for the SSZ source, from $t = 5400$ to 8100 s (1h30' to 2h15'), from the time when the tsunami starts entering the grid area to its impact on the TF shore. The incident tsunami arrives as a train of long-crested long period waves ($T_t \simeq 20 - 40$ min), which have already significantly refracted during their deep water propagation and continue to do so over the shelf slope and shelf proper, to become nearly perfectly aligned with bathymetric contours from a 100 m depth onward (Fig. 1.3e). Maximum surface elevations reach $\simeq$ 2 m nearshore; this is better seen in Fig. 1.4, which shows the envelopes of maximum surface elevation computed during simulations in grids G0 and G3. As anticipated for this SAFFR SSZ source, Fig. 1.4a shows that tsunami energy focuses on northern California and Oregon; but Fig. 1.4b also shows significant tsunami elevations near TF, with over 2 m predicted at the coast.

Near-field SMF source

Considering the bottom morphology and bathymetry of the continental slope (Fig. 2.1b), a realistic SMF source is sited in the same general area as identified by (Yelisetti et al., 2014) but, to trigger a more meaningful tsunami, in shallower depth and with a larger volume similar to that of the Goleta SMF (1.75 km^3) that occurred off of Santa Barbara, CA (Greene et al., 2005). The

SMF initial center of mass is located at 48.70822 Lat. N. and -126.53669 Lon. E. (i.e., about 70 km SW of TF), in depth $h_0 = 980$ m, and motion is assumed to occur in the direction of the steepest local slope, 209 deg clockwise from North. The maximum sediment thickness is set to $T = 0.1$ km, based on seismic profiles reported in (Yelisetti et al., 2014) and, following the methodology detailed in (Grilli et al., 2015), the SMF has a Gaussian-like geometry (shape factor $\epsilon = 0.717$), with an elliptical footprint of downslope length $b = 6$ km and cross-slope width $w = 8$ km (Fig. 2.1b); this leads to a volume $V_s = 1.7$ km^3. Fig. 2.1c shows the bathymetric transect through the direction of SMF motion, which has an average slope 2.1 deg. Assuming a rigid slump failure, with a pendulum-like center of mass motion: $s(t) = s_f\{1 - \cos(\pi t/t_f)\}/2$ [e.g., for details; (Grilli et al., 2015; Tappin et al., 2014)], realistic values are selected for the slump radius of rotation, $R = b^2/(8T) = 45$ km, runout $s_f = 9$ km, and time of failure $t_f = \pi((R/g)\,(\gamma + C_M)/(\gamma - 1))^{1/2} = 357.7$ s (for a bulk sediment density $\gamma = 2.1$, added mass coefficient $C_M = 1$, and gravitational acceleration $g = 9.81$ m/s^2) (Grilli et al., 2015). With these values, the SMF initial acceleration is $a_0 = 2\pi^2 s_f/t_f^2 = 0.35$ m/s^2 and maximum velocity $u_{max} = 2\pi s_f/t_f = 39.6$ m/s, which both are consistent with the expected values for such a SMF (Greene et al., 2005).

SMF tsunami generation is simulated with the three-dimensional (3D) non-hydrostatic model NHWAVE (Ma et al., 2012), which solves Euler equations in a horizontal Cartesian grid with boundary fitted (σ-coordinate) vertical layers. With 3 layers, this model provides a similar long-wave approximation as FUNWAVE-TVD; using more layers allows accurately modeling increasingly dispersive waves, such as generated by a small area SMF moving in deep water. The underwater slump time varying bottom geometry and kinematics are specified in NHWAVE

as bottom boundary conditions, which causes wave generation (Ma et al., 2012; Grilli et al., 2015). Similar to FUNWAVE-TVD, NHWAVE was efficiently parallelized and has been widely used to simulate SMF tsunami case studies [e.g., (Grilli et al., 2015; Tappin et al., 2014)], including for NTHMP, for which the model was also validated through benchmarking. As in earlier work, once the SMF stops moving, simulations of tsunami propagation are continued in nested grids using FUNWAVE-TVD, initialized with the last tsunami surface elevation and horizontal velocity components (at the required 0.531 times the depth) computed with NHWAVE. Here, SMF tsunami generation is simulated with NHWAVE in a grid with the same horizontal footprint as grid G2 (Fig. 2.1b), with 5 σ-layers in the vertical direction and 20 km wide sponge layers along the offshore boundary. Once generation is completed, simulations are continued with FUNWAVE-TVD in grid G2 and then by one-way coupling in grid G3 (Fig. 1.2a); Table 1.1).

Fig. 1.5 shows snapshots of free surface elevations computed for the SMF source in grid G2 from $t = 50$ to 900 s (50 s to 15 min), at which time the tsunami has propagated nearshore of TF, in nearly 50 m depth. As expected for a SMF, the tsunami initially takes the form of a dipole wave, with an offshore propagating elevation wave and an onshore propagating depression wave (Figs. 1.5a,b). As time increases, rebound waves are generated behind these leading waves, that gradually form a train of concentric, alternating, depression and elevation waves (Figs. 1.5c-h), whose amplitudes are much larger near the direction of SMF failure (transect in Figs. 2.1b,c); this strong directionality is expected for SMF tsunamis (Tappin et al., 2014; Grilli et al., 2015). The SMF tsunami waves are much shorter and shorter period ($T_t \simeq 5 - 10$ min) than the long period waves of the SSZ tsunami (Fig. 1.3). At larger times (Figs. 1.5i,j), the offshore propagating wave train starts being deflected by the wave-guiding effect caused by the shelf slope;

as shown by (Grilli et al., 2015) for the US East Coast, some of these waves would eventually propagate eastward and westward to impact other parts of the coast. By contrast, the onshore propagating wave train, similar to the SSZ tsunami, increasingly refracts over the shallow continental shelf and aligns itself with the local bathymetric contours, to approach TF as a nearly shore-parallel long-crested wave train. While the maximum SMF tsunami elevation (or depression) is much greater than 2 m near the source, due to directional energy spreading, it reduces to 0.5-1 m at $t = 900$ s (15 min), when approaching TF.

1.2.2 Tsunami wave rays and travel times based on geometric optics

Wave rays are contours materializing the instantaneous directions of tsunami propagation or wavenumber vectors, $\boldsymbol{k_t}(x, y) = (k_{tx}, k_{ty}) = k_t\,(\cos\phi_t, \sin\phi_t)$ (with ϕ_t the local direction of propagation with respect to the x axis, $k_t = \mid \boldsymbol{k_t} \mid = 2\pi/L_t$, and L_t the characteristic tsunami wavelength). The principle of the TC-TDA proposed by (Grilli et al., 2016) is to observe changes in pattern of time correlations of radar signal between pairs of radar cells located along the same wave ray, shifted in time by the tsunami propagation time between these cells. In the radar simulator, the radar signal is computed based on time series of tsunami currents simulated as detailed above and spatially averaged over each radar cell. Regarding wave rays, while tsunami surface elevations simulated in the propagation model (Figs. 1.3, 1.5) could also be used to identify wave rays (i.e., as envelopes of directions $\boldsymbol{k_t}$ normal to wave crests/troughs, or local direction of tsunami current), this is not straightforward to do. Earlier work, however, has shown ((Tehranirad et al., 2015); and this will be confirmed below) that wave rays computed based on the simplified geometric optics equation are accurate enough, and as it is much simpler to solve this equation as a function of bathymetry, it will be used here to compute wave rays.

Geometric optics assumes that wave propagation over a varying bathymetry $h(x, y)$ is only governed by refraction, leading to the eikonal equation. For linear long waves, which is a good approximation for tsunamis away from shore (maybe for $h > 10 - 15$ m depth), wave celerity is simply $c = \sqrt{gh}$ and is equal to the group velocity (Dean and Dalrymple, 1984). Hence, the eikonal equation, which is solved for $\phi_t(x, y)$ the local wave ray angle, is solely function of bathymetry and the initial tsunami direction in deep water, ϕ_{t0} (Grilli et al., 2016). Therefore, wave rays can be pre-computed in a given area of known bathymetry for a series of ϕ_{t0} values. The long wave approximation holds, and wave rays are independent from tsunami period, when the local wavelength, $L_t = cT_t \gg 20h$ or $T_t \gg 20\sqrt{h/g}$ (Dean and Dalrymple, 1984). Hence, for the minimum period of tsunami sources considered here, $T_t = 5$ or 20 min, this is true for, $h < 2,207$ or 35,316 m. It follows that all seismic tsunamis are long waves that propagate along the same wave rays, and this applies to shorter period near-field tsunamis, such as from SMF sources, that are generated in less than 2,207 m depth.

Fig. 1.6a shows 4 wave rays selected among many rays computed with the eikonal equation, that intersect the Tofino HF radar sweep area; these are incident from West (225, 285) and from South (160, 180); the only criterion for selection here was that the rays covered well the radar sweep area. As depth decreases, each wave ray becomes increasingly normal to the local bathymetric contours, consistent with the gradual orientation of the incident tsunami wave crests parallel to these contours caused by refraction (Figs. 1.3 and 1.5). Accordingly, as depth decreases, wave rays gradually loose "memory" of their initial direction of propagation in deep water and, for far-field tsunamis, become independent from the location of the tsunami source [see, e.g., (Tehranirad et al., 2015), for a more general illustration of this property of tsunami wave rays]. This implies that only a few wave rays

selected over the radar sweep area can be used to detect tsunamis from a variety of incident directions (and sources).

The relevance of wave rays computed by solving the eikonal equation is verified next. Fig. 1.6b compares, at an arbitrary time, many such wave rays with local tsunami current vectors $\boldsymbol{U_t}$ computed with FUNWAVE-TVD over the radar sweep area, for the SSZ far-field seismic tsunami; the figure also shows the magnitude of the current (length of vectors and color scale). Overall we observe a very good agreement between both, particularly in areas of stronger currents (here in 300-800 m depth), where detection with the TC-TDA would be most efficient. Other snapshots (not shown) for other times confirm this observation, with errors of less than 10% at most locations on tsunami direction. Hence, this validates the use of the geometric optics equation to predict tsunami wave rays. A consequence of this, in a tsunami detection context, is that tsunami elevation can be estimated from the radial tsunami current measured by the HF radar, U_{tr}, by projecting it along the local wave ray direction as,

$$\eta_t \simeq \frac{U_{tr}}{\cos(\boldsymbol{R}, \boldsymbol{k_t})} \sqrt{\frac{h}{g}} \tag{1.1}$$

The pre-computed wave rays allow identifying radar cells located along the same ray (see details in next section) and, still assuming linear long waves, computing the tsunami propagation time between each pair of such cells (p, q) as,

$$\Delta t_{pq} = t(\boldsymbol{R}_q) - t(\boldsymbol{R}_p) = \oint_{s(\boldsymbol{R}_p)}^{s(\boldsymbol{R}_q)} \frac{\mathrm{d}s}{\sqrt{gh(s)}} \tag{1.2}$$

with $\boldsymbol{R}(x, y)$ denoting the radial position of cells in the radar grid (with the radar location as the origin) and $s(\boldsymbol{R}(x, y))$ being the curvilinear abscissa along the selected wave ray satisfying, $\mathrm{d}s = \mathrm{d}x\, \cos\phi_t + \mathrm{d}y\, \sin\phi_t$. Hence travel times between pairs of cells can also be precalculated as a function of bathymetry.

Finally, without resorting to complex tsunami propagation simulations, the order-of-magnitude of tsunami current expected at a given depth can be estimated using Green's law (i.e., linear long wave shoaling), which neglecting refraction predicts $\eta_t = \eta_{t0}(h_0/h)^{1/4}$, given the incident tsunami elevation η_{t0} in deeper water h_0. Using Eq. (1.1), we find $U_t \propto h^{-3/4}$ and, as expected, that tsunami currents gradually increase as water depth decreases, making a tsunami gradually more detectable by the HF radar.

1.2.3 Detailed results of tsunami simulations

As shown above, the two selected tsunami sources cause very different surface elevations over the Tofino radar sweep area, which induce similarly different spatial current patterns, thus providing a good test of the ability of the proposed TDA to detect tsunamis from various sources.

For the SSZ far-field seismic source, for instance, Fig. 1.7a shows time series of computed cell-averaged tsunami radial currents (i.e., projected in the radar direction $\overline{U}_{tr} = -\overline{\boldsymbol{U}}_t \cdot \boldsymbol{R}/R$; positive towards the radar) at selected radar cells, numbered as stations 1-9 along wave ray 225 (Figs. 1.6a and 1.8a). Fig. 1.8b shows that these stations are located in increasingly deeper water, from 1 to 9, with the shelf break being between stations 5 and 6. As expected from the earlier discussion, the maximum tsunami radial velocity is largest, over 0.4 m/s, at station 1 in less than 50 m depth, but much smaller, less than 0.035 m/s, at the deepest station 9, which is over the continental slope in nearly 1,400 m depth. Despite this large change in current magnitude, however, the pattern of radial current time series repeats itself quite well at each station, from offshore to nearshore. This becomes more apparent in Fig. 1.7b, where the time series of Fig. 1.7a have been shifted by the tsunami propagation time Δt_{p1} between cells $p = 2, ..., 9$ and $q = 1$, computed with Eq. (1.2); the correlation of such time-shifted current time

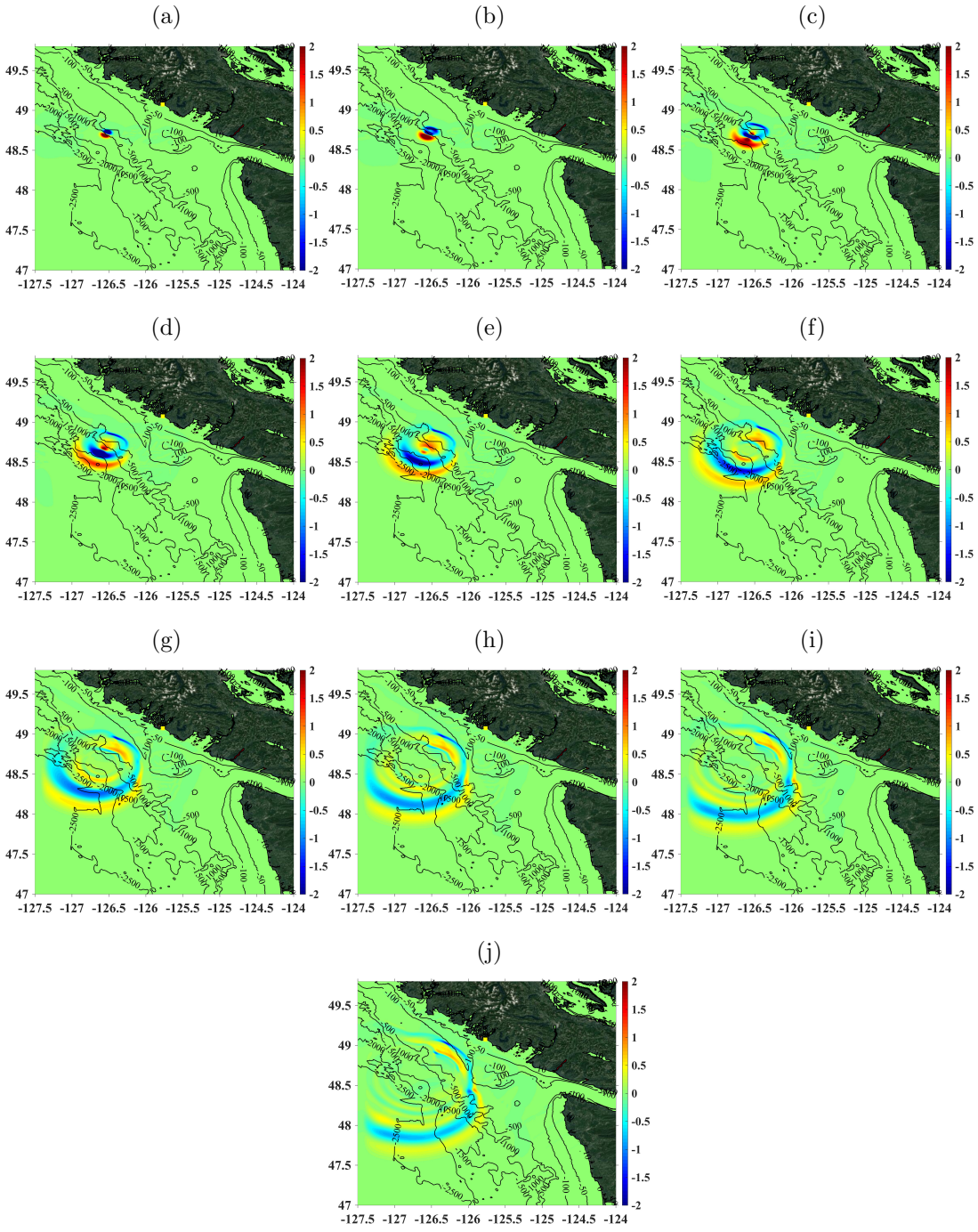

Figure 1.5: Instantaneous surface elevations (color scale in meter) simulated in grid G2 off of Tofino (■) with NHWAVE, for 1.68 km^3 SMF source (Fig. 2.1b), at t = (a) 50; (b) 100 (1'40"); (c) 200 (3'20"); (d) 300 (5'); (e) 400 (6'40"); (f) 500 (8'20"); (g) 600 (10'); (h) 700 (11'20"); (i) 800 (13'20"); and (j) 900 s (15').

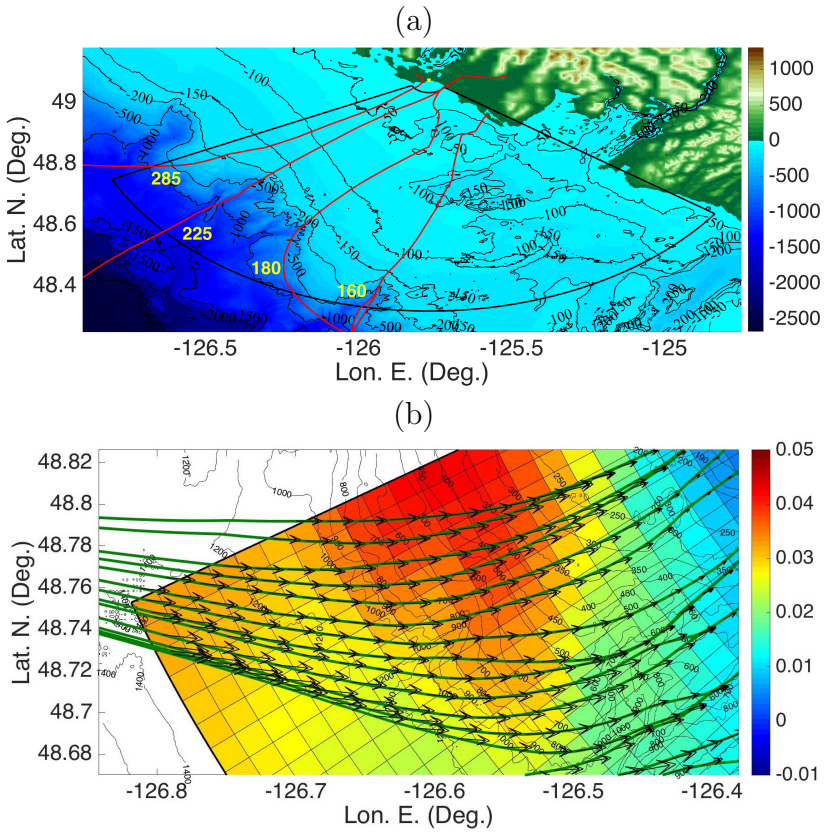

Figure 1.6: (a) Selected wave rays over the Tofino WERA HF radar sweep area, computed with the eikonal equation assuming a linear long wave, as a function of bathymetry in grid G3, incident from west (225, 285) and from south (160, 180); (b) Snapshot of instantaneous tsunami radial current magnitude (color scale in m/s) and direction (black vectors; length is proportional to magnitude) computed in grid G3 for the M_w 9.1 SSZ far-field seismic source, compared to local wave rays computed by geometric optics (solid green lines); the black grid marks the radar cell grid (near western corner of sweep area), and labeled black lines are depth contours in meter.

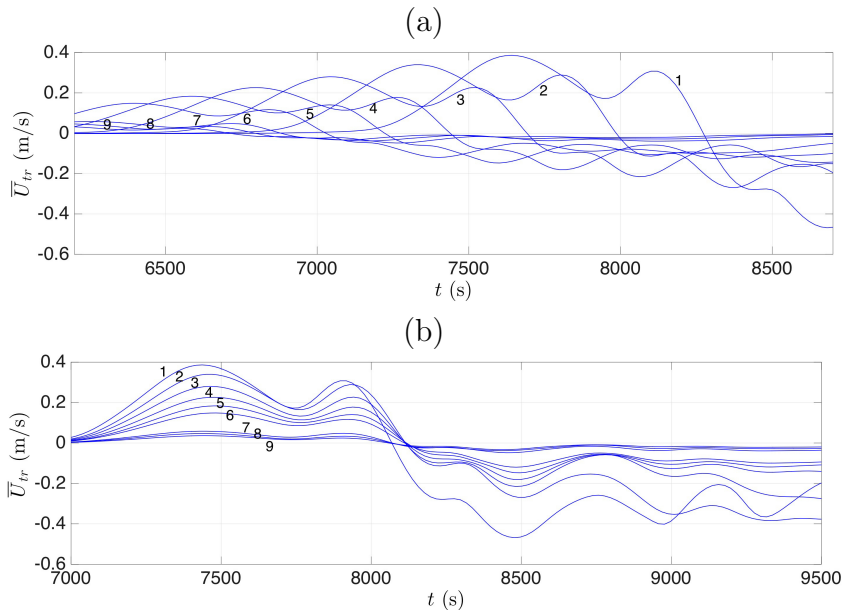

Figure 1.7: Time series of cell-averaged radial tsunami current velocity $\overline{U}_{tr} = -\overline{\boldsymbol{U}}_t \cdot \boldsymbol{R}/R$ (positive towards the radar), computed for the SSZ tsunami (Figs. 1.3 and 1.4), in 9 radar cells aligned along wave ray 225 (Fig. 1.8): (a) as a function of original time (from 1h45' to 2h25'); (b) time-shifted by the long wave propagation time Δt_{p1} from station $p = 2, ..., 9$ to station $q = 1$ (Eq. (1.2)) (from 1h57' to 2h38').

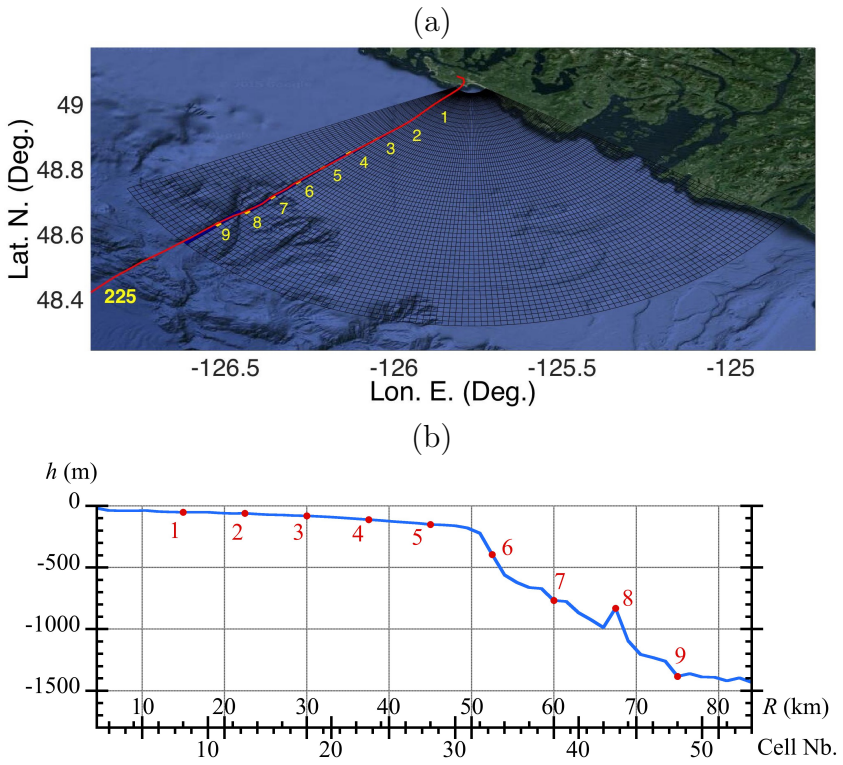

Figure 1.8: (a) Radar cell grid with wave ray 225 (—) intersecting the grid, and nine intersected cells numbered as stations 1-9 (•), as a function of increasing radar range R (and water depth). (b) Bathymetric transect along ray 225 as a function of range (R) or radar cell number (1-54; with, $R_l = 4.5 + 1.5(l-1)$ km, for cell $l = 1, ..., 54$); stations 1-9 of ray 225 are marked on the transect (•) (station ranges are, $R_k = 15 + 7.5(k-1)$ km and cell numbers, $C_k = 8 + 5(k-1)$, for $k = 1, ..., 9$); shelf break is in between stations 5 and 6.

series is very large (over 98%). Hence, this key property of tsunami currents for the viability of the proposed TC-TDA, (Grilli et al., 2016) initially made based on idealized tsunami wave train and bathymetry, is confirmed in this more realistic case study.

Similar results were obtained for the simulated currents generated by the SMF tsunami, which are not detailed here for sake of brevity.

1.3 Tsunami detection by HF radar using the TC-TDA

1.3.1 HF radar simulator

In the past four decades, HF radars have routinely been used to estimate near-surface ocean currents. The classical theory underlying this estimation is the well-known first-order Bragg scattering and we will refer to the standard literature for its derivation and use in the context of current mapping (Crombie, 1955; Barrick, 1972a; Barrick, 1972b; Barrick, 1972d; Barrick, 1972c; Stewart and Joy, 1974; Barrick, 1978).

In this paper, similar to (Grilli et al., 2016), a HF radar simulator based on first-order Bragg scattering is used to model the complex radar signal backscattered by a random sea, modulated by a time- and space-varying tsunami current. Here, this simulator is parameterized using the characteristics of the TF radar, i.e., a carrier electromagnetic (EM) wave frequency $f_{EM} = 13.5$ MHz and a usable maximum range of 85-110 km (depending on environmental conditions). [Note this frequency is similar to that (14 MHz) of the radar used by (Lipa et al., 2014) who detected a meteo-tsunami on the US East Coast shelf.]. Fig. 1.8a outlines the radar sweep area, assuming an 85 km maximum range, which is covered by radar cells of radial length $\Delta R = 1.5$ km and angular opening $\Delta\phi_r = 1$ deg in the azimuthal direction. The detection sector of the sweep area is 120 deg, implying that cells are 1.48 km wide at a 85 km range and increasingly narrower closer to the radar. The radar uses a 110 m long linear array of 12 detection antennas, with orientation 275 deg from N, clockwise (centered at 49° 4' 24.82" N, 125° 46' 11.55" W), such that one side of the sweep area boundary is nearly parallel to the coastline southeast of Tofino. [It should be noted that with this antenna array and considering the radar wavelength $\lambda_{EM} = 22.2$ m, the true angular resolution is only about $\lambda_{EM}/110 = 0.2$ rad or 11.6 deg. However in the WERA radar beam forming algorithm, a moving angular window allows providing a steering accuracy

of the radar signal of $\Delta\phi_r = 1$ deg, which is used here as this is not important for applying the TC-TDA to fairly long-crested waves.]

In the simulator, the total surface current over the radar sweep area is modeled as the sum of: (i) a spatially varying background (mesoscale) current, $\boldsymbol{U}_b(\boldsymbol{R})$, with a nearly stationary mean at the time scale of the radar data acquisition ($\mathcal{O}(T_w)$ or greater); and (ii) a spatially and temporally varying current, $\boldsymbol{U}_t(\boldsymbol{R}, t)$ induced by the tsunami wavetrain, computed with FUNWAVE-TVD for the SSZ or the SMF tsunamis (Figs. 1.3, 1.5); hence, $\boldsymbol{U}(\boldsymbol{R}, t) = \boldsymbol{U}_b(\boldsymbol{R}) + \boldsymbol{U}_t(\boldsymbol{R}, t)$. The background current has random fluctuations around its mean, which depend on local and synoptic environmental oceanic conditions. In a specific case such as off of Vancouver Island, the radial component of this current, $U_{br}(\boldsymbol{R})$, could be obtained from HF radar measurements made over the sweep area prior to tsunami arrival; here, however, as in (Grilli et al., 2016), the background current is simply modeled as a Gaussian random process.

Because radar cells are of varying size (Fig. 1.6b), we first determine which of FUNWAVE-TVD's grid cells, in the finest 90 m resolution grid G3, fall within a given radar cell (e.g., Fig. 1.2c). Based on this, for each time step of the model, the computed tsunami-induced currents are spatially-averaged over each radar cell p, yielding $\overline{\boldsymbol{U}_t}(\boldsymbol{R}_p, t)$, and projected in the local radar direction, yielding $\overline{U_{tr}}(\boldsymbol{R}_p, t)$, before being used in the radar simulator. Below, we summarize the main equations and physical processes of the simulator.

According to first-order Bragg scattering, and following (Grilli et al., 2016) (their Eq. (16)), the scattered radar signal complex amplitude takes the form,

$$\mathrm{S}_p(t) = \left(\alpha_p^- \mathrm{e}^{+2\mathrm{i}\pi f_B t} + \alpha_p^+ \mathrm{e}^{-2\mathrm{i}\pi f_B t}\right) \mathrm{e}^{-\mathrm{i}\mathcal{M}_p(t)}, \tag{1.3}$$

in each radar cell p, where $f_B = \sqrt{g/(\pi\lambda_{EM})}$ is the Bragg frequency in deep water, and $\alpha_p^{\pm}$ are complex normal variables with zero mean and variance function of the

directional wave spectrum in cell p. We refer to (Grilli et al., 2016) for an explicit formulation of the latter, as it is not necessary to know the absolute magnitude of these quantities. $\mathcal{M}_p(t)$ is a so-called "memory term" representing cumulative effects of the time varying surface current in cell p on the radar signal phase (see (Grilli et al., 2016) Eq. (10)),

$$\mathcal{M}_p(t) = \frac{4\pi}{\lambda_{EM}} \left\{ U_{br,p}\, t + \int_0^t U_{tr,p}(\tau) \mathrm{d}\tau \right\} \tag{1.4}$$

S_p is computed at a series of discrete times, $t_j = j\,\Delta t$ $(j = 1, ...)$, separated by a constant time steps, Δt.

Accounting for EM attenuation with range and environmental noise, the radar signal received from each cell p is expressed as,

$$\mathrm{V}_{p,j} = \mathrm{V}_p(t_j) = \mathcal{A}_p\ \mathrm{S}_{p,j} + \mathcal{N}_{p,j}, \tag{1.5}$$

where $\mathcal{A}_p$ is an attenuation function depending on the radar system and cell range and $\mathcal{N}_{p,j}$ is environmental noise in cell p, represented as a complex random Gaussian noise of variance $\sigma^2_{\mathcal{N}}$. The radar performance, or its ability to measure a current, depends on the SNR, which after scaling is proportional to, $\mathcal{A}'_p = \mathcal{A}_p/\sigma_{\mathcal{N}}$. Hence, in the simulator, $\mathcal{A}_p$ or the exact level of environmental noise do not have to be precisely defined, but instead the radar SNR (or $\mathcal{A}'_p$) must be specified as a function of range; here this is done based on actual data from the TF radar. As is customary, the SNR is expressed as the power of the Bragg peak divided by the Root-Mean-Square power of the available frequency band in the radar Doppler spectrum. The latter is classically obtained as the squared modulus of the FFT of $V_{p,j}$ over a windowing time T_w. Realistic SNR values were thus obtained, as a function of range, by empirically adjusting $\mathcal{A}'_p$ at every radar cell range for the simulated SNR to match values derived from TF radar data. This data became available late in the project for 6 days in 2016, representing different environmental

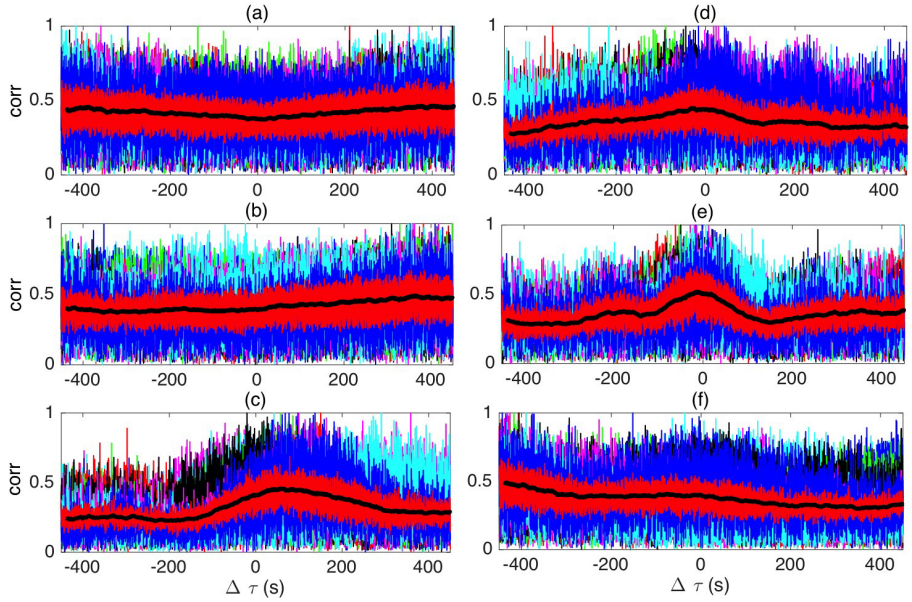

Figure 1.9: Case study of SSZ seismic tsunami source. Time-shifted correlations of radar signal (thin colored lines) computed for $T_c = 900$ s along ray 225 (Fig. 1.8a), in the presence of tsunami and random background currents, at $t =$ (a) 1h 23', (b) 1h 31', (c) 1h 39', (d) 1h 47', (e) 1h 55', and (f) 2h 03', between cells $p = 45$ ($R = 70.5$ km; Fig. 1.6c) and $q = 46 - 54$ ($R = 72$ to 84 km). The thick red line shows the cell-averaged correlation and the thicker black line is a moving average of it over 50 Δt. The appearance of a correlation peak near zero time lag is clearly detected at $t =$ 1h 39' (effective detection would occur $T_c/2 = 7.5$ min later).

conditions; radar data was averaged in azimuthal directions and processed using $T_w = 133$ s.

Note that we computed Doppler spectra in each cell p based on range resolved TF radar signal data, to which we applied a standard beam forming algorithm. No optimization, and in particular noise reduction algorithms were applied, such as, e.g., done by the standard WERA processing software to eliminate Radio Frequency Interferences (RFIs). Hence, the true SNR of the TF radar system is likely to be larger (and thus better) than that used in the radar simulator, and we expect to achieve slightly better results when applying the TC-TDA to actual radar signal data.

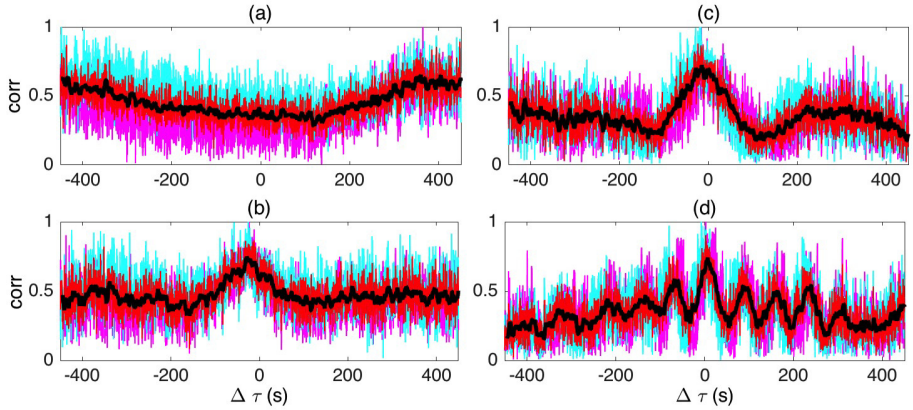

Figure 1.10: Results similar to Fig. 1.9 along ray 160 (Fig. 1.8a), computed for $T_c = 600$ s, between cells $p = 45$ ($R = 70.5$ km; Fig. 1.6c), and $q = 44$ and 46 ($R = 69$ and 72 km). The appearance of a correlation peak near zero time lag is clearly detected at $t =$ 1h 42' (effective detection would occur $T_c/2 = 5$ min later).

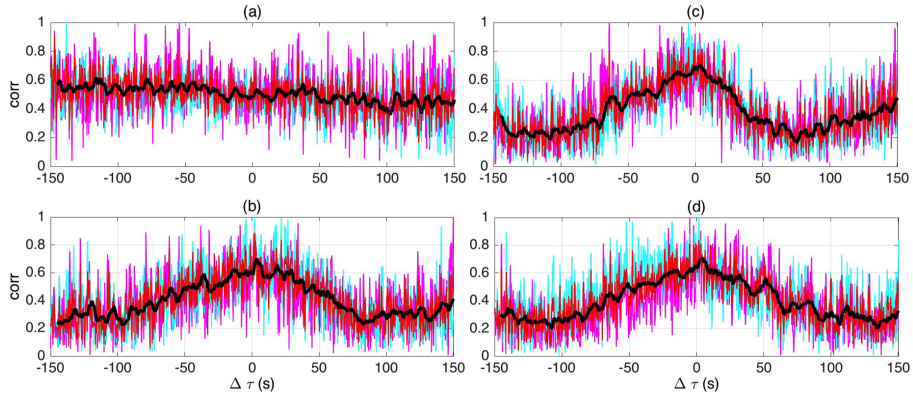

Figure 1.11: Results similar to Fig. 1.9 for case study of SMF near-field tsunami source. Time-shifted correlations of radar signal computed for $T_c = 300$ s along ray 225 (Fig. 1.8a), in the presence of tsunami and random background currents, at $t =$ (a) 3'20", (b) 5', (c) 6'40", and (d) 8'30", between cells $p = 30$ ($R = 46.5$ km) and $q = 29$ and 31 ($R = 45$ and 48 km). The appearance of a correlation peak near zero time lag is clearly detected at $t = 5'$ (b) (effective detection would occur $T_c/2 = 2.5$ min later).

1.3.2 Application of the TC-TDA to tsunami case studies

We assess the ability of the TC-TDA to detect the simulated SSZ and SMF tsunamis as follows:

(1) We use the simulator (Eqs. (1.3)-(1.5)) to compute radar signal time series, $\mathrm{V}_p(t)$, in each cell p aligned along selected wave rays crossing the TF radar sweep area (e.g., ray 225 in Fig. 1.8a); as in the TF radar data, we use $\Delta t = 0.26$ s.

(2) We do this both without tsunami currents and in the presence of cell-averaged radial tsunami currents $\overline{U_{tr}}(\boldsymbol{R}_p, t)$ modeled for the SSZ or the SMF case (with a superimposed random background current, U_{br}).

(3) We compute correlations of time series of radar signals simulated in pairs of cells (p, q) located along the same wave ray, time-shifted by the tsunami propagation time between these cells, Δt_{pq}; that is,

$$\mathrm{corr}\{\mathrm{V}_q, \mathrm{V}_p\} = \mid \frac{1}{T_c} \int_{t-\frac{T_c}{2}}^{t+\frac{T_c}{2}} \mathrm{V}_q(\tau + \Delta\tau)\, \mathrm{V}_p^*(\tau - \Delta t_{pq}) \mathrm{d}\tau \mid, \qquad (1.6)$$

for a correlation time T_c and as a function of an additional time lag $\Delta\tau$, where the star indicates the complex conjugate. [Note, to reduce high frequency oscillations observed in correlations, these are computed on the *analytical* radar signal, where negative frequencies are removed. This can easily be calculated for simulated or measured signals; see details in (Grilli et al., 2016).]

(4) In the absence of tsunami currents (or for uncorrelated random background currents), we expect correlations based on Eq. (1.6) to be flat as a function of time lag $\Delta\tau$, but to become peaked near $\Delta\tau = 0$ in the presence of incident tsunami currents. Observing this change in correlation pattern is the basis for tsunami detection.

One important feature of the TC-TDA is its lack of sensitivity to the spatial pattern of background surface currents, as long as these are slowly varying at the time scale of observations. This results from the structure of the memory term in Eq. (1.4), for which any stationary (but not necessarily spatially uniform) radial current, $U_{br,p}$, while present in the complex exponential of Eq. (1.3) and thus affecting the radar signal Doppler spectrum, can be factored out of the integral in the correlation Eq. (1.6), and thus simplifies when the absolute value is applied (unit norm). In applications, we use $T_c \simeq 5 - 15$ min, which is commensurate with T_t but much smaller than the time scale of variation of surface currents caused by mesoscale oceanic circulation, tidal cycles, or synoptic wind forcing. Therefore, a slowly fluctuating spatial current pattern, at say an hourly time scale or longer, can be discarded in the TC-TDA validation analysis, since only rapid fluctuations of the cell-averaged currents affect the magnitude of correlations. Consequently, in the validation applications detailed below, we simply assume a normally distributed background current, of zero mean and standard deviation $\sigma_c = 0.15$ m/s (meaning that 95% of these currents have a magnitude $\in [-0.3, 0.3]$ m/s), and randomly generate it in each cell at each time step. This is a large and rapidly fluctuating background current (e.g., caused by wind gusts), which should be conservative for assessing the performance of the TC-TDA.

Note that, in contrast to the TC-TDA, a Doppler-based TDA attempting to detect the oscillatory spatial pattern of inverted tsunami currents, will be more sensitive to a slowly varying non-uniform background current contributing to such oscillations. Hence, applying such a TDA requires a priori knowledge of the background current spatial distribution (which, e.g., can be inferred from radar measurements made over the past hour) to be able to correctly interpret any additional spatial oscillations in terms of an incoming tsunami wave train.

1.3.3 Far-field SSZ tsunami

Figs. 1.9 and 1.10 show, for rays 225 and 160 respectively, the correlations of radar signals calculated at far ranges with Eq. (1.6), using T_c = 900 and 600 s (15 and 10 min), between cells p = 45 (R = 70.5 km) and q = 46-54 (R = 72 to 84 km), and 44 and 46 (R = 69 and 72 km), respectively. Correlations are shifted by the tsunami travel time between cells p and q along each ray, Δt_{pq}, and computed as a function of an additional time lag $\Delta\tau$; in Figs. 1.9 and 1.10, $\Delta\tau = 0$ corresponds to t = 1 h 23' to 2h 03' and 1h 32' to 2h 02', respectively. Note that the correlation time was reduced for ray 160 because of the shorter wavelength of tsunami waves in this region of the radar sweep area; while this was done manually here, in operational conditions, the TC-TDA would simply compute time-shifted correlations at each pair of cells on selected rays, for a range of values of T_c, in order to best cover the possible values of incident tsunami periods T_t (this does not represent a significant computational effort); once a meaningful change in correlation pattern is observed, the algorithm would issue a warning and stop increasing T_c on that particular wave ray.

Results in each figure show individual correlations between pairs of cells (various colors), their average (red), and a moving average of the latter over $50\Delta t$ = 13 s (black). While individual correlations curves are very noisy, which can be shown to result from the large random background currents specified here (i.e., correlation noise is much reduced in the absence of these random fluctuations), the average correlation and in particular its moving average, which eliminates high frequency oscillations, show a clear pattern. For both rays, prior to tsunami arrival, the moving average correlations are initially flat as a function of time lag $\Delta\tau$, but as time increases and tsunami currents reach the considered radar cells, a peaked maximum of the correlation appears and gradually grows near the zero time lag,

while the correlation stays flat on either side of it. Then, for later times when the large positive tsunami currents have moved on to shallow water, and before the arrival of large negative currents, the correlations return to a flatter pattern (more so on ray 225 than 160 where there is more of an oscillatory tail trailing the leading crest of the tsunami). It should be pointed out that, as already noted by (Grilli et al., 2016), the maximum correlations of the radar signal (computed for cells 44-72 in Figs. 1.9 and 1.10) do not exactly occur at $\Delta\tau = 0$. Indeed, the time dependent memory term of Eq. (1.4) causes the radar signal phase to increase with both tsunami current and time; the latter causing an additional time lag on top of the pre-computed travel times. This additional time lag does not prevent the TC-TDA from detecting a peaked correlation pattern, since it is easy to search a short time lag window on either side of $\Delta\tau = 0$ (say [-100,+100] s in the present case).

Regarding early detection with the TC-TDA, which is the most important aspect to assess here, Figs. 1.9 and 1.10 show that a marked peaked correlation pattern occurs at $t =$ 1h 39' and 1h 42', for rays 225 and 160, respectively, to which one must add, $T_c/2 = 7.5$ and 5 min, respectively (since the correlation window is centered on current time). Hence, detection would occur at 1h 46'30" and 1h 47', for each ray, respectively, which is $\simeq$ 29 min before tsunami impact on the TF shore. Importantly, for ray 225, the maximum magnitude of tsunami currents averaged within cells 45-54, considered here, is very low (especially in view of the much larger random background currents), less than 0.04 m/s, and these cells are located in deep water beyond the continental shelf (1,200 to 1,450 m depth; Fig 1.8b).

These results confirm the conclusions of (Grilli et al., 2016), but here based on a realistic case study.

1.3.4 Near-field SMF tsunami

The same analysis and application of the TC-TDA is performed for the SMF tsunami. While the SSZ tsunami waves and corresponding surface currents had a long period (T_t = 20-40 min) and were long crested when reaching the Tofino radar sweep area (i.e., eventually nearly parallel to shore; Fig. 1.3), those created by the near-field SMF have a much shorter period ($T_t = 5 - 10$ min) and are initially made of fairly circular and concentric fronts; these eventually refract onshore to gradually align with the local bathymetry (Fig. 1.5).

Fig. 1.11 shows the correlations of radar signals computed using $T_c = 300$ s between cells $p = 30$ ($R = 46.5$ km) and $q = 29$ and 31 ($R = 45$ and 48 km) along ray 225, shifted by the tsunami travel time Δt_{pq}, as a function of an additional time lag $\Delta\tau$. Each subfigure is centered on times $t = 3'20"$ to 8'20", and the color coding of plotted lines is the same as for Fig. 1.9. Here, the cells where the SMF tsunami can be detected are located at middle-ranges, where waves have sufficiently refracted to align with the local wave rays (as shown in Fig. 1.5); this is different from the SSZ tsunami whose incident waves are already long-crested at the outskirts of the sweep area (Fig. 1.3). As discussed above, at earlier times, the SMF tsunami waves are too concentric and the radial currents still show significant 3D effects that hide the tsunami signature in the algorithm. In Fig. 1.11, we again observe a change in pattern of the moving averaged correlations, initially from flat as a function of time lag prior to tsunami arrival in the measuring region, to a peaked and growing maximum correlation near the zero time lag. The earliest detection with the TC-TDA would occur in (b), at $t = 5'$, to which $T_c/2 = 2.5$ min must be added; hence tsunami detection would occur at $t \simeq 7.5$ min after SMF tsunami generation.

1.4 Discussion and conclusions

We simulated tsunami detection by HF radar on the basis of case studies conducted for a far-field seismic (M_w 9.1 SSZ source) and a near-field SMF (1.7 km^3 rigid slump source) tsunami impacting the west coast of Vancouver Island, BC. Following a similar approach to Part I of this work (Grilli et al., 2016), we numerically modeled both tsunami propagation and radar remote sensing, but rather than using idealized tsunamis we simulated realistic tsunami sources propagating over a complex bottom bathymetry, with the 2D long wave model FUNWAVE-TVD and the 3D SMF tsunami generation model NHWAVE. Additionally, the radar signal simulator was parameterized to simulate the 13.5 MHz WERA HF radar recently installed in Tofino, BC, and radar data was used to develop a realistic representation of the SNR as a function of range.

The two tsunamis considered here, while only 2 examples among many possibilities, are representative of the large variety of tsunamis that can affect the study area, since they are at both ends of its spectrum in terms of incident wave pattern. Indeed, the far-field SSZ tsunami is made of long period waves (20-40 min) that have already significantly refracted in deep water and are approaching the shelf break as fairly long crested wave trains, which almost immediately align with the local isobaths (and thus follow well the wave rays). By contrast, the nearshore SMF tsunami is made of shorter period waves (5-10 min), which are initially concentric, causing fairly 3D currents, whose onshore moving wave train gradually refracts over the shelf, becoming more 2D and aligning with the isobaths (thus following wave rays) only in the middle ranges and depths over the shelf.

Based on these more realistic simulations, we confirmed that tsunami detection based on the proposed TC-TDA is effective for both near- and far-field sources. In the latter case, we verified that this algorithm makes tsunami detection possible

in deep water/long ranges, beyond the continental shelf, which potentially yields longer warning times (for instance, the TC-TDA first detected the SSZ tsunami arrival based on radar signal in cells overlying a 1,200-1,400 m depth).

One concern with tsunami detection algorithms is that long infragravity (IG) waves might trigger a "false positive" alert. According to the US Army Corps of Engineers Coastal Engineering Manual, IG waves have periods of 30 s to 5 min and are associated with wave groups; in deep water, they are of moderate amplitude (a few cm to a few dm). We verified that typical IG waves would not affect correlations computed by the TC-TDA, and trigger a warning, by specifying IG wave currents in the HF radar simulator, modeled as sinusoidal waves of moderate amplitude (20 cm here) and period varying from 1 to 4 min, propagating at the linear phase velocity (function of local depth). Such waves are intermediate water depth waves at the deeper end of our wave rays and hence would not quite follow the selected (long) wave rays. But assuming that did, because they propagate at a slower speed than longer tsunami waves, when time-shifted by the long wave propagation time, their correlation computed with $T_c = 10$ min between pairs of cells showed no change in pattern as compared to the situation without IG waves. This results from destructive interferences, because of their slower phase speed, in correlations computed over times longer than their period. We note, however, that even longer period IG waves would become tsunami-like, propagate along the selected "long wave" rays, and thus be detected by the TC-TDA; but such waves may be categorized as meteo-tsunamis whose detection is desirable, since they could cause dangerous resonances in bays, harbors, and marinas.

An important characteristic of the TC-TDA is its robustness to the presence of large stationary mean background currents in the radar sweep area, prior to tsunami arrival, which do not affect radar signal correlations. The TC-TDA was

also found to be robust to the choice of wave rays and we observed that the same rays could be used to detect different events without any particular optimization, provided they cover well the radar sweep area. This was illustrated here for 2 vastly different synthetic tsunami wave trains (SSZ and SMF). The 4 wave rays shown in Fig. 1.6a had initial deep water directions from the West (rays 225 and 285) and South (rays 160 and 180), and were only a few rays selected among a very large number of possible wave rays covering the radar sweep area (e.g., Fig. 1.6b). In operational conditions, both the number of selected incident deep water directions and rays could be increased, but this should only be by a few additional rays; indeed, as shown in earlier work, for long tsunami waves, rays gradually loose the memory of their incident direction once they are on the shelf slope and shelf proper (Tehranirad et al., 2015). This was confirmed in the present work, and its further developments (Guérin et al., 2017), by the fact that the TC-TDA could detect the SSZ synthetic tsunami on the 4 selected rays, albeit at slightly different times. Besides monitoring correlation patterns between pairs of cells on selected rays, the TC-TDA would also need to perform these for a range of correlation times T_c, to account for possible variations in dominant tsunami period T_t, but this can be done automatically and is not computationally intensive; for instance, here we had T_t = 20-40 min for the SSZ and 5-10 min for the SMF tsunamis.

The TC-TDA could thus be easily implemented within an operational radar system, as an additional component to a real time tsunami detection algorithm combining various instruments (e.g., as part of an observatory such as NEPTUNE), in which the radar signal would be continuously measured (rather than computed with a radar simulator) and processed in all the radar cells (Fig. 1.8a). This would only require precalculating and selecting a group of wave rays representative of possible incident tsunami directions (such as the 4 rays shown in Fig. 1.6a),

identifying which radar cells these intersect (e.g., Fig. 1.8a), and precomputing tsunami travel times between pairs of cells; all of which is easily done based on a known bathymetry. Once the algorithm in place on the radar system, time-shifted correlations could be dynamically calculated between many pairs of cells located along the pre-computed wave rays, starting from the most distant cells, as was illustrated in the present applications. The appearance of a peaked correlation between time series of time-shifted radar signal, first in the most distant pairs of cells located along the same wave rays and then averaged over a few pairs of cells (from offshore to onshore), would indicate that a tsunami is approaching the radar. In the range of periods/time scales that are considered here, there is indeed no other geophysical phenomenon that can create long wave trains that are spatially coherent, with a current magnitude sufficient to cause measurable modulations of the HF radar signal (baring very long IG waves). By computing signal correlations in all relevant pairs of cells along many wave rays, one could thus track the progression in time of an incoming tsunami by following the locations (front) of peaked correlations (e.g., Figs. 1.9, 1.10, 1.11). In the absence of a spatially coherent tsunami current, signal correlations are independent of time lag (i.e., flat); therefore, a marked difference in correlation pattern around the theoretical long wave propagation time (zero time lag) could be used to specify a tsunami detection threshold in the algorithm.

A preliminary application of the TC-TDA to actual (rather than simulated) signal data from the TF WERA HF radar can be found in (Guérin et al., 2017), which confirms the findings of this paper. While the latter study still used the 2 simulated tsunamis presented in this paper (whose signal was superimposed to actual radar data), the TC-TDA was also recently successfully applied to data from an event that triggered a real time warning from the current TF WERA

system on 10/14/16 (A. Dzvonkovskaya, personal communication, 10/2016), i.e., the algorithm detected the tsunami only on the basis of radar data; this event was likely a meteo-tsunami (A. Rabinovich, personal communication, 06/2017). These results will be reported in a forthcoming paper.

The TC-TDA has an important weakness as compared to a Doppler-based TDA, whose ability to detect tsunamis in real conditions has already been reported in the literature (Lipa et al., 2016). While the latter TDA both detects tsunami arrival and provides the magnitude of tsunami currents, from which an estimate of tsunami amplitudes can be inferred along wave rays (e.g., using Eq. (1.1)), the TC-TDA only detects tsunami arrival without providing any indication on the magnitude of currents and hence tsunami amplitude. However, the TC-TDA can potentially issue an earlier detection, in deeper water. As is well accepted in the tsunami warning community, every additional minute gained in issuing a first warning can save lives and hence is a worthwhile goal. To this effect, we compared the performance of the TC-TDA to that of a basic Doppler-based TDA for the two considered tsunami case studies, using a simple estimation of the Doppler spectrum, and found that in both cases the TC-TDA allowed gaining several minutes on the first tsunami detection. Despite these encouraging results, we elected not to include this comparison in the paper, pending both the use of actual radar data and the best available Doppler-based TDA. As indicated above, such more realistic studies are the object of ongoing work, and an in-depth and detailed comparison of both types of algorithms in quasi-operational conditions, using the same radar data and tsunami signals, will also be reported in a forthcoming paper.

Therefore, we envision that a complete tsunami detection system by HF radar could combine *both types of algorithms*, with the TC-TDA providing an early warning of tsunami arrival and the Doppler-based TDA confirming this warning in

shallower water (where the SNR/currents are higher) and also providing an estimate of tsunami elevations, which is very important to assess the potential coastal hazard. More specifically, with both algorithms implemented in real time, the TC-TDA should be able to detect the early appearance of a peaked correlation near zero-time lag by processing radar signals measured in only the first few farthest cells of the radar sweep area, aligned along selected wave rays (as demonstrated in this paper). Once this pattern detected, a first-level warning could be issued (a watch) that could gradually be confirmed, with a second-level warning issued as the tsunami propagates further into the grid and along several wave rays, and more cells and pairs of correlations are used in the detection. In parallel, after a first warning was issued, the Doppler-based TDA would continuously attempt to infer the magnitude of tsunami currents and estimate tsunami elevations along wave rays; this would become reliable once the cell-averaged radial currents and/or radar SNR achieve a sufficient magnitude. The development of an operational tsunami detection system based on these principles, and its further validation and testing for the simulated currents of a variety of near- and far-field tsunamis, whose effect is superimposed on measured radar signal (from the TF WERA HF radar) in a variety of environmental conditions, is part of ongoing work that will be reported in future papers.

Finally, one consequence of the possibility of using the TC-TDA to detect an approaching tsunami in deeper water, where tsunami currents are very small, is that for a given radar system it would be worthwhile increasing the emitted power, as much as economically and technically possible, to broaden the sweep area and increase the radar detection range beyond the local shelf break.

Acknowledgements: The authors gratefully acknowledge ONC for providing

support for this research and access to their radar system data, and Helzel Messtechnik GmbH (in particular Dr. A. Dzvonkovskaya) for technical support for processing radar data. C.-A. Guérin acknowledges the French CNRS, the University of Toulon, and the French-American Fulbright commission for support during his research stay at URI. Finally, we thank the editor and anonymous reviewers for their in-depth reviews and comments that helped improve this paper.

List of References

Abadie, S., Harris, J. C., Grilli, S. T., and Fabre, R. (2012). Numerical modeling of tsunami waves generated by the flank collapse of the Cumbre Vieja Volcano (La Palma, Canary Islands) : tsunami source and near field effects. *J. Geophys. Res.*, 117:C05030.

Anderson, P. S. (2015). Improving end-to-end tsunami warning for risk reduction on Canada's West coast. Technical Report CSSP-2013-TI-1033, Task 3 Report, Canadian Safety and Security Program.

Anderson, P. S. and Gow, G. A. (2004). Tsunamis and coastal communities in British Columbia: An assessment of the BC Tsunami Warning System and related risk reduction practices. Technical Report PS4-13/2004E-PDF, Public Safety and Emergency Preparedness Canada.

Barrick, D. E. (1972a). First-order theory and analysis of MF/HF/VHF scatter from the sea. *IEEE Transactions on Antennas and Propagation*, 20(1):2–10.

Barrick, D. E. (1972b). Remote sensing of sea state by radar. In *IEEE International Conference on Engineering in the Ocean Environment, Ocean 72*, pages 186–192. IEEE.

Barrick, D. E. (1972c). Remote sensing of sea state by radar. In *Remote sensing of the Troposphere*, volume 12. VE Derr, Editor, US Government.

Barrick, D. E. (1972d). Remote sensing of the troposphere. *Remote Sensing of Sea State by Radar*, pages 1–46.

Barrick, D. E. (1978). HF radio oceanography: a review. *Boundary-Layer Meteorology*, 13(1-4):23–43.

Barrick, D. E. (1979). A coastal radar system for tsunami warning. *Remote Sensing of Environment*, 8(4):353–358.

Benjamin, L. R., Flament, P., Cheung, K. F., and Luther, D. S. (2016). The 2011 Tohoku tsunami south of Oahu: high-frequency Doppler radio observations and model simulations of currents. *J. Geophys. Res. (publ. online)*, pages 1–29.

Bernard, E. and Titov, V. (2016). Evolution of tsunami warning systems and products. *Phil. Trans. R. Soc. Lond. A*, 373(2053):20140371.

Cherniawsky, J. Y., Titov, V., Wang, K., and Li, J.-Y. (2007). Numerical simulations of tsunami waves and currents for southern Vancouver Island from a Cascadia megathrust earthquake. *Pure Appl Geophysics*, 164(2-3):465–492.

Crombie, D. D. (1955). Doppler spectrum of sea echo at 13.56 Mc./s. *Nature*, pages 681–682.

Dean, R. G. and Dalrymple, R. A. (1984). *Water Wave Mechanics for Engineers and Scientists*. Prentice-Hall.

Dzvonkovskaya, A. (2012). Ocean surface current measurements using HF radar during the 2011 Japan tsunami hitting Chilean coast. In *Geoscience and Remote Sensing Symp. (IGARSS), 2012 IEEE Intl.*, pages 7605–7608. IEEE.

Dzvonkovskaya, A., Gurgel, K.-W., Pohlmann, T., Schlick, T., and Xu, J. (2009). Simulation of tsunami signatures in ocean surface current maps measured by HF radar. In *OCEANS 2009-EUROPE*, pages 1–6. IEEE.

Fine, I., Cherniawsky, J., Rabinovich, A., and Stephenson, F. (2008). Numerical modeling and observations of tsunami waves in Alberni Inlet and Barkley Sound, British Columbia. *Pure Appl. Geophys.*, 165(11-12):2019–2044.

Fine, I., Cherniawsky, J., Thomson, R., Rabinovich, A., and Krassovski, M. (2013). Observations and numerical modeling of the 2012 Haida Gwaii tsunami off the coast of British Columbia. *Pure Appl. Geophys.*, 172(3-4):699–718.

Fine, I., Rabinovich, A., Bornhold, B., Thomson, R., and Kulikov, E. (2005). The Grand Banks landslide-generated tsunami of November 18, 1929: preliminary analysis and numerical modelling. *Mar. Geol.*, 215:45–57.

Forget, P. (2015). Noise properties of HF radar measurement of ocean surface currents. *Radio Science*, 50(8):764–777.

Greene, H., Murai, L., Watts, P., Maher, N., Fisher, M. A., Paull, C., and Eichhubl, P. (2005). Submarine landslides in the Santa Barbara Channel as potential tsunami sources. *Natural Hazards and Earth System Science*, 6(1):63–88.

Grilli, S. T., Dubosq, S., Pophet, N., Pérignon, Y., Kirby, J., and Shi, F. (2010). Numerical simulation and first-order hazard analysis of large co-seismic tsunamis generated in the Puerto Rico trench: near-field impact on

the North shore of Puerto Rico and far-field impact on the US East Coast. *Natural Hazards and Earth System Sciences*, 10:2109–2125.

Grilli, S. T., Grosdidier, S., and Guérin, C.-A. (2016). Tsunami detection by High Frequency Radar beyond the continental shelf. I. Algorithms and validation on idealized case studies. *Pure Appl Geophysics*, 173(12):3,895–3,934.

Grilli, S. T., Harris, J. C., Tajalli-Bakhsh, T., Masterlark, T. L., Kyriakopoulos, C., Kirby, J. T., and Shi, F. (2013). Numerical simulation of the 2011 Tohoku tsunami based on a new transient FEM co-seismic source: Comparison to far- and near-field observations. *Pure Appl Geophysics*, 170:1333–1359.

Grilli, S. T., Ioualalen, M., Asavanant, J., Shi, F., Kirby, J. T., and Watts, P. (2007). Source constraints and model simulation of the December 26, 2004 Indian Ocean tsunami. *J Waterway Port Coastal Ocean Eng*, 133(6):414–428.

Grilli, S. T., O'Reilly, C., Harris, J., Tajalli-Bakhsh, T., Tehranirad, B., Banihashemi, S., Kirby, J., Baxter, C., Eggeling, T., Ma, G., and Shi, F. (2015). Modeling of SMF tsunami hazard along the upper US East Coast: Detailed impact around Ocean City, MD. *Natural Hazards*, 76(2):705–746.

Guérin, C.-A., Grilli, S., Moran, P., Grilli, A., and Lado, T. (2017). Tsunami detection by High Frequency Radar using a Time-Correlation Algorithm: performance analysis based on data from a HF radar in British Columbia. In *Proc. 27th Offshore and Polar Engng. Conf. (ISOPE17, San Francisco, USA. June 2017) (to appear).*

Gurgel, K.-W., Dzvonkovskaya, A., Pohlmann, T., Schlick, T., and Gill, E. (2011). Simulation and detection of tsunami signatures in ocean surface currents measured by HF radar. *Ocean Dynamics*, 61(10):1495–1507.

Heron, M. L., Prytz, A., Heron, S. F., Helzel, T., Schlick, T., Greenslade, D. J., Schulz, E., and Skirving, W. J. (2008). Tsunami observations by coastal ocean radar. *Intl J Remote Sensing*, 29(21):6347–6359.

Hinata, H., Fujii, S., Furukawa, K., Kataoka, T., Miyata, M., Kobayashi, T., Mizutani, M., Kokai, T., and Kanatsu, N. (2011). Propagating tsunami wave and subsequent resonant response signals detected by HF radar in the Kii Channel, Japan. *Estuarine, Coastal and Shelf Science*, 95(1):268–273.

Horrillo, J., Grilli, S., Nicolsky, D., Roeber, V., and Zhang, J. (2014). Performance benchmarking tsunami operational models for NTHMP's' inundation mapping activities. *Pure Appl Geophysics*, 172:869–884.

Insua, T., Grilli, A. R., Grilli, S. T., Shelby, M., Wang, K., Gao, D., Cherniawsky, J., Harris, J. C., Heesemann, M., McLean, S., and Moran, K. (2015). Preliminary tsunami hazard assessment in British Columbia, Canada. *EOS Trans. AGU*, 96(52):Fall Meet. Suppl., Abstract NH23C–1890.

Ioualalen, M., Asavanant, J., Kaewbanjak, N., Grilli, S. T., Kirby, J. T., and Watts, P. (2007). Modeling the 26th December 2004 Indian Ocean tsunami: Case study of impact in Thailand. *J. Geophys. Res.*, 112:C07024.

Kânoğlu, U., Titov, V., Bernard, E., and Synolakis, C. (2015). Tsunamis: bridging science, engineering and society. *Phil. Trans. R. Soc. A*, 373(2053):20140369.

Kirby, J. T., Shi, F., Tehranirad, B., Harris, J. C., and Grilli, S. T. (2013a). Dispersive tsunami waves in the ocean: Model equations and sensitivity to dispersion and Coriolis effects. *Ocean Modeling*, 62:39–55.

Kirby, S., Scholl, D., Von Huene, R., and Wells, R. (2013b). Alaska earthquake source for the SAFRR tsunami scenario. Technical Report USGS Report, 2013, U.S. Geological Survey Open-File . http://pubs.usgs.gov/of/2013/1170/b/, The SAFRR (Science Application for Risk Reduction) Tsunami Scenario.

Lipa, B., Barrick, D., and Isaacson, J. (2016). *Tsunami*, chapter Chapter 5: Coastal Tsunami Warning with Deployed HF Radar Systems, pages 73–112. Environmental Sciences. InTech.

Lipa, B., Barrick, D., Saitoh, S.-I., Ishikawa, Y., Awaji, T., Largier, J., and Garfield, N. (2011). Japan tsunami current flows observed by HF radars on two continents. *Remote Sensing*, 3(8):1663–1679.

Lipa, B., Isaacson, J., Nyden, B., and Barrick, D. (2012a). Tsunami arrival detection with high frequency (HF) radar. *Remote Sensing*, 4(5):1448–1461.

Lipa, B. J., Barrick, D. E., Bourg, J., and Nyden, B. B. (2006). HF radar detection of tsunamis. *J Oceanography*, 62(5):705–716.

Lipa, B. J., Barrick, D. E., Diposaptono, S., Isaacson, J., Jena, B. K., Nyden, B., Rajesh, K., and Kumar, T. (2012b). High frequency (HF) radar detection of the weak 2012 Indonesian tsunamis. *Remote Sensing*, 4:2944–2956.

Lipa, B. J., Parikh, H., Barrick, D. E., Roarty, H., and Glenn, S. (2014). High frequency radar observations of the June 2013 US East Coast meteotsunami. *Natural Hazards*, 74:109–122.

Lynett, P. and thirty-seven alii (2017). Inter-model analysis of tsunami-induced coastal currents. *Ocean Modeling*, 114:14–32.

Ma, G., Shi, F., and Kirby, J. T. (2012). Shock-capturing non-hydrostatic model for fully dispersive surface wave processes. *Ocean Modeling*, 43-44:22–35.

McAdoo, B. and Watts, P. (2004). Tsunami hazard from submarine landslides on the Oregon continental slope. *Marine Geol*, 203(3):235–245.

Myers, E. and Baptista, A. (2001). Analysis of factors influencing simulations of the 1993 Hokkaido Nansei-Oki and 1964 Alaska tsunamis. *Natural Hazards*, 23:1–28.

Rabinovich, A., Thomson, R., and Fine, I. (2013). The 2010 Chilean tsunami off the west coast of Canada and the northwest coast of the United States. *Pure Appl. Geophys.*, 170:1529–1565.

Shi, F., Kirby, J. T., Harris, J. C., Geiman, J. D., and Grilli, S. T. (2012). A high-order adaptive time-stepping TVD solver for Boussinesq modeling of breaking waves and coastal inundation. *Ocean Modeling*, 43-44:36–51.

Stewart, R. H. and Joy, J. W. (1974). HF radio measurements of surface currents. In *Deep Sea Research and Oceanographic Abstracts*, volume 21(12), pages 1039–1049. Elsevier.

Tang, L., Titov, V., Moore, C., and Wei, Y. (2016). Real-time assessment of the 16 september 2015 Chile Tsunami and implications for near-field forecast. *Pure Appl Geophysics*.

Tappin, D. R., Grilli, S. T., Harris, J. C., Geller, R. J., Masterlark, T., Kirby, J. T., Shi, F., Ma, G., Thingbaijamg, K., and Maig, P. (2014). Did a submarine landslide contribute to the 2011 Tohoku tsunami ? *Marine Geol.*, 357:344–361.

Tappin, D. R., Watts, P., and Grilli, S. T. (2008). The Papua New Guinea tsunami of 1998: anatomy of a catastrophic event. *Natural Hazards and Earth System Sciences*, 8:243–266.

Tehranirad, B., Harris, J., Grilli, A., Grilli, S., Abadie, S., Kirby, J., and Shi, F. (2015). Far-field tsunami hazard in the north Atlantic basin from large scale flank collapses of the Cumbre Vieja volcano, La Palma. *Pure Appl Geophysics*, 172(12):3,589–3,616.

Tehranirad, B., Shi, F., Kirby, J. T., Harris, J. C., and Grilli, S. T. (2011). Tsunami benchmark results for fully nonlinear Boussinesq wave model FUNWAVE-TVD, Version 1.0. Technical Report No. CACR-11-02, Univ. of Delaware.

Thomson, R., Fine, I., Rabinovich, A., Mihly, S., Davis, E., Heesemann, M., and Krassovski, M. (2011). Observation of the 2009 Samoa tsunami by the NEPTUNE-Canada cabled observatory: Test data for an operational regional tsunami forecast model. *Geophys. Res. Lett.*, 38:L11701.

Thomson, R. E., Rabinovich, A. B., Fine, I. V., Sinnott, D. C., McCarthy, A., Sutherland, N. A. S., and Neil, L. K. (2009). Meteorological tsunamis on the coasts of British Columbia and Washington. *Physics and Chemistry of the Earth Parts A/B/C*, 34(17):971–988.

Titov, V., Rabinovich, A., Mofjeld, H., Thomson, R., and Gonzalez, F. (2005). The global reach of the 26 December 2004 Sumatra tsunami. *Science*, 309(5743):2045–2048.

Whitmore, P. (1993). Expected tsunami amplitudes and currents along the North American coast for Cascadia Subduction Zone earthquakes. *Natural Hazards*, 8:59–73.

Yelisetti, S., Spence, G., and Riedel, M. (2014). Role of gas hydrates in slope failure on frontal ridge of northern Cascadia margin. *Geophysical J Intl*, 199(1):441–458.

MANUSCRIPT 2

Tsunami detection by High Frequency Radar in British Columbia: performance assessment of the Time-Correlation Algorithm for synthetic and real events

Published in Ocean Dynamics, September (online 2/20/2018), 1-16. DOI 10.1007/s10236-018-1139-7

By

Charles-Antoine Guérin[1], Stéphan T. Grilli[2], Patrick Moran[2], Annette R. Grilli[1],Tania L. Insua[3]

1. Université de Toulon, Aix Marseille Univ., CNRS IRD, MIO UM110, La Garde, France
2. Department of Ocean Engineering, University of Rhode Island, Narragansett, RI 02882, USA
3. Ocean Networks Canada (ONC), 2300 McKenzie Ave., Victoria, BC, VBW 2Y2, Canada

Abstract

The authors recently proposed a new method for detecting tsunamis using High-Frequency (HF) radar observations, referred to as "Time-Correlation Algorithm" [TCA; (Grilli et al., 2016a; Grilli et al., 2016b; Grilli et al., 2017)]. Unlike standard algorithms that detect surface current patterns, the TCA is based on analyzing space-time correlations of radar signal time series in pairs of radar cells, which does not require inverting radial surface currents. This was done by calculating a contrast function, which quantifies the change in pattern of the mean correlation between pairs of neighboring cells upon tsunami arrival, with respect to a reference correlation computed in the recent past. In earlier work, the TCA was successfully validated based on realistic numerical simulations of both the radar signal and tsunami wave trains. Here, this algorithm is adapted to apply to actual data from a HF radar installed in Tofino, BC, for three test cases: 1) a simulated far-field tsunami generated in the Semidi Subduction Zone in the Aleutian Arc; 2) a simulated near-field tsunami from a submarine mass failure on the continental slope off of Tofino; and 3) an event believed to be a meteo-tsunami, which occurred on October 14th, 2016, off of the Pacific West Coast and was measured by the radar. In the first two cases, the synthetic tsunami signal is superimposed onto the radar signal by way of a current memory term; in the third case, the tsunami signature is present within the radar data. In light of these test cases, we develop a detection methodology based on the TCA, using a correlation contrast function, and show that in all three cases the algorithm is able to trigger a timely early warning.

2.1 Introduction

Tsunamis are among the natural disasters that can impact highly populated, low lying, coastal areas. In recent past, the world was reminded of their destructive power by the 2004 Indian Ocean (IO) [e.g,

(Titov et al., 2005; Grilli et al., 2007; Ioualalen et al., 2007)] and Tohoku 2011 [e.g., (Mori et al., 2012; Grilli et al., 2013)] mega-tsunamis, which caused nearly 250,000 combined fatalities. While their most common generation process is seismicity, tsunamis can be generated by a variety of non-seismic processes, such as volcanic activity [e.g., (Abadie et al., 2012; Tehranirad et al., 2015)], submarine mass failure [SMF; e.g., (Fine et al., 2005; Tappin et al., 2008; Grilli et al., 2015)], and atmospheric disturbances known as meteo-tsunamis (Monserrat et al., 2006; Thomson et al., 2009).

Mitigating tsunami coastal impact, particularly loss of life, requires issuing early warnings to the population. In the US, the two NOAA tsunami warning centers, operate around the clock in Hawaii and Alaska to do so, using extensive numerical modeling together with data from a variety of instruments, such as deepwater pressure sensors [DART buoys; e.g., (Bernard and Titov, 2016)]. Recently, High Frequency (HF) oceanic radars deployed along the shore have proved effective in detecting tsunamis, while they are still a large distance away from shore [see, e.g., (Grilli et al., 2016a; Grilli et al., 2017) and reviews and references therein]. Although most of these detections were made in *a posteriori* reanalyses of radar data [e.g., (Lipa et al., 2014; Benjamin et al., 2016)], a HF radar deployed in Tofino, BC (off of the Pacific Ocean side of Vancouver Island) detected a potential meteo-tsunami in real time on October 14, 2016 (Dzvonkovskaya et al., 2017).

The detection of tsunamis by HF radars was first proposed by Barrick (Barrick, 1979), but it is only in the aftermath of the IO 2004 tsunami that this possibility was confirmed by numerical simulations [e.g., (Lipa et al., 2006; Heron et al., 2008; Gurgel et al., 2011; Fuji and Hinata, 2017)], and following the Tohoku 2011 tsunami in *a posteriori* reanalyses of radar data [e.g., (Hinata et al., 2011; Lipa et al., 2011; Lipa et al., 2012a; Benjamin et al., 2016)].

HF radars can measure properties of the ocean surface (e.g., radial surface current, significant wave height,...) beyond the horizon, over a large sweep area reaching up more than 100 km offshore (depending on frequency, antenna power, and environmental noise), with a ∼120 degree or greater aperture. In most HF radar systems, radial surface currents are reconstructed over a dense grid of radar cells (a few by a few km in size), based on the shift they induce in the backscattered Doppler spectrum [so-called Bragg scattering phenomenon; (Crombie, 1955; Barrick, 1972a; Barrick, 1972b; Barrick, 1972d; Barrick, 1972c; Stewart and Joy, 1974; Barrick, 1978)]. This ability of HF radars to provide a dense dataset of time series of radial surface currents, makes them more suitable to detect tsunami currents generated by non-seismic sources (e.g., SMFs, meteotsunamis) than traditional point-based sensors (e.g., pressure or tide gages). Indeed, such tsunamis can occur at any location on or near the continental shelf and shelf break, without the advance warning of an associated strong earthquake to orient the detection of a possibly generated tsunami.

Tsunami Detection Algorithms (TDAs) based on radial surface currents inverted from HF radars have been proposed in some of the studies referred to above, which identify the oscillatory nature of tsunami currents in space and/or time, and TDAs are operational at a few radar locations (e.g., in Tofino, BC). These will be referred to in the following as "Doppler Method" (DM) TDAs. There are, however, some limitations to this detection method [TCA; (Grilli et al., 2016a; Grilli et al., 2017)]. Essentially, to be detectable, tsunami currents must rise above the threshold of accuracy of the Doppler-based estimation, which is inversely proportional to the radar frequency and integration time used to compute the spectrum; thus, estimating small currents requires large integration times. However, this conflicts with the oscillatory nature of tsunami currents, as averaging radar

data over a large integration time reduces the estimated current magnitude, making tsunamis less detectable. Hence, one must use a short enough integration time (up to a few minutes) to avoid averaging out tsunami currents. Another limitation is the radar Signal-to-Noise Ratio (SNR), which must remain sufficiently large at the chosen integration time to allow for a reliable estimation of the surface currents. In practice, this limits tsunami detection by way of Doppler shifts to either strong currents (hence on the continental shelf due to shoaling effects), or weak currents but strong SNR (hence in the short ranges), as was for instance the case for the weak 2012 Indonesian tsunami (Lipa et al., 2012b). It should be pointed out that, assuming an integration time of a few minutes, this limitation is more important for the shorter period non-seismic tsunamis (T ∼5-10 min), than for the longer period co-seismic tsunamis (T ∼10-40 min).

To alleviate this limitation of DM-TDAs, (Grilli et al., 2016a) proposed a new method, referred to as "Time Correlation Algorithm" (TCA), that does not require inverting currents from Doppler spectra, but instead detects changes in patterns of correlations of radar signal time series, computed between pairs of cells located along pre-computed tsunami wave rays. Performing numerical simulations of both radar signal and tsunami current, for idealized (Grilli et al., 2016a) and realistic (Grilli et al., 2016b; Grilli et al., 2017) seafloor bathymetry and tsunamis, the authors showed that the TCA-TDA, which does not depend on an integration time, may be able to detect weaker tsunami currents (a few cm/s) in deeper water, beyond the continental shelf, without averaging them out. More specifically, (Grilli et al., 2017) validated the TCA-TDA using a radar simulator developed using the characteristics of the Tofino WERA HF radar system (manufactured by Helzel Messtechnik GmbH), combined with actual measurements of its signal-to-noise ratio (SNR) as a function of range. The simulator was applied to tsunami

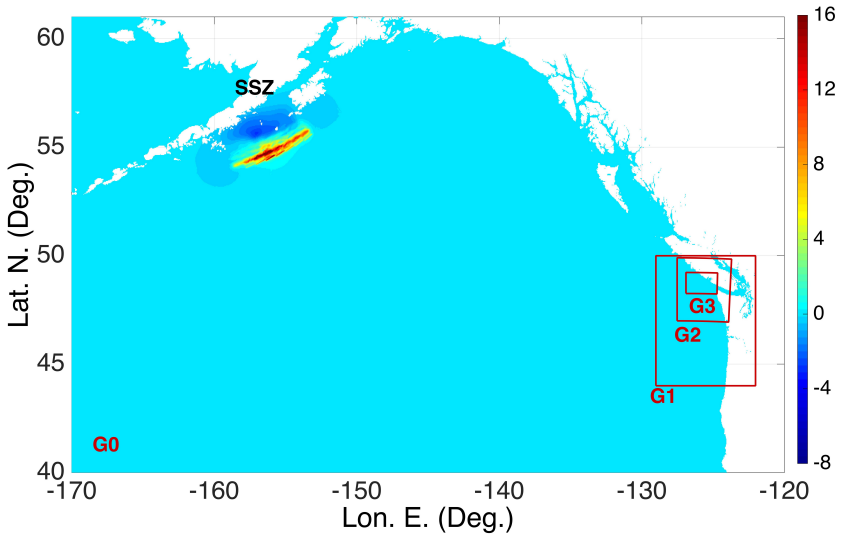

Figure 2.1: Zoom-in on part of 2 arc-min grid G0 used in FUNWAVE-TVD's simulations of the M_w 9.1 co-seismic tsunami sourced in the Semidi Subduction Zone (SSZ); black boxes mark boundaries of nested model grids off of Vancouver Island, BC: G1 (0.6 arc-min), G2 (270 m), and G3 (90 m). The color scale (meter) is the initial surface elevation of the SAFRR seismic source used in simulations.

currents simulated in the area off of Tofino, using a long wave model, for two cases: (i) a Mw 9.1 far-field co-seismic tsunami, sourced in the Semidi Subduction Zone (SSZ; Fig. 1); and (ii) a near-field SMF tsunami triggered on the continental slope, directly off of Tofino (Fig. 2). They concluded that the TCA had the potential to detect the incoming tsunamis further offshore, in deeper water, than using an algorithm based on currents directly inverted from the Doppler spectra (DM). Despite these encouraging results, no definitive conclusions could be drawn before the TCA algorithm was tested using actual radar data. Indeed, besides the idealization of the radar signal in the simulator, the background oceanic currents were also simplified in earlier work (as purely random) and ionospheric contamination as well as Radio Frequency Interferences (RFI) were ignored.

In view of this, in this paper, we first apply the TCA to actual data measured with the Tofino radar (for a few days with different oceanic conditions and wave cli-

mate), over which effects of tsunami currents simulated for the same two cases as in (Grilli et al., 2017) (Figs. 1, 2) are superimposed. [We refer to (Grilli et al., 2017) for details of numerical simulations of tsunami generation and propagation for the SSZ and SMF sources (e.g., Fig. 3).] While one cannot get a tsunami on demand and see its impact on radar data, one can, however, numerically simulate the effects of simulated tsunami currents on measured radar data; this works by introducing, in each radar cell, a phase shift depending on a current memory term (see details below). This technique was already used for instance in (Gurgel et al., 2011) to simulate the effects a past tsunami event would have produced on radar data. If not a definitive assessment of an operational TCA-TDA, this approach represents a further step towards a better evaluation of its performance. In a second part we apply the TCA to radar data acquired during an event, which on October 14, 2016 triggered a warning from the DM-TDA that is part of the standard WERA radar system. This event was determined to be a potential meteo-tsunami event (Dzvonkovskaya et al., 2017), although some other long wave phenomena cannot entirely be ruled out, and, hence, this test case represents a fully realistic, albeit offline, validation of the TCA tsunami detection abilities.

2.2 HF radar system and data used in this work

In April 2016, Ocean Networks Canada (ONC) installed a WERA HF radar near Tofino, BC, on the west coast of Vancouver Island (Canada) (Fig. 2), as a component of their ocean observing systems. This radar was equipped with a commercial tsunami detection software, provided by the Helzel company, with the aim to evaluate real-time tsunami detection by HF radar data on the coast of British Columbia. This radar has a carrier electromagnetic frequency $f_{EM} = 13.5$ MHz and a 110 m long array of 12 antennas, centered at 49° 4' 24.82" N, 125° 46' 11.55" W, yielding an 85-110 km range, depending on sea state and atmospheric

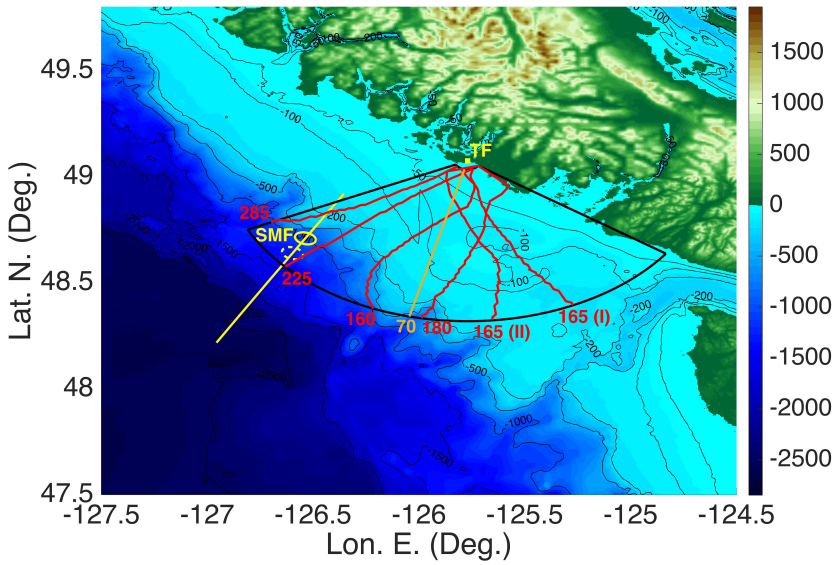

Figure 2.2: Bathymetry/topography (color scale and contours) and sweep area (black sector; assuming a 85 km maximum range) of the WERA HF radar located in Tofino, BC (TF; ■). The solid yellow ellipse (centered at 48.70822 Lat. N. and -126.53669 Lon. E.) and dashed line mark the initial SMF footprint ($w = 8$ by $b = 6$ km) and direction of motion (209 deg. clockwise from N), respectively; the dashed ellipse marks its final location ($s_f = 9$ km downslope). The numbered red solid lines mark 6 wave rays selected to apply the TCA-TDA, and the brown line is a selected azimuth (70th).

conditions, and a ∼12 deg. azimuthal resolution at the center of the beam. The orientation of the radar array, 275 deg. from N, clockwise, and its 120 deg. beam opening, yield a sweep area for which one side is nearly parallel to the coastline southeast of Tofino (Fig. 2). In the radar signal processing system, the sweep area is divided into radar cells, within which the received radar signal is averaged (and radial surface currents are inverted). These cells all have a radial length $\Delta R = 1.5$ km and the angular opening $\Delta\phi_r = 1$ deg. is used in the direction finding algorithm to process the radar signal in overlapping angular windows; hence cell width and area: $\Delta\mathbb{S} = R\,\Delta R\,\Delta\phi_r$ increase with range.

In the application of the TCA-TDA to synthetic tsunamis presented later, several days of radar data corresponding to different oceanic conditions will be used (Julian days 200, 227, 238, 287, 289 in 2016), including one day with a strong swell (i.e., day 289, with a 4.3 m significant wave height and 10.7 s peak spectral wave period), over which effects of simulated tsunami currents will be superimposed (see details below). In the application of the TCA-TDA to the detection of the potential meteo-tsunami event of October 14, 2016, the algorithm will be directly applied to radar data measured on that day (Julian day 288). The main sea state parameters of the different days are summarized in Table 2.1. These were extracted from records of a nearby buoy (La Perouse, station C46206), available online on the Canadian Marine Environment Data Service (http://www.meds-sdmm.dfo-mpo.gc.ca).

2.3 Simulation of synthetic tsunamis

In earlier work, Grilli et al. (Grilli et al., 2016b; Grilli et al., 2017) simulated the surface elevations and currents caused by two hypothetical tsunamis, over the Tofino radar sweep area. As indicated above, tsunami currents simulated for the same two sources are used in this paper to test the TCA-TDA, in combination with

Day	H_s	T_p	WD	WS
200 (0-2)	1.1	8.4	-	-
227 (11-13)	2.15-2.41	6.9	183	9.9
238 (1-2)	1.01	6.9	36	0.2
287 (0-2)	2.75	6.9	106	14.8
288 (6-8)	4.54	16	183	10.1
289 (6-8)	4.32	10.7	155	6

Table 2.1: Available sea state conditions as recorded at La Perouse Bank station (462006) for the different days of radar data. From left to right column: Julian day (UTC hour of the day), significant wave height (H_s, in m), Wave peak period (T_p, in s), Wind direction (WD, in degree TrueNorth), Wind speed (WS, in m/s)

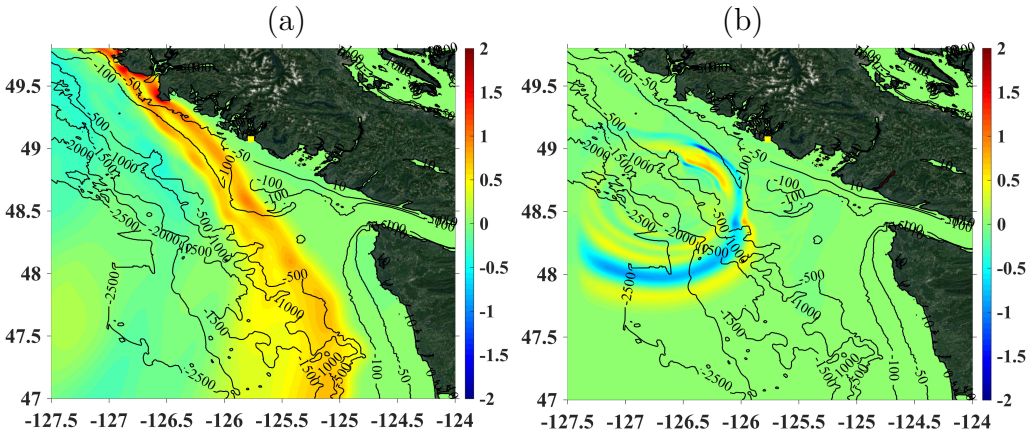

Figure 2.3: Instantaneous surface elevations (color scale in meter) simulated in grid G2: (a) with FUNWAVE-TVD for the SSZ source (Fig. 1), at $t = 7200$ s; b) with NHWAVE for the SMF source (Fig. 2) at $t = 800$ s.

actual radar data. Details of source parameterization and tsunami generation and propagation simulations can be found in the references.

The first synthetic tsunami was co-seismic and generated by a M_w 9.1 far-field source located in the Semidi Subduction zone (SSZ; Fig. 1). This source was designed by the SAFRR group as a worst-case scenario for northern California (Kirby et al., 2013) and is also a plausible major tsunami case for the Pacific West Coast of Canada. The SSZ tsunami propagation was modeled using the Boussinesq long wave model FUNWAVE-TVD (Shi et al. 2012; Kirby et al. 2013a) by one-way coupling, using a series of nested spherical, then Cartesian, grids of increasingly

fine resolution towards the coast of Tofino (G0-G3; Fig. 1; Fig. 3a). The second synthetic tsunami was generated by a near-field SMF of volume 1.7 km^3, located in a 980 m depth on the continental slope, 70 km off of Tofino (Fig. 2); the SMF geometry was idealized as a sediment mound of quasi-Gaussian shape with 8 by 2 km elliptical footprint and maximum thickness 100 m (Fig. 2). The SMF tsunami generation was modeled in grid G2 as a rigid slump with a $s_f = 9$ km runout, using the non-hydrostatic model NHWAVE (Ma et al., 2012; Grilli et al., 2015), with 5 boundary conforming layers in the vertical direction. Once generation was completed, simulations were continued with FUNWAVE-TVD in grid G2 and then by one-way coupling in grid G3 (Fig. 2.3b). In both cases shown in Fig. 2.3, time is measured from the initial time ($t = 0$) corresponding to the initiation of the tsunami wave train at the source. It takes approximatively 2 hours and 20 min for the SSZ tsunami to reach the shore of Vancouver Island near Tofino, and only 20 minutes for the SMF tsunami.

To simulate their effect on radar data, time series of simulated horizontal tsunami currents $\mathbf{u}_t$ are projected in the radar radial direction $\mathbf{R}$ as $U_{tr} = \mathbf{u}_t \cdot \mathbf{R}$ and spatially-averaged over individual radar cells in the sweep area. Note, as FUNWAVE-TVD's G3 grid 90 m resolution was much smaller than most radar cells' area, a large number of grid cells were averaged to compute tsunami radial current time series within each radar cell. To apply the TCA, many wave rays were computed from a number of assumed incident directions, by solving the wave geometric optic equation for the specified bottom bathymetry. A small number of these rays (6 rays labeled 160 to 285 in Fig. 2) was selected, which covered well the radar sweep area, particularly in its distant shallower parts where currents are stronger. Radar cells aligned along these rays were identified and tsunami propagation times between such cells computed using the linear long wave phase

velocity $c = \sqrt{gh}$ (where g is gravitational acceleration and h the depth), also as a function of the local bathymetry. Details of the wave ray and travel time computations can also be found in the references.

2.4 The Time-Correlation Algorithm (TCA)

According to first-order Bragg theory, the complex back-scattered signal received at time t for a given radar cell q is of the form,

$$\mathrm{V}_q(t) = \alpha^+ \; e^{-2\mathrm{i}\pi f_B t} + \alpha^- \; e^{+2\mathrm{i}\pi f_B t} \tag{2.1}$$

where $\alpha^{\pm}$ are complex constant coefficients, functions of sea state, range, and radar calibration, and $f_B = \sqrt{g/(\pi\lambda_{EM})}$ is the Bragg frequency (λ_{EM} is the electromagnetic wavelength). In the presence of a constant radial surface current U_r, the complex radar signal experiences a Doppler frequency shift $f_U = -2U_r/\lambda_{EM}$ and is thus multiplied by a complex exponential $e^{2\mathrm{i}\pi f_U t}$. For a variable current in time, $U_r(t)$, the Doppler frequency shift is obtained through the integration of the instantaneous Doppler frequency $f_U(t) = -2U_r(t)/\lambda_{EM}$, and the radar time series is thus multiplied by the complex exponential $e^{\mathrm{i}M(t)}$, where,

$$M(t) = -\frac{4\pi}{\lambda_{EM}} \int_{-\infty}^{t} U_r(t')dt' \tag{2.2}$$

is often referred to as a *current memory term*, since it integrates the past values of the current.

In the presence of a tsunami wave train, the radar signal of Eq. (1) is thus modified as,

$$\mathrm{V}_q(t) = \left(\alpha^+ \; e^{-2\mathrm{i}\pi f_B t} + \alpha^- \; e^{+2\mathrm{i}\pi f_B t}\right) e^{\mathrm{i}M(t)} \tag{2.3}$$

where the memory term is computed based on the tsunami radial current, space-averaged within each radar cell U_{tr}.

As seen in tsunami simulations (e.g., Fig. 3) and according to linear long wave theory, the arrival of an incident tsunami wave train within a given sea

state, causes the appearance of a slowly varying horizontal current propagating at the long wave phase speed c, whose amplitude is nearly proportional to the local tsunami elevation and inversely proportional to $\sqrt{h}$. The main principle underlying the TCA, proposed by the authors in earlier work, is to take advantage of the unique large scale coherency of this tsunami-induced current, to identify (i.e., detect) its occurrence in the radar signal through its effect on the memory term M. As the tsunami wave train propagates over large distances, refracting along wave rays as a function of its (depth-dependent) phase speed (well approximated by c), currents induced at successive locations along such a ray should be strongly correlated. More specifically, we expect the strongest correlation to occur between the current $U_{tp}(t)$ at cell p and the time-shifted current $U_{tq}(t+t_{pq})$ at cell q, where t_{pq} is the tsunami travel time from cell p to cell q, and currents used here are projections of $\mathbf{u}_t$ on the local wave ray. This property carries over to the memory term and, therefore, also to the radar signal itself, which is modulated by M (see Eq. (3)), assuming that most wave rays at far ranges, where detection is most effective, are directed more or less towards the radar (e.g., Fig. 2) and hence, the effect of projecting currents from the tangential direction to a ray to the radial direction is negligible.

Based on this principle, the TCA calculates correlations of complex backscattered radar signal time series, $V_p(t)$ and $V_q(t-t_{pq})$, received from 2 given cells p and q located along the same tsunami ray, shifted by the tsunami propagation time between these cells (if cell q is located farther offshore than cell p, travel time t_{pq} is positive),

$$C_{pq}(\tau;t) = \left|\mathrm{corr}\{\mathrm{V}_p(t+\tau), \mathrm{V}_q(t-t_{pq})\}\right|. \tag{2.4}$$

as a function of an additional time lag $\tau \in [-T_l/2, T_l/2]$, with T_l, the length of the time lag window. With this definition, the maximum signal correlation is expected

to occur at $\tau = 0$. Hence, a change in pattern of previously computed correlations C_{pq} near $\tau = 0$ should indicate that a tsunami is propagating through the radar sweep area. In practice, assuming short time stationarity, the ensemble average is obtained through a temporal average using a running time window in the recent past,

$$C_{pq}(\tau; t) = \left| \frac{1}{T_c - \tau} \int_{I_t} \mathrm{V}_p(t' + \tau)\, \mathrm{V}_q^*(t' - t_{pq})\, \mathrm{d}t' \right| \tag{2.5}$$

where the integration is performed over the time interval $I_t = [t - T_c, t - \tau]$. Here, $T_c > T_l$ the length of the time window (i.e., correlation time), which should be sufficiently large to capture a meaningful part of the oscillations of the tsunami current, that is at least one-third to one-half the tsunami dominant period T_t (in the following applications we used $T_c = 900$ to 1200 s). Note that in Eq. (2.5), the integration domain decreases as time lag increases, which is due to the requirement that the calculation of the correlation at the present time does not require knowledge of the radar time series in the future ($t' + \tau > t$). The reduction of the integration time as lag increases is compensated by the atypical normalization factor $1/|T_c - \tau|$. This ensures in particular that the correlation of two uniform signals remains flat and prevents the occurrence of an artificial correlation peak near zero time lag.

2.5 Application of the TCA to actual radar data

We obtained raw signal recorded by the Tofino HF radar system at a sampling rate $\Delta t = 0.26$ s, for Julian days 200, 227, 238, 287, 289 in 2016 and October 14th, 2016, and processed it in range and azimuth using software developed by Helzel Messtechnik GmbH, to produce time series of complex backscattered signal $\mathrm{V}_q(t)$ for each radar cell q located along the selected tsunami rays in the sweep area (Fig. 2). The first 5 days were randomly selected from a larger dataset, as complete days of records representing different oceanic conditions.

Following Eq. (3), the effect of synthetic tsunami currents on radar data was simulated by multiplying the measured radar signal time series by the complex memory term from Eq. (2.2), computed in each cell based on space-averaged radial currents U_{tr}, i.e.,

$$V_p \to V_p(t)\, \mathrm{e}^{\mathrm{i}M(t)} \tag{2.6}$$

To avoid spurious values, which are sometime observed in radar signal time series, and to equalize their magnitude at different ranges, only the re-centered and normalized complex values of the radar signal time series were retained, i.e., we considered signals of the form,

$$S_p(t) = \frac{V_p(t) - \overline{V_p}}{|V_p(t)|}, \tag{2.7}$$

where $\overline{V_p}$ is the temporal mean of the signal in the window of observation.

Time-shifted, radar signal correlations $C_{pq}(\tau;t)$ between pairs of cells (p,q) were calculated with Eq. (5), based on $S_p(t)$. In each case, the signal at radar cell p was correlated with that at its Kth neighbor, $p+K$, for N successive values (that is $p = p_0, p_0+1, .., p_0+N-1$). The N resulting correlations were normalized by their maximum and averaged over the N available pairs,

$$C_{p_0,N,K}(\tau;t) = \frac{1}{N} \sum_{p=p_0}^{p_0+N-1} \frac{C_{p,p+K}(\tau;t)}{\max_\tau(C_{p,p+K}(\tau;t))} \tag{2.8}$$

A final smoothing in time (here over a 120 s window) was finally applied to remove higher-frequency oscillations in the average correlation (which had negligible effect on the contrast function detailed later).

Figs. 4a,b show plots of correlations $C_{p_0,N,K}(\tau;t)$ computed as a function of τ, on day 238, for $p_0 = 31$, $N = 23$ and $K = 1$, along rays 160, 180, 225 and 285, at two different times $t =$ 1h48'09" and 1h56'09" into the SSZ tsunami event (red lines), compared to the reference correlation computed using data 1h in the past (black dashed lines). By contrast with the idealized cases studied earlier using

a radar simulator (Grilli et al., 2016a; Grilli et al., 2016b; Grilli et al., 2017), in which the radar data showed a flat correlation in the absence of a tsunami, here the reference correlation already exhibits a strong correlation peak near the zero time lag, even in the absence of a tsunami. This was first noted by (Guérin et al., 2017), who postulated that this is likely an artifact of the radar signal processing algorithms (i.e., range-gating and beam-forming), which are applied to raw data to calculate the range- and azimuth-resolved radar signal. It is difficult to provide a rigorous explanation for this phenomenon without delving into details of the radar signal processing algorithm. In short, this is due to the fact that the simultaneous signals backscattered from neighboring radar cells cannot be exactly uncoupled in the range and azimuthal processing. Comparing time-shifted correlations computed with and without tsunamis, such in Figs. 4c and d, but for more distant cells, would show that this preexisting correlation between cells is stronger than the additional signal correlation resulting from the current memory term. However, even though the computed time-shifted correlations are not flat in the absence of the tsunami, the occurrence of the latter still manifests itself in a measurable way, through an increase of the mean correlation $C_{p_0,N,K}$ (Figs. 4a,b). This is due to the highly correlated structure of the memory term caused by the tsunami current, for time-shifted radar cell time series. Hence, tsunami detection can still be easily achieved by observing a clear change in pattern of the mean correlation with respect to some reference level. In an operational way, as already indicated above, the reference correlation of a given sea state in the absence of a tsunami can simply be calculated using the radar signal recorded in the recent past, say 1 h earlier. During this length of time, while the tsunami wave train has not yet reached the radar cells, both sea state and radar characteristics can be assumed to be quasi-steady.

Therefore, to quantify this change in correlation pattern, a *contrast function* is introduced defined as,

$$\Gamma_{p_0,N,K}(t) = \frac{\int_{-T_l/4}^{T_l/4} \left(C_{p_0,N,K}(\tau;t) - C^{\text{ref}}_{p_0,N,K}(\tau;t) \right) d\tau}{\int_{-T_l/4}^{T_l/4} \left(C_{p_0,N,K}(\tau;t) + C^{\text{ref}}_{p_0,N,K}(\tau;t) \right) d\tau} \tag{2.9}$$

This function quantifies the change in area of the mean correlation $C_{p_0,N,K}$ with respect to its reference value $C^{\text{ref}}_{p_0,N,K}$, normalized by the sum of the respective areas. Note, only the central half of the correlation lags in the correlation window T_l are considered, since the larger lags are less reliable from a numerical point of view. The reference correlation $C^{\text{ref}}_{p_0,N,K}$ can simply be taken as a correlation computed in the recent past, that is $C^{\text{ref}}_{p_0,N,K}(\tau;t) = C_{p_0,N,K}(\tau;t-\Delta t)$, for some time shift Δt to be defined. In the following applications, we use $\Delta t = 1$ h, for which meteorological and oceanic conditions are expected to be quasi-steady. This choice also results from a technical convenience, as the radar time series is interrupted in the last 2.5 minutes of each hour for control purposes. Hence, the choice of a one-hour time shift for the reference signal makes it possible to process an interrupted subsequent time series of 57.5 minutes.

We also tested several values of the separation distance K between the correlation pairs and found that taking $K = 1$ (i.e., using the nearest neighboring cell range-ward) led to computing the most discriminant contrast function. It should be noted that, in this case where correlations are computed for adjacent radar cells, the tsunami travel time between cells is very small (on the order of 20 to 50 s) compared to both the time correlation window T_c and the dominant tsunami wave period T_t; hence we observed that ignoring this travel time (i.e., setting $t_{pq} = 0$ in Eq. (2.4)) had negligible effects on the contrast function. The results below were nevertheless computed using the travel times.

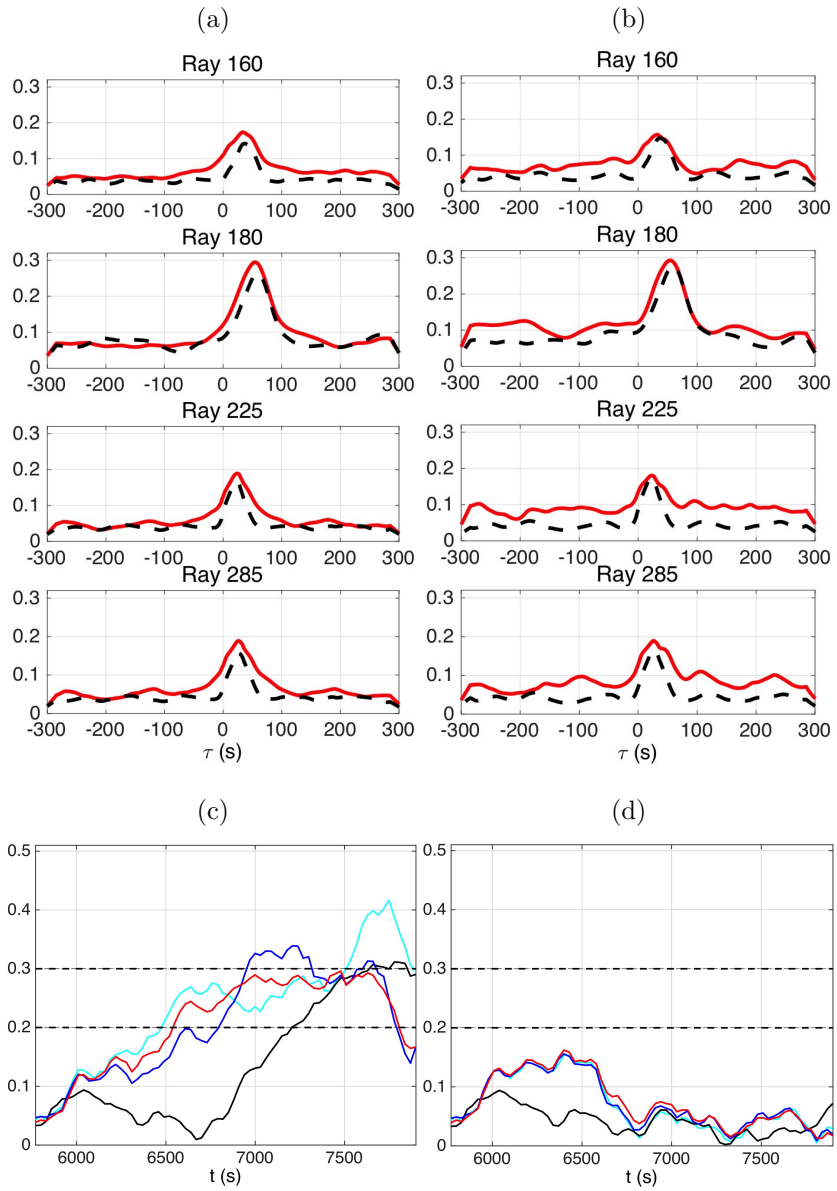

Figure 2.4: (a) and (b), mean correlations $C_{31,23,1}$ (red solid lines) and their reference values (black dashed lines) computed as a function of time lag τ for the SSZ tsunami, using radar data from day 238, at $t =$ (a) 1h48' (first warning); and (b) 1h56' (alert confirmation). [The correlations have been smoothed with a 120 s window.] (c) Time series of contrast function $\Gamma_{31,23,1}$ computed along rays: (cyan) 160, (black) 180, (blue) 225, and (red) 285; based on a low and high contrast threshold 0.2 and 0.3, respectively (horizontal dashed lines), a first warning would be issued at 6,480 s (1h48') and an alert confirmation at 6,960 s (1h56') into the event. (d) Same as (c), with no synthetic tsunami current added.

2.6 Application of the TCA to synthetic tsunami detection

2.6.1 The far-field SSZ co-seismic tsunami

Fig. 4 shows the mean correlation $C_{31,23,1}(\tau)$ and corresponding contrast function $\Gamma_{31,23,1}(t)$ (with and without the tsunami), computed along 4 tsunami wave rays marked in Fig. 2 (160, 180, 225 and 285), as a function of time lag τ and time t, respectively. In the correlations, time series of radar signal measured in cells 31 to 53 (corresponding to ranges from 45 to 79.5 km) are correlated with those in the neighboring cells range-ward (i.e., cells 32 to 54), using an integration window $T_c = 1,200$ s. The figure shows results based on data measured on Julian day 238 in 2016 (on which the synthetic tsunami current effect was superimposed), but several days of radar data corresponding to different oceanic conditions were tested (Julian days 200, 227, 238, 287, 289 in 2016). Figs. 2.4a, b show the mean correlation (here smoothed over a 120 s moving window) and Figs. 2.4c, d the contrast function with and without tsunami currents. In Fig. 2.4c, a clear increase in contrast can be observed as the tsunami wave train propagates across the radar cells. Based on a low contrast threshold of 0.2, a first warning could be issued at $t = 6,480$ s (1h48') while a confirmation (i.e., an alert) could be issued at $t = 6,960$ s (1h56') based on a higher contrast threshold of 0.3. This is confirmed in Figs. 2.4a,b, which show average correlations computed at these critical times for cells 31 to 53, along the 4 selected wave rays; a clear change in pattern of these correlations can be observed with respect to the reference correlations (calculated based on data 1 h in the past). To confirm the relevance of this alert, the contrast functions were also calculated In Fig. 2.4d using the same radar data time series, but without superimposing the memory term based on the tsunami current (Eq. (2.6)); the contrast functions clearly remain below both low and high contrast thresholds. It is interesting to note that the detection based on the contrast function is effective even though the magnitude of the tsunami-induced currents

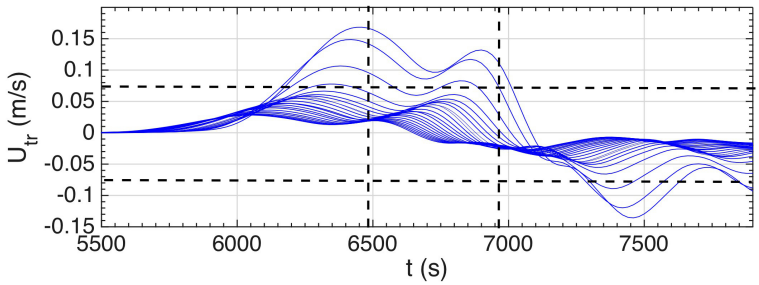

Figure 2.5: Time series of radial surface currents induced by the SSZ tsunami (Figs. 1 and 3a) computed at radar cells 31 to 53 along ray 225 (Fig. 2) using FUNWAVE-TVD. The vertical dashed lines mark the time of first warning (1h48') and alert (1h56'), while the horizontal dashed lines mark the region with a ±7.5 cm/s current magnitude.

is small in cells 31 to 53. This can be seen in Fig. 2.5, which shows the time evolution of radial tsunami surface currents $U_{tr}(t)$ calculated in these cells, along the ray 225, from FUNWAVE-TVD's simulations of the SSZ source. At the time of first warning (1h48'), the magnitude of tsunami-induced currents is less than 7.5 cm/s, except in the 3 shallowest radar cells (31-33), where it reaches up to 17 cm/s. Similar results and detection times (not shown) were obtained using radar data for the other 4 selected days, even on day 289, which had a strong swell.

2.6.2 The near-field SMF tsunami

The same numerical experiment was repeated using the SMF tsunami currents, for the same radar cells, rays, and radar time series of different hours and days. Due to the smaller time scales involved, a smaller integration time $T_c = 900$ s was used. Fig. 2.6 shows an example of the contrast function $\Gamma_{31,23,1}$ computed on Julian day 238 with (a) and without (b) a superimposed tsunami current. In the presence of the latter, a first warning could be issued 6 min 9 s into the event, using rays 225 and 285, and a confirmation could be given at 8 min 39 s. Numerical experiments using several other hours and days worth of data revealed a stable pattern for the evolution of the contrast function, regardless of the oceanic

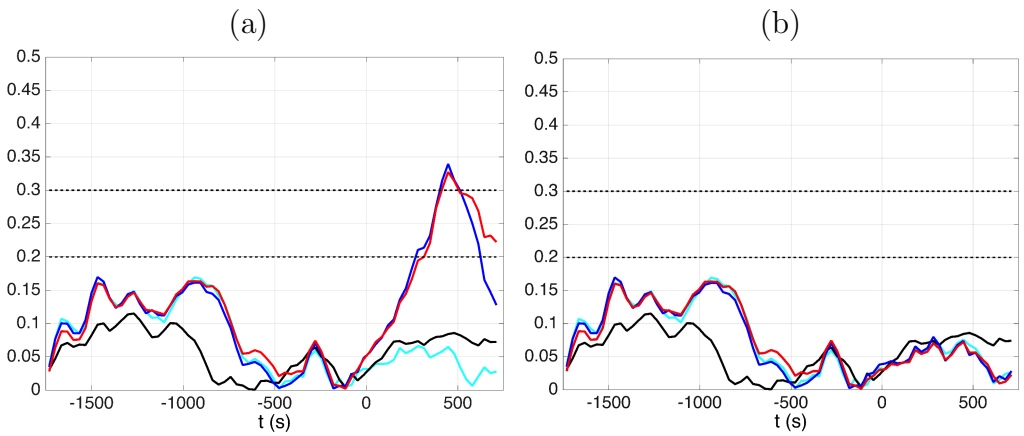

Figure 2.6: Time series of the contrast function $\Gamma_{31,23,1}$ computed as a function of time along rays (Fig. 2): (cyan) 160, (black) 180, (blue) 225, (red) 285, for the synthetic SMF source combined with radar data from day 238, with (a) and without (b) a superimposed tsunami; based on a low and high contrast threshold of 0.2 and 0.3, respectively (horizontal dashed lines), a first warning would be issued 369 s (6 min 9 sec) into the event using rays 225 and 285, and a confirmation of this warning (an alert) would be issued at 519 s (8 min 39 s).

conditions, and showed that the highest threshold (here a value of 0.3) is never reached in the absence of a tsunami.

2.6.3 The influence of sea state

An important question is whether the efficiency and ability to issue a warning of the TCA are robust to sea state and in which respect the contrast functions shown for the synthetic tsunami test cases are impacted by the variability of the radar data (which is itself related to the variability of oceanic conditions). To answer this question, we applied the algorithm to the few days and hours of radar data which are summarized in Table 1 and evaluated the contrast functions for both the SMF and SSZ tsunami test cases. We found the same trends in contrast function from one day to another as for day 238, but also observed that the function levels was slightly dependent on the selected time period. In some cases, this implied that a warning threshold was reached on a given day but missed on another.

This is illustrated in Fig. 2.7 where the SSZ and SMF contrast functions on ray 225 are evaluated using radar data from five Julian days: 200, 227, 238, 287 and 289. The figure shows, in this case, that the alert threshold would not be reached on day 289 for the 2 tsunamis while a false warning would be triggered. Julian day 289 (October 15, 2016) was a day with a much larger wave height and period ($H_s \simeq 4.5$ m and $T_p \simeq 10.7$ s at La Perouse Bank station; see Table 2.1) than for the other trial days. An analysis of the full archive of data at La Perouse Bank station during 2016, shows that such a significant wave height, although not exceptional, is quite rare as it belongs to the top 8% of the recorded values. As of now, we have no definite explanation for the lesser performance of the TCA on a day with a strong sea state, which is an issue that will require further investigation.

For calm or moderate sea states (Julian days 200, 227, 238 and 287), we could not establish any systematic relation between the "quality" of the contrast function and sea state parameters. We observed that, similarly to the Doppler Method, the performance of the TCA is primarily impacted by the SNR (which can be defined as the ratio of the Bragg peak and the background power in the HF radar signal) and the strength of the tsunami currents, which depends on local bathymetry. However, as the TCA is not based on inverting radial currents, this algorithm is expected to be more robust to a smaller SNR than the Doppler Method and to be less sensitive to the background oceanic currents. Note that there is no obvious relationship either between sea state and SNR, as the attenuation in the propagation of electromagnetic surface waves over a rough sea is compensated by the increasing strength of the Bragg wave component. Hence, a complete and reliable assessment of the performance of TCA as a function of sea state could only be performed on a statistical basis, by testing a large number of days of radar data and wave rays, which is beyond the scope of this paper.

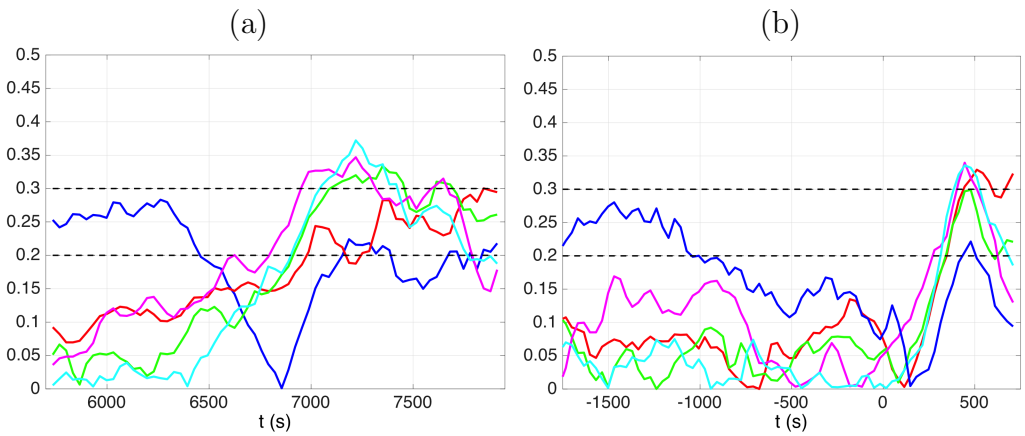

Figure 2.7: Time series of contrast function $\Gamma_{31,23,1}$ computed as a function of time along ray 225 (Fig. 2) using the radar data of Julian day: (red) 200, (green) 227, (magenta) 238, (cyan) 287 and (blue) 289, for the synthetic a) SSZ source b) SMF source.

To further evaluate the robustness of the TCA to strong sea states, we recalculated the same contrast functions along different rays on day 289, for the two synthetic tsunamis (Fig. 8). As seen on the figure, at in least in the SSZ case, the simultaneous use of different rays allows to compensate for the loss of quality of the contrast function of individual rays in case of a strong sea state.

2.7 Offline detection of meteo-tsunami with the TCA

2.7.1 The October 14th, 2016 event

On October 14th, 2016, at 6h 06 min UTC, the WERA HF radar installed in Tofino, whose system was running the standard tsunami detection software developed by Helzel Messetechnik GmbH (DM-TDA based), triggered a tsunami alert, as the influence of the approaching typhoon Songda was starting to be felt along the Pacific coasts of the US and Canada. At the time of the alert, long-period sea level oscillations of ∼20 cm amplitude were clearly measured by some nearby tide gauges and meteorological stations located off of the coast recorded the propagation of a strong low pressure front (of about 980 milibar), moving at an exceptionally high speed of ∼95 km/h (see Figs. 2.9 and 2.10). Since no seismic

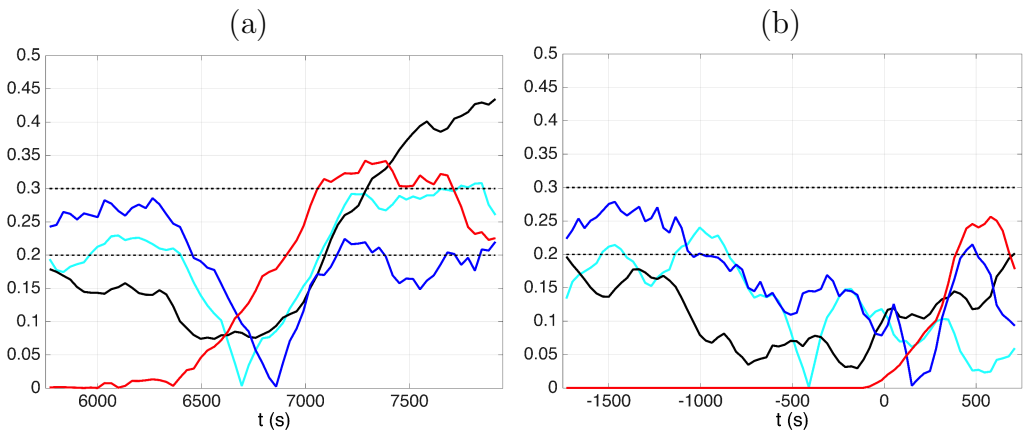

Figure 2.8: Time series of contrast function $\Gamma_{31,23,1}$ computed as a function of time along rays (Fig. 2): (cyan) 160, (black) 180, (blue) 225, (red) 285, for the synthetic a) SSZ source b) SMF source combined using radar data from day 289.

activity was reported in the region at the time, it seemed that this event could have been of atmospheric origin and, in particular, a meteo-tsunami. Dzvonkovskaya et al. (Dzvonkovskaya et al., 2017) provided an initial geophysical interpretation of this event as well as data on current measurements and tsunami detection achieved by the standard TDA that was running in real time in the Tofino HF radar system. If, in research still in progress, this event was confirmed to have indeed been a meteo-tsunami, it would be the first example in the history of HF radars, of a real time tsunami detection. To date, it is still not definitely established whether this event was caused by a storm surge, a seiche, a meteo-tsunami, infra-gravity waves, or any combination of these four types of phenomena. A thorough analysis and inclusion of all available geophysical data is necessary to reach more definitive conclusions in this respect. Below, we further analyze this event and then assess the TCA detection performance in this context.

To better understand the event that triggered the tsunami alert in the radar system, we first analyzed time series of radial surface currents inverted from 3h of radar data acquired between 4h 00 min and 6h 58 min UTC on 10/14/16. Here,

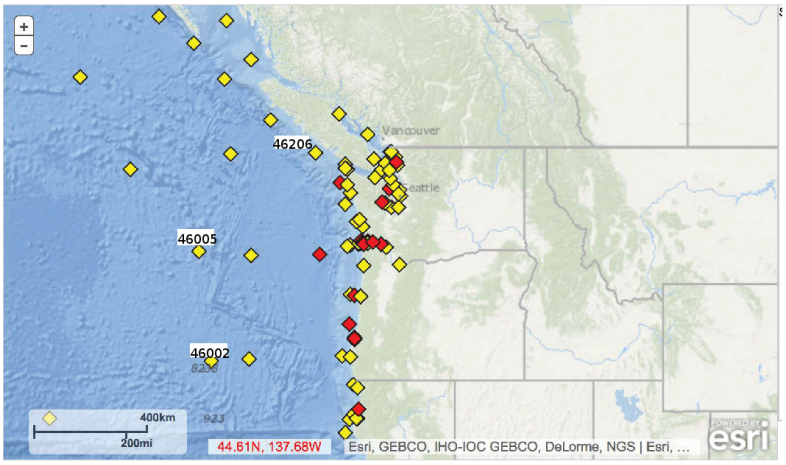

Figure 2.9: Location of NOAA meteorological stations 46002, 46005 and 46206.

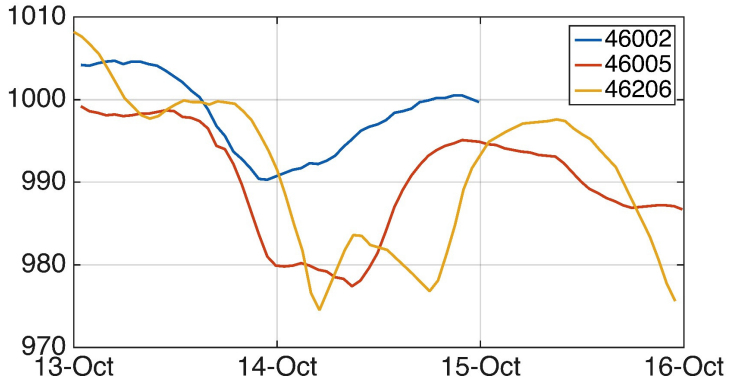

Figure 2.10: Time series of atmospheric pressure (milibar) measured at NOAA stations 46002, 46005 and 46206 (Fig. 6) from October 13-16, 2016. The propagation of a low pressure front towards the NNE, at a speed of about 95 km/h, is clearly visible.

currents were inverted using a Bayesian probabilistic method recently developed by the authors to efficiently and accurately process data originating from phase array systems (Guérin and Grilli, 2017). In this method, a Bayesian estimation of the absolute value of the surface currents is calculated based on time series of complex radar signal backscattered from each radar cell, similar to those processed in the TCA. Specifically, a "Maximum A Posteriori Probability Estimate" (MAPPE) is developed using relevant *a priori* information on the surface currents, which makes it possible inverting currents in a noisy environment with short integration times; as discussed above, the latter is important when dealing with tsunami currents. Figure 2.11 shows the evolution of the absolute value of radial currents calculated with the MAPPE method over different cell intervals/ranges along azimuth 70 (Fig. 2). Here, ∼2 min sliding intervals (512 samples; 133 s) were used to produce surface current time series, with a 16 s update rate. The *a priori* probability distribution used in the Bayesian estimation was Gaussian with a mean equal to the average value estimated over the past 264 s of data and standard deviation set to 15 cm/s. The starting time in the estimation was 4h 00 min UTC. Figs. 2.11a,b,c clearly show a sudden increase in radial current magnitude by ∼25-30 cm/s (i.e., a current front), at 96 (5h 36 min UTC), 110 (5h 50 min UTC), and 129 (6 h 09 min UTC) min, over cells 40-41, 30-31 and 20-21, respectively. A similar analysis made in other azimuthal directions on either side of azimuth 70 (not shown here) yielded a consistent, albeit less pronounced, behavior, supporting the hypothesis that this unusual current pattern followed a main direction of propagation close to azimuth 70.

The speed of propagation of the observed current front can approximately be estimated by dividing cell range interval by time difference between Figs. 2.11a, b and c. Thus, as the current front occurs at 5:36' at range 40 and 5:50' at range

30, a 15 km propagation takes place in 14 min, yielding a 64 km/h propagation speed between these two locations. Similarly, at range 20 the front is seen at 6:09', which in turn implies a propagation speed of 47 km/h between ranges 30 and 20. Considering the bathymetric variation under azimuth 70 (Fig. 2.12), these propagation speeds are close to the long wave celerity $c = \sqrt{gh}$ computed from the local bathymetry h: in average, 65 km/h between cells 40 and 30 and 55 km/h between cells 30 and 20. If one assumes that the propagating current front is caused by an atmospheric disturbance, this close correspondence with the local free long wave speed supports the occurrence of a Proudman resonance and, hence, the hypothesis of a meteo-tsunami (Monserrat et al., 2006).

2.7.2 Detection of a potential meteo-tsunami event with the TCA

In the following, we investigate whether the TCA would have detected the October 14th, 2016 event, had it been running in real time on the radar system, and estimate when a first warning could have been issued. To do so, we applied the TCA to the Tofino radar data acquired over the sweep area during the time period surrounding the occurrence of the candidate meteo-tsunami event, i.e., 4h 00 min to 7h 00 min UTC. Unfortunately, no data were available after 7h 00 min, as the storm associated with this event caused an electrical outage in Tofino. Figure 2.13 shows time series of contrast functions calculated along the 6 rays shown in Fig. 2.2, which cover well the entire sweep area. Although an operational TDA would systematically check a large number of possible cell intervals on each selected wave ray, here for illustration we used 3 relevant cell intervals on each ray, namely cells 20 to 30 (Figs. 2.13a,b), 30 to 40 (Fig. 2.13c,d), and 40 to 50 (Fig. 2.13e,f). Radar data in each cell within these ranges was correlated with that of its neighboring cell range-ward, yielding 21 correlation pairs (C_{30-31}, C_{31-32}, ..., C_{50-51}). The reference correlations necessary to evaluate the contrast functions were obtained

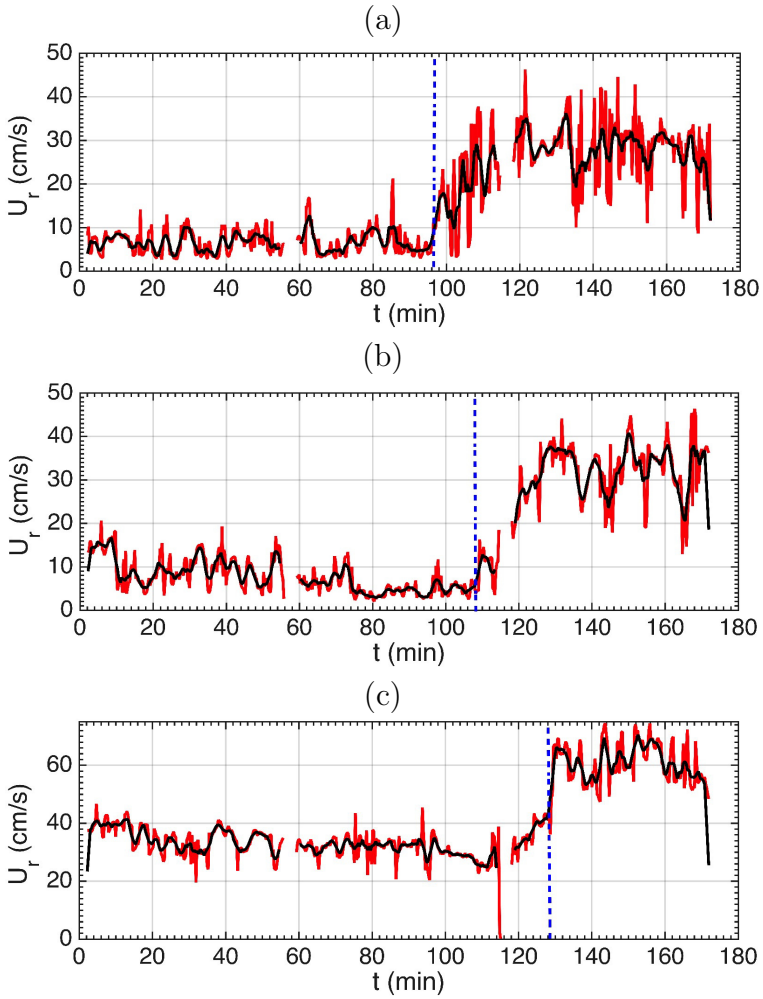

Figure 2.11: Time series of inverted radial surface currents (red lines), and smoothed currents (black lines) computed on October 14th, 2016 (day 288) along azimuth 70 (Fig. 2), averaged over cells/ranges: (a) 40-41; (b) 30-31; and (c) 20-21 (the time origin is at 4h 00 min UTC). Radial currents are estimated every 16 s using the MAPPE method (Guérin and Grilli, 2017), for overlapping intervals of 512 points (133 sec). The occurrence of a jump in current magnitude is clearly visible in figures (a-c), at 96 (5h 36 min UTC), 108 (5h 48 min UTC) and 129 (6h 09 min UTC) min, respectively (marked by a vertical dashed line), which propagates from ranges 40, to 30 and 20.

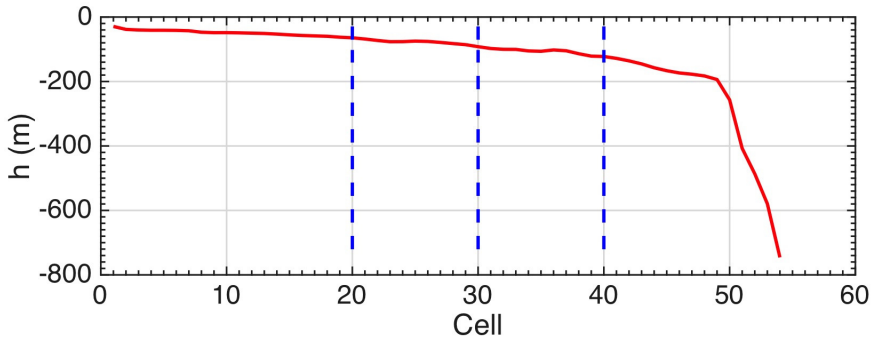

Figure 2.12: Bathymetry transect along azimuth 70 (Fig. 2).

by calculating the same quantities one hour in the past, hence before tsunami arrival. An integration window of $T_c = 900$ s in the past was used, which was found to be a good compromise between obtaining stable estimates of the average correlations and capturing the transient effects caused by the current front. Based on these correlations, 3 one-hour time series of contrast functions were computed: $\Gamma_{20,11,1}$, $\Gamma_{30,11,1}$, $\Gamma_{40,11,1}$, from 5h 00 min to 6h 00 min and 6h 00 min to 7h 00 min UTC in Figs. 2.13a,c,e and Figs. 2.13b,d,f, respectively.

Assuming contrast thresholds of 0.3-0.4 or 0.2-0.4, Fig. 2.13 shows that, based on the contrast functions computed for rays 180, 225 and 235 over cells 30-40 (45-60 km), a first warning could have been issued by the TCA-TDA at 5h 49 min UTC (Fig. 2.13c) and confirmed at 5h 55 min UTC (Fig. 2.13e). This would have been triggered by the strong increase in contrast function on ray 180, over cells 40-50 (60-75 km). Based on the even more drastic increase in contrast function on rays 160 and 180 over cells 40-50 (Fig. 2.13f) confirmed by the large increase in contrast functions of the entire group of rays over cells 30-40 (Fig. 2.13d), a second alert could have been issued at about 6h 35 min. Note that the non-monotonic behavior of the contrast function, with the occurrence of two maxima separated in time by 40 minutes (5h 55 min and 6h 35 min), is consistent with the tsunami alert map issued by the radar system, which is reproduced in Fig.

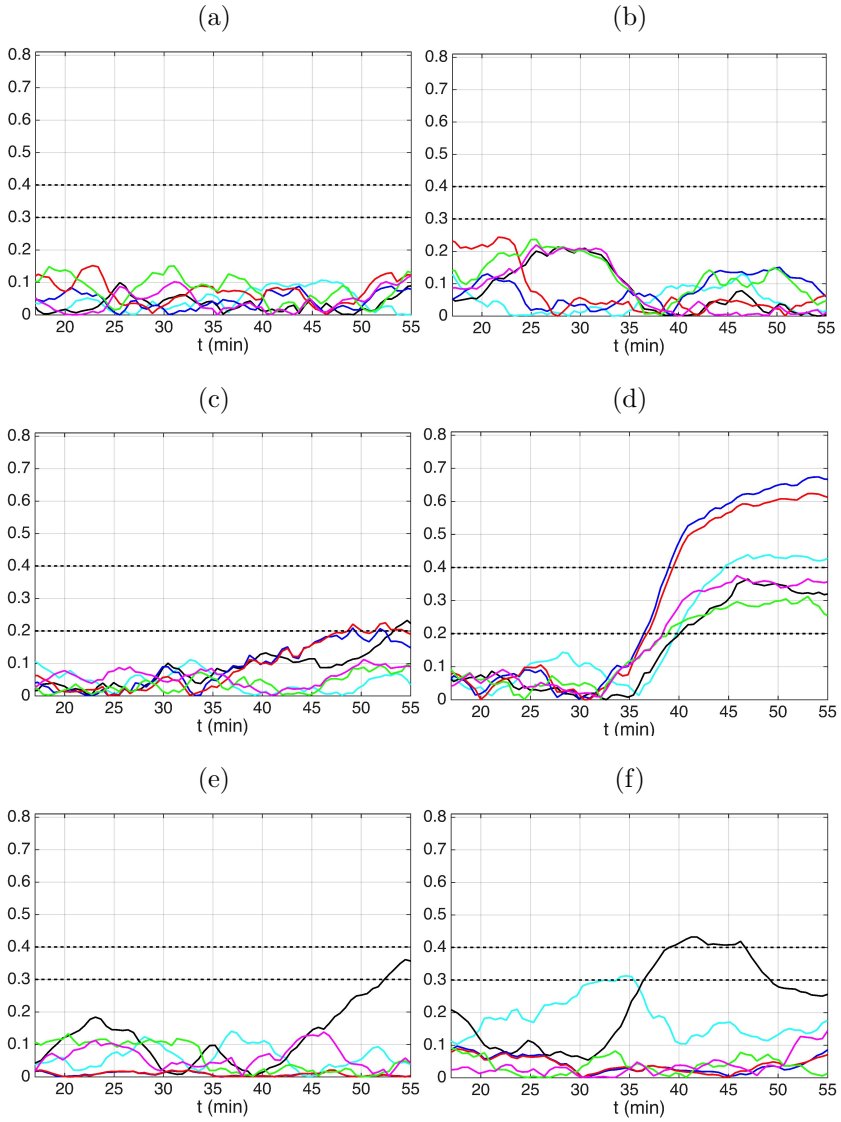

Figure 2.13: Zoom on 1h contrast function time series computed on October 14th, 2016 (day 288) with $T_c = 900$ s (in the past), along rays (Fig. 2): (cyan) 160, (black) 180, (blue) 225, (red) 285, (green) 165 (I) and (magenta) 165 (II). (a) and (b): $\Gamma_{20,11,1}$ (i.e., using the combination of gates (20:30)+1); (c) and (d) $\Gamma_{30,11,1}$; (e) and (f) $\Gamma_{40,11,1}$. The origin of time is 5h 00 min UTC in the leftward column (a, c and e) and 6h 00 min UTC in the rightward column (b, d and f). Arbitrary contrast threshold values have been marked by black dashed lines.

4 of (Dzvonkovskaya et al., 2017), where the alert threshold was reached twice at about the same time. The second alert could correspond to a second, stronger, incoming tsunami wave of tsunami. Unfortunately, the October 14th, 2016, storm caused an electrical outage at about 7h 00 min UTC, resulting in a few hours of interruption in the HF radar records. It would have been interesting to check for the arrival of subsequent waves and possible alerts, to confirm the tsunami-like nature of this event.

2.8 Probability of false alarms

In the TCA, the choice of the low and high contrast thresholds used for issuing a tsunami warning and an alert, respectively, is a delicate matter, which would require a thorough statistical analysis of radar time series under various oceanic conditions. In light of such an analysis, the selected thresholds would then result from a tradeoff between the probability of detection P(D) and the probability of false alarms P(F) . In the TCA, besides the selected thresholds, these probabilities will also depend on the choice of radar cells, integration time used to evaluate the correlations, and selected wave rays. While it is difficult to evaluate P(D), as this would require performing statistics over many actual tsunamis, P(F) can more easily be computed by estimating the probability of the contrast function to reach a given pre-set contrast threshold in the absence of a tsunami, which only requires a statistical analysis of archived radar data representative of various oceanic conditions. Thus, for a given contrast threshold Γ_ϵ, P(F) could be defined as the number of occurrences of the contrast function exceeding this threshold ($\Gamma > \Gamma_\epsilon$) divided by the total number of available values of the contrast function. Here, a very crude estimate of P(F) was calculated this way based only on the few hours/days of radar data under consideration. Figure 2.14 shows P(F) calculated as a function of the contrast threshold for 4 rays (160, 180, 225, 285; Fig. 2; only

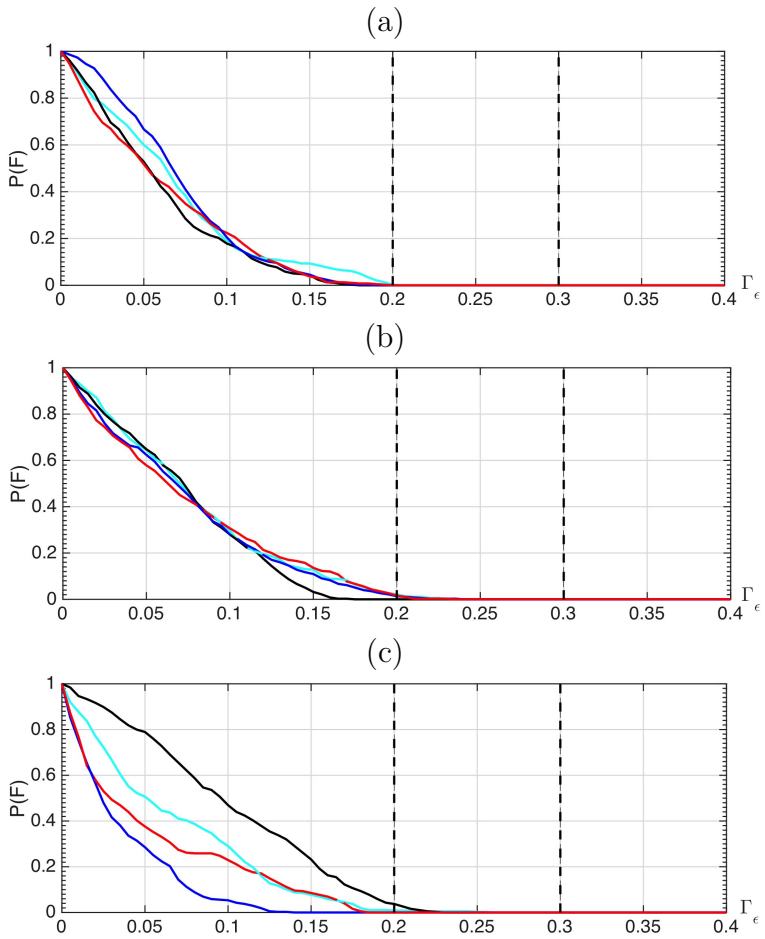

Figure 2.14: Same data and case as in Fig. 2.13. Probability of false alarms as a function of contrast function threshold, for a tsunami warning issued by the TCA, based on the magnitude of the radar contrast function: (a) $\Gamma_{20,11,1}$; (b) $\Gamma_{30,11,1}$; and (c) $\Gamma_{40,11,1}$, along rays (Fig. 2): (cyan) 160, (black) 180, (blue) 225 and (red) 285.

the most relevant rays for this case were processed) and contrast functions $\Gamma_{20,11,1}$, $\Gamma_{30,11,1}$,and $\Gamma_{40,11,1}$, used in the above meteo-tsunami detection study. As can be seen, a detection criterion based on the lowest thresholds 0.2 and 0.3 as used in Figs. 2.13c,e, would trigger a warning with a nearly zero rate of false alarms. Note that the estimation of P(F) could be refined by requiring that the contrast function exceed some threshold for several rays simultaneously (instead of one at a time), a task which has not been performed here.

The low and nearly zero probability of false alarms observed at the low (0.2)

and high (0.3) thresholds, respectively, confirm the effectiveness of an alert issued by the TCA, based on a threshold exceedence, such as done above in Fig. 2.13.

2.9 Discussion and conclusions

In this study, we further assessed and tested the tsunami detection ability of the Time Correlation Algorithm (TCA) proposed by Grilli et al. (Grilli et al., 2016a; Grilli et al., 2017), based on using actual data from the Tofino HF radar, either combined with realistic site specific tsunami simulations or "as is" for the potential meteo-tsunami event of October 14th, 2016. The analysis showed that the original TCA, initially validated with synthetic radar data, had to be refined and adjusted to account for the pre-existing correlation of radar signal backscattered from different cells, which is an artifact of the range and azimuth processing algorithms applied to the raw radar data. This was done by calculating a so-called contrast function, which quantifies the change in pattern of the mean correlation between pairs of neighboring radar cells upon tsunami arrival, with respect to a reference correlation computed in the recent past. In the paper, we showed, using two synthetic but realistic tsunamis case studies (for a large far-field co-seismic and a near-field SMF tsunamis), that a marked change in contrast function can be used as a relevant proxy for tsunami detection, which allows issuing a timely warning, confirmed by an alert. Note that different integration times were used in the TCA for the detection of the SMF and SSZ tsunamis, as the time scale of observation must be adapted to the tsunami characteristic period. This requires some a priori knowledge of the type of events that could possibly be detected at a given site. If tsunamis with very different time scales are plausible at the same location (e.g., longer tsunamis from seismic sources and shorter tsunamis from SMF or atmospheric sources), the TCA could easily be run in sequence (or in parallel) using multiple integration times.

The TCA tsunami detection performance was then further tested based on an actual event, which occurred on October 14th, 2016 and triggered a tsunami alert in the standard monitoring software running on the Tofino WERA system. Here, we performed an *a posteriori* (i.e., offline) analysis of both the meteorological and radar data acquired during the 2 hours surrounding the alert (i.e., from 5h 00 min to 7h 00 min UTC). The identification of both a propagating low pressure front along the US and Canadian West coasts, and a corresponding marked current front traveling at a local long wave celerity approximatively equal to the propagation speed of the low pressure front (95 km/h, see Fig. 2.10), support the hypothesis of a Proudman resonance mechanism generating a meteo-tsunami, although the occurrence of another type of unusual long wave phenomenon (e.g., seiche, storm surge, infra-gravity waves) cannot yet be ruled out. The exact nature of this event could be elucidated both by conducting a more thorough multi-sensor geophysical analysis and numerical simulations of tsunami generation by the observed pressure perturbation; the latter are the object of ongoing work. To assess its detection performance for this event, the TCA was applied along 6 rays covering the entire radar sweep area and the contrast function was evaluated for pairs of adjacent radar cells along the rays, in the close- (cells 20-30, 30-45 km), intermediate- (cells 30-40, 45-60 km) and far-ranges (cells 40-50, 60-75 km). Using an appropriate contrast function threshold value in the TCA, a first warning based on results from different rays could have been issued as early as 5h 49 min UTC.

The determination of optimal contrast function threshold values, in terms of maximizing the probability of detection and minimizing that of false alarms, would require a long-term assessment, over at least a full year of radar data corresponding to a large variety of oceanic conditions. Such a thorough statistical analysis was recently performed, using a Doppler-based algorithm, using HF radar data acquired

in Japan (Fuji and Hinata, 2017), where a detection probability could be estimated by combining synthetic (numerical) tsunamis with one month of actual HF radar measurements. It was found that the detection probability crucially depends on the tsunami to background current energy ratio. This limitation is in principle relaxed with the TCA, where the correlation analysis is performed on the radar signal itself and, hence, does not depend on the background current. In addition, the TCA performance could be refined by optimizing the cell ranges and rays used in the analysis. Both of these aspects will be addressed next in our work as they are necessary steps to develop a truly operational TDA system, which could be used as a useful complement to existing algorithms. This will be part of future work.

he authors wish to thank Helzel Messtechnik GmbH (in particular Dr. A. Dzvonkovskaya) for technical support to process the radar data and Ocean Networks Canada for providing the WERA HF radar data and support to the University of Rhode Island to conduct this research. C.-A. Guérin also acknowledges the CNRS, the University of Toulon, and the French-American Fulbright commission for supporting his sabbatical leave at URI.

List of References

Abadie, S., Harris, J. C., Grilli, S. T., and Fabre, R. (2012). Numerical modeling of tsunami waves generated by the flank collapse of the Cumbre Vieja Volcano (La Palma, Canary Islands) : tsunami source and near field effects. *J. Geophys. Res.*, 117:C05030.

Barrick, D. E. (1972a). First-order theory and analysis of MF/HF/VHF scatter from the sea. *IEEE Transactions on Antennas and Propagation*, 20(1):2–10.

Barrick, D. E. (1972b). Remote sensing of sea state by radar. In *IEEE International Conference on Engineering in the Ocean Environment, Ocean 72*, pages 186–192. IEEE.

Barrick, D. E. (1972c). Remote sensing of sea state by radar. In *Remote sensing of the Troposphere*, volume 12. VE Derr, Editor, US Government.

Barrick, D. E. (1972d). Remote sensing of the troposphere. *Remote Sensing of Sea State by Radar*, pages 1–46.

Barrick, D. E. (1978). HF radio oceanography: a review. *Boundary-Layer Meteorology*, 13(1-4):23–43.

Barrick, D. E. (1979). A coastal radar system for tsunami warning. *Remote Sensing of Environment*, 8(4):353–358.

Benjamin, L. R., Flament, P., Cheung, K. F., and Luther, D. S. (2016). The 2011 Tohoku tsunami south of Oahu: high-frequency Doppler radio observations and model simulations of currents. *J. Geophys. Res. (publ. online)*, pages 1–29.

Bernard, E. and Titov, V. (2016). Evolution of tsunami warning systems and products. *Phil. Trans. R. Soc. Lond. A*, 373(2053):20140371.

Crombie, D. D. (1955). Doppler spectrum of sea echo at 13.56 Mc./s. *Nature*, pages 681–682.

Dzvonkovskaya, A., Petersen, L., and L, I. T. (2017). Real-time capability of meteotsunami detection by WERA ocean radar system. In *8th Intl. Radar Symp. (IRS 2017, June 28-30, 2017, Prague, Czech Republic)*, page 10 pps.

Fine, I., Rabinovich, A., Bornhold, B., Thomson, R., and Kulikov, E. (2005). The Grand Banks landslide-generated tsunami of November 18, 1929: preliminary analysis and numerical modelling. *Mar. Geol.*, 215:45–57.

Fuji, R. and Hinata, H. (2017). Temporal variability of tsunami arrival detection distance revealed by virtual tsunami observation experiments using numerical simulation and 1-month hf radar observation. *Journal of Oceanography*, pages 1–17.

Grilli, S. T., Grosdidier, S., and Guérin, C.-A. (2016a). Tsunami detection by High Frequency Radar beyond the continental shelf. I. Algorithms and validation on idealized case studies. *Pure and Applied Geophysics*, 173(12):3,895–3,934.

Grilli, S. T., Guérin, C.-A., Shelby, M., Moran, P., Grosdidier, S., and Insua, T. L. (2017). Tsunami detection by High Frequency Radar beyond the continental shelf: II. Extension of algorithms and validation on realistic case studies. *Pure and Applied Geophysics*, 174(1):3,003–3,028.

Grilli, S. T., Harris, J. C., Tajalli-Bakhsh, T., Masterlark, T. L., Kyriakopoulos, C., Kirby, J. T., and Shi, F. (2013). Numerical simulation of the 2011 Tohoku tsunami based on a new transient FEM co-seismic source: Comparison to far- and near-field observations. *Pure Appl Geophysics*, 170:1333–1359.

Grilli, S. T., Ioualalen, M., Asavanant, J., Shi, F., Kirby, J. T., and Watts, P. (2007). Source constraints and model simulation of the December 26, 2004 Indian Ocean tsunami. *J Waterway Port Coastal Ocean Eng*, 133(6):414–428.

Grilli, S. T., O'Reilly, C., Harris, J., Tajalli-Bakhsh, T., Tehranirad, B., Banihashemi, S., Kirby, J., Baxter, C., Eggeling, T., Ma, G., and Shi, F. (2015). Modeling of SMF tsunami hazard along the upper US East Coast: Detailed impact around Ocean City, MD. *Natural Hazards*, 76(2):705–746.

Grilli, S. T., Shelby, M., Grilli, A., Guérin, C.-A., Grosdidier, S., and Insua, T. L. (2016b). Algorithms for tsunami detection by high frequency radar: Development and case studies for tsunami impact in british columbia, canada. In *Proc. 26th Intl. Ocean and Polar Engng. Conf. (ISOPE16, Rodos, Greece. June 2016).*, pages pps. 807–814. International Society of Offshore and Polar Engineers.

Guérin, C.-A. and Grilli, S. (2017). A probabilistic method for the estimation of ocean surface currents from short time series of HF radar data. *Ocean Modelling*. in revision.

Guérin, C.-A., Grilli, S., Moran, P., Grilli, A., and Lado, T. (2017). Tsunami detection by High Frequency Radar using a Time-Correlation Algorithm: performance analysis based on data from a HF radar in British Columbia. In *Proc. 27th Offshore and Polar Engng. Conf. (ISOPE17, San Francisco, USA. June 2017) (to appear).*

Gurgel, K.-W., Dzvonkovskaya, A., Pohlmann, T., Schlick, T., and Gill, E. (2011). Simulation and detection of tsunami signatures in ocean surface currents measured by HF radar. *Ocean Dynamics*, 61(10):1495–1507.

Heron, M. L., Prytz, A., Heron, S. F., Helzel, T., Schlick, T., Greenslade, D. J., Schulz, E., and Skirving, W. J. (2008). Tsunami observations by coastal ocean radar. *Intl J Remote Sensing*, 29(21):6347–6359.

Hinata, H., Fujii, S., Furukawa, K., Kataoka, T., Miyata, M., Kobayashi, T., Mizutani, M., Kokai, T., and Kanatsu, N. (2011). Propagating tsunami wave and subsequent resonant response signals detected by HF radar in the Kii Channel, Japan. *Estuarine, Coastal and Shelf Science*, 95(1):268–273.

Ioualalen, M., Asavanant, J., Kaewbanjak, N., Grilli, S. T., Kirby, J. T., and Watts, P. (2007). Modeling the 26th December 2004 Indian Ocean tsunami: Case study of impact in Thailand. *J. Geophys. Res.*, 112:C07024.

Kirby, S., Scholl, D., Von Huene, R., and Wells, R. (2013). Alaska earthquake source for the SAFRR tsunami scenario. Technical Report USGS Report, 2013, U.S. Geological Survey Open-File .

http://pubs.usgs.gov/of/2013/1170/b/, The SAFRR (Science Application for Risk Reduction) Tsunami Scenario.

Lipa, B., Barrick, D., Saitoh, S.-I., Ishikawa, Y., Awaji, T., Largier, J., and Garfield, N. (2011). Japan tsunami current flows observed by HF radars on two continents. *Remote Sensing*, 3(8):1663–1679.

Lipa, B., Isaacson, J., Nyden, B., and Barrick, D. (2012a). Tsunami arrival detection with high frequency (HF) radar. *Remote Sensing*, 4(5):1448–1461.

Lipa, B. J., Barrick, D. E., Bourg, J., and Nyden, B. B. (2006). HF radar detection of tsunamis. *J Oceanography*, 62(5):705–716.

Lipa, B. J., Barrick, D. E., Diposaptono, S., Isaacson, J., Jena, B. K., Nyden, B., Rajesh, K., and Kumar, T. (2012b). High frequency (HF) radar detection of the weak 2012 Indonesian tsunamis. *Remote Sensing*, 4:2944–2956.

Lipa, B. J., Parikh, H., Barrick, D. E., Roarty, H., and Glenn, S. (2014). High frequency radar observations of the June 2013 US East Coast meteotsunami. *Natural Hazards*, 74:109–122.

Ma, G., Shi, F., and Kirby, J. T. (2012). Shock-capturing non-hydrostatic model for fully dispersive surface wave processes. *Ocean Modeling*, 43-44:22–35.

Monserrat, S., Vilibić, I., and Rabinovich, A. B. (2006). Meteotsunamis: atmospherically induced destructive ocean waves in the tsunami frequency band. *Natural Hazards and Earth System Science*, 6:1035–1051.

Mori, N., Takahashi, T., and Group, . T. E. T. J. S. (2012). Nationwide post event survey and analysis of the 2011 tohoku earthquake tsunami. *Coastal Engineering Journal*, 54(01):1250001.

Stewart, R. H. and Joy, J. W. (1974). HF radio measurements of surface currents. In *Deep Sea Research and Oceanographic Abstracts*, volume 21(12), pages 1039–1049. Elsevier.

Tappin, D. R., Watts, P., and Grilli, S. T. (2008). The Papua New Guinea tsunami of 1998: anatomy of a catastrophic event. *Natural Hazards and Earth System Sciences*, 8:243–266.

Tehranirad, B., Harris, J., Grilli, A., Grilli, S., Abadie, S., Kirby, J., and Shi, F. (2015). Far-field tsunami hazard in the north Atlantic basin from large scale flank collapses of the Cumbre Vieja volcano, La Palma. *Pure Appl Geophysics*, 172(12):3,589–3,616.

Thomson, R. E., Rabinovich, A. B., Fine, I. V., Sinnott, D. C., McCarthy, A., Sutherland, N. A. S., and Neil, L. K. (2009). Meteorological tsunamis on the coasts of British Columbia and Washington. *Physics and Chemistry of the Earth Parts A/B/C*, 34(17):971–988.

Titov, V., Rabinovich, A., Mofjeld, H., Thomson, R., and Gonzalez, F. (2005). The global reach of the 26 December 2004 Sumatra tsunami. *Science*, 309(5743):2045–2048.

MANUSCRIPT 3

Tsunami Detection by High Frequency Radar: Comparison of Time Correlation and Q-Factor Algorithms

.

To be submitted to Natural Hazards

By

Patrick Moran[1], Stéphan T. Grilli[1], Charles-Antoine Guérin[2], Annette R. Grilli[1]

1. Department of Ocean Engineering, University of Rhode Island, Narragansett, RI 02882, USA

2. Université de Toulon, Aix Marseille Univ., CNRS IRD, MIO UM110, La Garde, France

Abstract

The development of a detection and early warning system for tsunamis can prevent massive loss of life along coastal communities. By using widely installed coastal current monitoring systems based on High Frequency (HF) radars, several different detection methods have been proposed, two of which are discussed and compared in this paper: (i) the Time Correlation Algorithm (TCA), developed by the authors in earlier work, which detects fluctuations in patterns of correlations of backscattered radar signal from the ocean surface; and (ii) the Q-Factor Algorithm, which uses pattern recognition in radial ocean current time series, generated through inverting radar Doppler spectra. Both algorithms are implemented and compared using actual data from a WERA HF radar located in Tofino, Canada, acquired on various days with different meteorological conditions. This data is combined with synthetic currents generated in realistic tsunami simulations with a long wave model, for: (i) a M9 co-seismic source in the Semidi Subduction Zone; and (ii) a submarine mass failure located on the continental slope, off of Tofino. Currents from these synthetic tsunamis are superimposed onto the radar signal using a convolution-like memory term. The algorithms are also tested using radar data acquired on 10/14/16, during which a current surge believed to be a meteotsunami impacted the area. Times at which detection occurs with the TCA and Q-factor algorithms are compared for these 3 cases, based on which we conclude that both algorithms perform similarly for the far-field co-seismic source; however the Q-factor algorithm fails to detect the SMF source entirely and detects the meteotsunami much later than the TCA.

3.1 Introduction

Tsunamis are among the most destructive natural hazards for densely populated low lying coastal areas. In the past 15 years, this was evidenced

by two megatsunamis that caused enormous damage and over 250,000 combined fatalities, in 2004 to Indian Ocean (IO 2014) countries (Titov et al., 2005; Grilli et al., 2007) and in 2011 to Japan (Grilli et al., 2013) (Tohoku 2011). Tsunamis are primarily generated by seismic activity, but can also be triggered by a variety of other processes such as volcanic activity (Abadie et al., 2012; Tehranirad et al., 2015), submarine mass failures (SMF), (Fine et al., 2005; Tappin et al., 2008; Tappin et al., 2014; Grilli et al., 2015; Grilli and Shi, 2017), and atmospheric disturbances. Tsunamis caused by atmospheric disturbances are referred to as "meteo-tsunamis" (Monserrat et al., 2006; Thomson et al., 2009).

Mitigating tsunami impact in terms of loss of life can be achieved by issuing an early enough warning to coastal populations, which can then evacuate to high ground. Currently in the US two tsunami warning centers are operated around the clock by NOAA, in Hawaii and Alaska, whose main mission is to issue tsunami warning and forecasts in real time during the course of an event. In particular, they aim at providing timely warning in the near field of tsunami sources. To do so, these warning centers use a combination of advanced numerical modeling and real time measurements at a variety of sensors, such as deepwater pressure sensors (a.k.a., DART buoys) (Bernard and Titov, 2016). Recent work has shown that shore-based High Frequency (HF) radars, given proper signal processing algorithms, can be used to detect tsunamis that are propagating towards the radar location, minutes to tens of minutes before tsunami landing, depending on continental shelf depth (Lipa et al., 2006; Lipa et al., 2012c; Lipa et al., 2014; Grilli et al., 2016; Lipa et al., 2016; Grilli et al., 2017; Guérin et al., 2017). Hence, HF radar could be used to issue an early warning of tsunami arrival, as part of operational tsunami warning systems. To date, most detections of tsunamis with HF radar were done in *a posteriori* analysis of data recorded during tsunami events (Lipa et al., 2012b;

Benjamin et al., 2016). One notable exception if the real time warning issued on October 14, 2016 by the WERA HF radar system deployed in Tofino, BC (off of the Pacific coast of Vancouver Island), after it detected what is believed to be a meteo-tsunami (Dzvonkovskaya et al., 2017; Guérin et al., 2017).

The possibility of detecting tsunamis with HF radars was first proposed by Barrick (Barrick, 1979). However, it is only in the wake of the devastating IO 2004 tsunami, that the detection capability of HF radars was confirmed by numerical simulations (Lipa et al., 2006; Heron et al., 2008; Gurgel et al., 2011) and in *a posteriori* analyses of radar data (Hinata et al., 2011; Lipa et al., 2011; Lipa et al., 2012b; Benjamin et al., 2016). HF radars can be used to measure various properties of the ocean surface (e.g., radial surface current, significant wave height,...), up to far ranges over the horizon (tens to a few hundred kilometers depending on radar characteristics; e.g., frequency, antenna power, environmental noise,...) and for a broad angular sweep area (up to $\sim$ 120 degrees or more). Typically, radial surface currents are reconstructed over a grid of radar cells (of a few by a few km in size), based on the shift they induce in the backscattered radar signal Doppler spectrum. Owing to the "Bragg Scattering" phenomenon (DD, ; Barrick, 1972a; Barrick, 1972c; Barrick, 1972b), the backscattered radar spectrum power is maximum for a specific ocean surface wavelength (L_B), which is equal to half the wavelength of the radar carrier electromagnetic (EM) waves (λ_{EM}). The Doppler shift in the spectrum at that particular wave frequency is then found to be proportional to the surface radial current. The high spatial coverage provided by HF radars and their nearly continuous monitoring over time makes them more suitable to detect tsunami-induced surface currents from non-seismic sources, such as near-field SMF or meteo-tsunamis, than traditional point-based sensors (e.g., pressure sensors or tide gauges). Such non-seismically generated tsunamis can oc-

cur at any location on or near the shelf break, and inherently complicate detection without the precursor of a strong earthquake.

In earlier work, Tsunami Detection Algorithms (TDA) have been proposed that detect the oscillatory nature of tsunami waves in space and/or time, in surface currents measured by HF radars (Lipa et al., 2012b; Lipa et al., 2012c; Lipa et al., 2014). Such TDAs, referred to here as "Doppler Method" (DM) TDAs, have limitations resulting from physical properties of the current inversion in the HF radar system, combined with the physical conditions in the radar sweep area. In order to be detectable, tsunami currents must be large enough to rise above a minimum threshold related to the frequency resolution of the radar Doppler measurements as well as other background currents (caused, e.g., by swells, tides, general circulation,...). While tsunami currents are very weak in the deep ocean, their strength rapidly increases as tsunamis move over the continental shelf and depth decreases. This means that, for a given HF radar system and signal processing algorithm, there is a depth threshold beyond which currents from a typical tsunami in the considered area are no longer measurable. In the HF radar system, the accuracy of the current inversion is inversely proportional to the carrier frequency and integration time used to process the backscattered signal; resolving small currents thus requires using large integration times T_i. However, this conflicts with the oscillatory nature of tsunami currents, since averaging data over a larger integration time reduces the estimated current magnitude, making tsunamis less detectable. A balance must be found between using a sufficiently large T_i, allowing for a reliable estimation of surface currents, but small enough to avoid averaging out tsunami currents. It should be noted that, assuming a typical T_i value of a few minutes, this limitation applies more to shorter period non-seismic tsunamis (T_t ∼5-10 min), than to longer period co-seismic tsunamis (T_t ∼10-40

min). Finally, the detection of surface currents by HF radars is limited by the radar Signal-to-Noise Ratio (SNR), which must be sufficiently large for a given T_i to guarantee reliable current estimation. This limits the use of DM-TDAs to either strong enough tsunami currents (typically found on the continental shelf), or weak currents but with a strong SNR (i.e., to short ranges). The latter was the case in the a posteriori detection of the weak 2012 Indonesian tsunami (Lipa et al., 2012a).

Lipa et al. (Lipa et al., 2012b) proposed one such DM-TDA, referred to as the Q-Factor, which is applied over radial bands, roughly parallel to bathymetric contours for typical coastal bathymetries. At all times, radial surface currents inverted by the radar are spatially averaged over the radial bands, yielding average current time series for each individual band. A pattern detection algorithm is then used to test for an oscillatory signature within the time series, indicative of an approaching tsunami. This method was developed and empirically tested, based on recorded HF radar data that included the effects of the Tohoku 2011 tsunami at 14 radar sites located in Japan and the US (Lipa et al., 2012b). They found the Q-factor could have issued a warning of tsunami arrival in average 19 min in Japan and 15 min in the US, before the tsunami was measured at tide gages.

To alleviate some of the limitations of DM-TDAs, Grilli et al. (Grilli et al., 2016) proposed a new tsunami detection algorithm for HF radar data, referred to as Time Correlation Algorithm (TCA) TDA, which does not require inverting surface currents but instead performs time-shifted correlations of the radar backscattered signal in pairs of cells located on the same tsunami wave ray. For long waves, the latter can be a priori computed based on the bathymetry in the radar sweep area, for a series of incident tsunami directions. An incident tsunami is detected when correlation patterns change. While Grilli et al. used both idealized tsunamis and bottom topographies, Grilli et al. (Grilli et al., 2017) demonstrated

the ability of the TCA-TDA based on state-of-the-art numerical simulations of both radar signal and tsunami currents. They showed that the new algorithm may be able to detect weaker tsunami currents (of a few cm/s) in deeper water, beyond the continental shelf, without averaging them out. More specifically, the TCA-TDA was validated using a radar simulator developed parameterized using the characteristics of the Tofino HF radar system (WERA radar manufactured by Helzel Messtechnik GmbH), combined with actual measurements of its SNR as a function of range (Grilli et al., 2017). The simulator was then applied to tsunami currents simulated in the area off of Tofino, using a long wave model, for two cases: (i) a Mw 9.1 far-field co-seismic tsunami, sourced in the Semidi Subduction Zone (SSZ; Fig. 3.1); and (ii) a near-field SMF tsunami triggered on the continental shelf slope, directly off of Tofino (Fig. 3.2). It was concluded that the TCA had the potential to detect incoming tsunamis further offshore, in deeper water, than using an algorithm based on currents directly inverted from the Doppler spectra (DM). Despite these encouraging results, no definitive conclusions could be drawn before the TCA algorithm was tested using actual radar data. This study was also limited due to the idealization of the radar signal in the simulator, the representation of background oceanic currents (assumed purely random), and ignoring ionospheric contamination as well as Radio Frequency Interferences (RFI).

In a subsequent study, Guéin et al. (Guérin et al., 2017) applied the TCA-TDA to actual data from the Tofino HF radar acquired for 5 days in 2016. Tsunami current effects were specified onto the recorded data in each radar cell by way of a "current memory term" (similar to a time dependent phase shift), for the same two cases, SMF and SSZ (Figs. 3.1 and 3.2). [This technique was first used by Gurgle et al. (Gurgel et al., 2011) to simulate the effects a tsunami event would have had on radar measurements.] An additional day was considered, October 14th, 2016, when

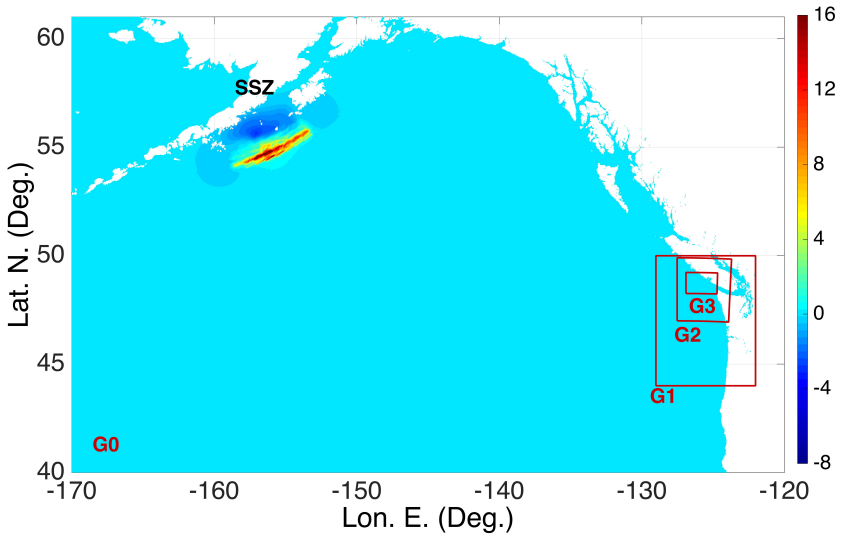

Figure 3.1: Zoom-in on part of the 2 arc-min grid G0 used in FUNWAVE-TVD's simulations of the M_w 9.1 co-seismic tsunami sourced in the Semidi Subduction Zone (SSZ); red boxes mark boundaries of nested model grids off of Vancouver Island, BC: G1 (0.6 arc-min), G2 (270 m), and G3 (90 m). The color scale (meters) is the initial surface elevation of the SAFRR seismic source used in simulations (see Grilli et al., 2017a).

the standard algorithm in the WERA system had issued a tsunami warning, later identified as the possible occurrence of a meteo-tsunami in the radar sweep area (Dzvonkovskaya et al., 2017). For the SSZ and SMF tsunamis, the TCA issued an early detection for both sources in all 6 days. To do so, however, the original TCA proposed by Guéin et al. (Guérin et al., 2017) had to be modified due to the nature of actual radar data, which has pre-existing correlation between neighboring radar cells as a result of the beam-forming and direction-finding algorithms used in the WERA radar system. A new correlation contrast function, which compares the current and past signal correlation values, was introduced that led to a new detection criteria in the TCA, when this function raised beyond some threshold.

As the Q-factor DM-TDA approach proved successful in past work for some types of tsunamis and depth ranges, it is of interest comparing its performance to the proposed TCA-TDA and investigate whether a more efficient "hybrid" method-

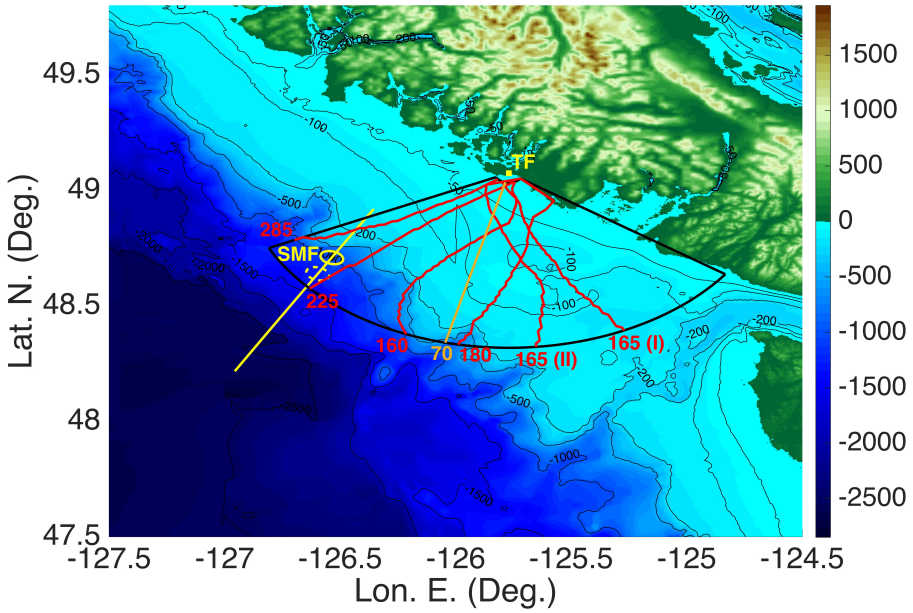

Figure 3.2: Bathymetry and topography (color scale and contours) of 270 m resolution grid G2 used in simulations of the SMF tsunami (Grilli et al., 2017). Black lines outline the sweep range of the Tofino WERA HF radar (TF; ■). The solid yellow ellipse ($w = 8$ by $b = 6$ km centered at 48.70822 Lat. N. and -126.53669 Lon. E.) marks the initial position of the SMF, with the direction of failure marked by the yellow line (209 deg. clockwise from N, with $s_f = 9$ km downslope) to its final position marked by the dashed yellow ellipse. Numbered red solid lines mark 6 wave rays used to apply the TCA-TDA, the brown line is a selected azimuth (70th).

ology based on HF radar data can be developed that combines both approaches. This study also aims at improving our overall understanding of the capabilities and limitations of the two TDA methodologies. After summarizing the HF radar tsunami detection methods, a direct comparison between the two TDA methods, as proposed by their authors, is made. Work is done using raw radar signal from the WERA HF radar located in Tofino, BC.

3.2 Principles of HF radar measurement of tsunami currents

Tsunami detection by HF radar is based on identifying the signature in the radar signal of an incoming tsunami wave train. The so-called DM-TDAs are based on radial surface currents inverted from the radar backscattered EM signal Doppler spectra. Since Crombie (DD,), it has been known that the dominant contribution to the radar signal backscattered from the sea surface, known as sea echo, corresponds to the resonant "Bragg" wave. The latter has a wavelength, half that of the radar EM wavelength,

$$L_B = \frac{\lambda_{EM}}{2} = \frac{gT_B^2}{2\pi} \quad \text{with} \quad \lambda_{EM} = \frac{c_{EM}}{f_{EM}} \tag{3.1}$$

where, assuming deep water ocean waves, the Bragg wave period T_B is found from the linear dispersion relationship, c_{EM} = 299,700 km/s, the speed of light in air, and g = 9.81 m/s^2, the gravitational acceleration. For the Tofino WERA radar, whose carrier EM frequency is f_{EM} = 13.5 MHz, we find L_B = 11.1 m and $T_B \simeq$ 2.67 s. Wind waves of this period are widespread on the ocean surface, even for very low wind, and hence a clear radar signal will be obtained in most situations. For the same radar, Eqs. 3.1 yield the Bragg wave frequency, $f_B = 1/T_B = 0.375$ Hz, at which maximum power is found in the sea echo spectrum; actually at $\pm f_B$, for waves moving radially towards or away from the radar.

In the presence of radial surface currents of velocity $\pm U_r$ a Doppler shift

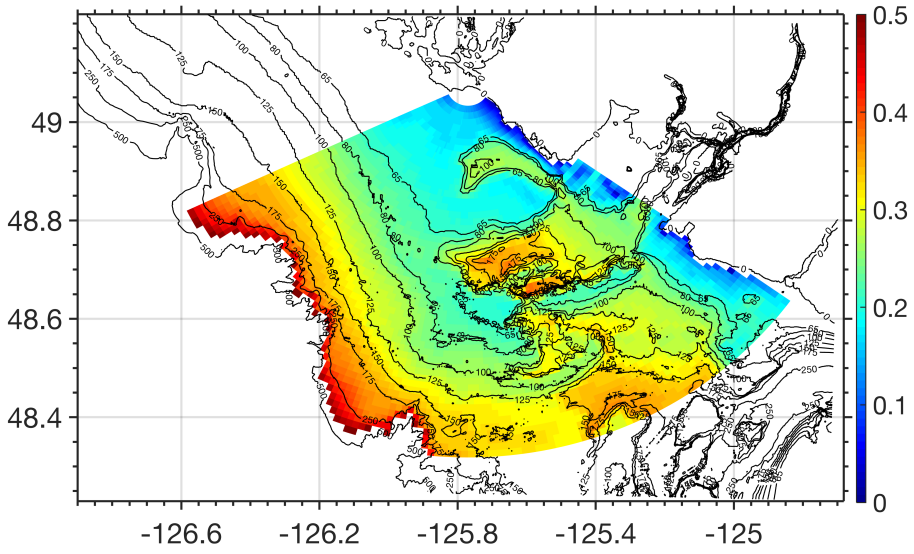

Figure 3.3: Minimum detectable tsunami elevation in the Tofino radar sweep area (color scale in meter), based on LWT Eqs. 3.3 and 3.4, with $\Delta U_r^{\min} = 0.084$ m/s (for $T_i = 132$ s). Note, at each location, the tsunami is assumed to propagate in the direction radial to the radar and a 0.5 elevation cutoff has been applied.

appears in the sea echo spectrum given by,

$$\Delta f_B = \pm \frac{2U_r}{\lambda_{EM}} = \pm \frac{U_r}{L_B} \tag{3.2}$$

which can be inverted to estimate the radial surface current for measured Doppler shifts. As the backscattered signal is averaged over each radar cell, Doppler shifts are also calculated for each radar cell and so are the inverted surface currents. Furthermore, the frequency resolution of the Doppler spectrum and, based on Eq. 3.2, that of the surface current are given by,

$$\Delta f_D = \frac{1}{T_i} \quad , \quad \Delta U_r = \frac{L_B}{T_i} \tag{3.3}$$

respectively, where T_i is the integration time. The latter is also the minimum measurable current by the radar; assuming $T_i = 132$ s, we find for the Tofino radar, $\Delta U_r^{\min} = 0.084$ m/s.

The horizontal current caused by a tsunami of surface elevation η_t in depth h in its instantaneous direction of propagation can be estimated with linear

long wave theory, which is a good approximation for tsunamis away from shore (Dean and Dalrymple, 1984),

$$U_t \simeq \eta_t \sqrt{\frac{g}{h(x,y)}} \tag{3.4}$$

Combining Eqs. 3.3 and 3.4, an estimate of the minimum detectable tsunami elevation can be derived for a given bathymetry (e.g., such as shown in Fig. 3.2), assuming that,at each location, the tsunami propagates in the direction radial to the radar. Fig. 3.3 shows an example of this in the Tofino radar sweep area. As expected, the farther away from the radar, the larger the depth and corresponding minimum detectable tsunami amplitude. Hence, when detecting a tsunami with a DM-TDA method, tsunami amplitude must either be very large in deeper water or detection will be limited to areas closer to the radar (which reduces warning times).

3.3 HF radar system used in this work

Since April 2016, a WERA HF radar, installed and operated by Ocean Networks Canada (ONC) near Tofino BC, has been operational to measure ocean surface properties in its sweep area off of the west coast of Vancouver Island (Canada) (Fig. 3.2). This radar, which is one component of ONC's real time ocean observing systems, came equipped with a basic real time tsunami detection software developed by Helzel Messtechnik GmbH. As part of ongoing collaboration with ONC, URI has worked on developing and validating improved TDAs to be eventually installed as a component of the WERA radar system. The radar operates at an electromagnetic frequency, f_{EM} = 13.5 MHz, is equipped with a 110 meter long array of 12 antennas centered at 49° 4' 24.82" N, 125° 46' 11.55" W, and has a sweep area with a 120 deg. beam opening ranging to 85-110 km, depending on sea state and atmospheric conditions (with a $\sim$ 12 deg. azimuthal resolution at the center of the beam). The orientation of the radar antenna array, 275 deg. from

N, clockwise and its 1angular opening result in a sweep area with one side that runs nearly parallel to the coastline southeast of Tofino (Fig 3.2). The radar signal system divides the sweep area into a grid of spatial cells, over which the received radar signal is averaged and radial surface currents are inverted, with a radial length $\Delta R = 1.5$ km and an angular opening $\Delta\phi_r = 1$ deg; hence cell width and area, $\Delta\mathbb{S} = R\Delta R\Delta\phi_r$ increases with range. At each time level separated by a small time interval Δt, the radar direction finding and beam forming algorithms process the raw radar signal in overlapping angular windows and compute instantaneous cell-average values of the radar signal at each cell center.

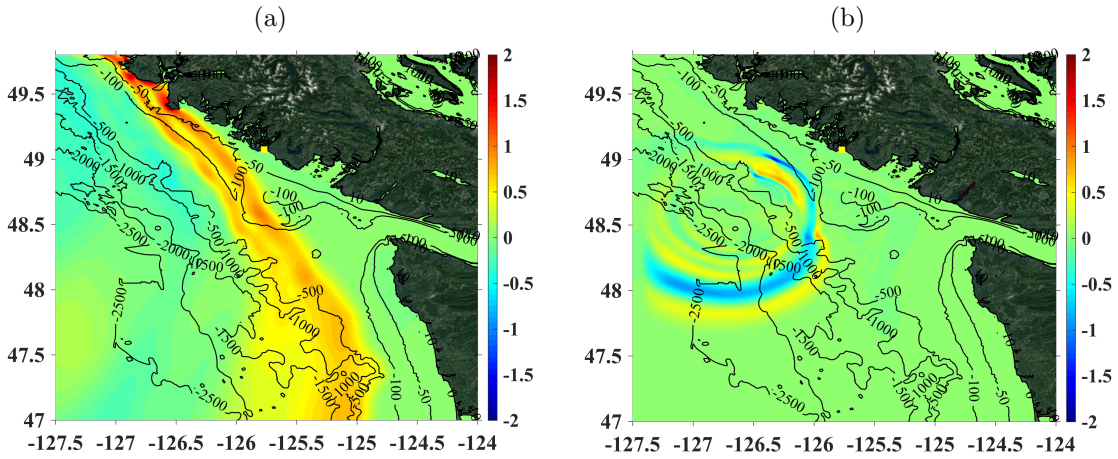

Figure 3.4: Instantaneous surface elevations (color scale in meters) simulated in grid G2: (a) with FUNWAVE-TVD for the SSZ source (Fig. 3.1), at t = 7,200 s (120 min); and (b) with NHWAVE for the SMF source (Fig. 3.2), at t = 800 s.

3.4 Numerical simulation of synthetic tsunamis

In earlier work, surface elevations and currents caused by two hypothetical tsunamis impacting the Tofino area were modeled and combined with either simulated or actual radar data (Grilli et al., 2017; Guérin et al., 2017): (i) a M_W 9.1 SSZ coseismic tsunami (Fig 3.1); and (ii) a near-field SMF tsunami with a 1.7 km^3 volume located at a 980 m of depth on the continental slope, 70 km off of

Tofino (Fig. 3.2). Here, the simulated horizontal tsunami radial surface currents, $U_{tr} = \mathbf{u}_t \cdot \mathbf{R}$ (with $\mathbf{R}$ the radial direction) are used in combination with actual radar data to test and compare a Q-factor based TDA to the TCA-TDA.

Details of source parametrization and tsunami simulations can be found in the referenced work. The SSZ tsunami source was designed by the SAFRR group as a worst-case scenario for northern California; it is also a plausible major tsunami case for the Pacific West Coast of Canada (Kirby et al., 2013). The Boussinesq long wave model FUNWAVE-TVD (Kirby et al., 2013) (Shi et al., 2012) was used to model the SSZ tsunami propagation by one-way coupling, using a series of nested spherical, then Cartesian, grids of increasingly fine resolution towards the coast of Tofino (G0-G3; Fig. 3.1 ; Fig. 3.4a). For the second synthetic tsunami, the SMF geometry was idealized as a sediment mound of quasi-Gaussian shape, with an 8 by 2 km elliptical footprint and maximum thickness of 100 m (Fig. 3.2). Tsunami generation was modeled in grid G2 as a rigid slump with a $s_f = 9$ km runout, using the non-hydrostatic model NHWAVE (Ma et al., 2012) (Grilli et al., 2015) with 5 boundary conforming layers in the vertical direction. Simulations were then continued in FUNWAVE-TVD, first in grid G2 and then by one-way coupling in grid G3 (Fig. 3.4b). In both cases shown in Fig. 3.4, time is measured from the initial time ($t = 0$) corresponding to the initiation of the tsunami wave train at the source. It takes approximately 2 hours and 20 minutes for the SSZ tsunami to reach the shore of Vancouver Island near Tofino, and only 20 minutes for the SMF tsunami. As FUNWAVE-TVD's finest resolution grid G3's 90 m resolution was much smaller than most radar cells' area, a large number of grid cells were averaged to compute the tsunami radial current within each radar cell.

3.5 Inversion of radial currents

A DM-TDA such as the Q-factor requires ocean surface currents. Here, we briefly summarize how these are computed by inverting radar Doppler spectra, on the basis of the frequency shifts they induce (Eq. 3.2 and 3.3). To compute Doppler spectra the raw radar data time series, corresponding to each radar cell in the sweep area, are sampled based on the radar station integration window duration, T_i (here 132 s), yielding $M = T_i/\Delta t$ data points in each sample spaced out by time Δt (here 0.26 s; i.e., $M = 508$). The spectrum at time t_s is computed by performing a FFT of the signal $V(t)$ for $t \in [t_s - T_i, t_s]$ as,

$$I(f_D, t_s) = \frac{1}{T_i} \left| \int_{t_s - T_i}^{t_s} w((t - T_i)/\Delta t)\, V(t) e^{2i\pi f_D t} \mathrm{d}t \right|^2 \tag{3.5}$$

A Hann window, $w(n)$ was applied in Eq. 3.5 to smooth out discontinuities at the beginning and at the end of the radar time series ($n = 1, ...M$),

$$w(m) = \frac{1}{2}\left(1 - \cos\left(\frac{2\pi m}{M-1}\right)\right) \tag{3.6}$$

From the Doppler spectrum, the surface current, averaged over a given radar cell (tilde) and over time T_i (overbar) is finally found as,

$$\overline{\tilde{U_r}}(t_s) = L_B(f_D^{max}(t_s) \pm f_B) \tag{3.7}$$

where f_D^{max} denotes the frequency band containing the maximum backscattered signal energy in the spectrum.

An example of the Doppler inversion method is shown in Fig. 3.5, for the radar signal of Julian day in 2016, over which the SSZ tsunami currents were superimposed using the method discussed in the next section. In this example the current inversion was completed every 33 s (i.e., spacing of t_s). The inverted current follows the pattern of the synthetic tsunami currents, except for the addition of a background current that was present in the radar data. This does not affect current or signal correlations in the algorithms.

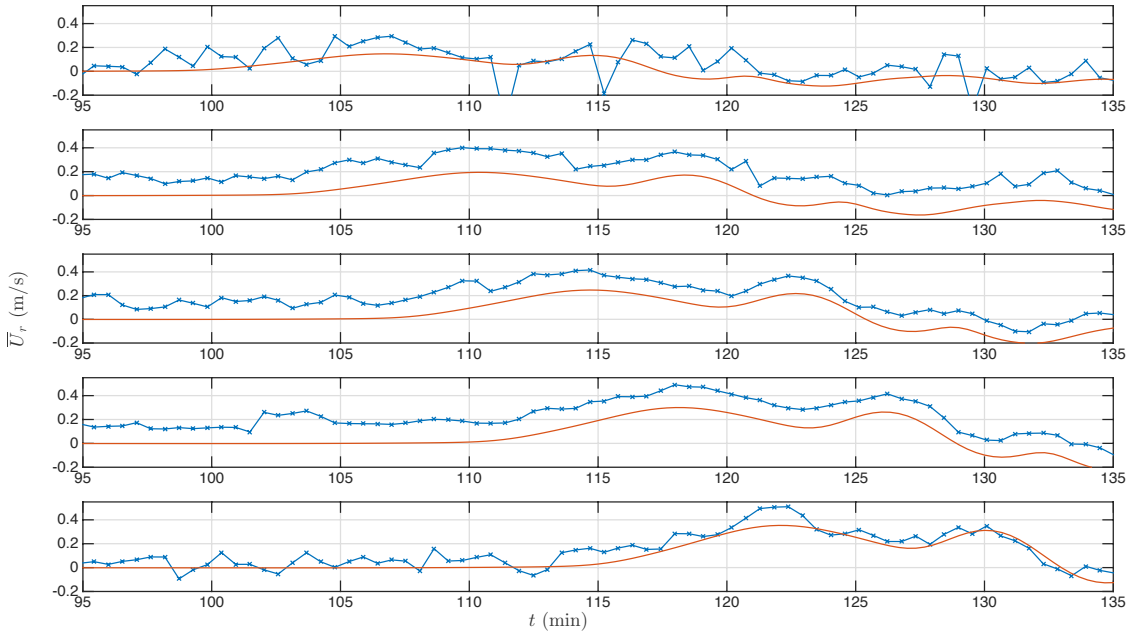

Figure 3.5: Comparison of cell/time averaged SSZ synthetic tsunami currents specified onto the radar signal of day 238 (red lines), with currents retrieved by inversion of the signal Doppler (blue lines). Both radar signal and current are those of the northernmost radar cells in every third spatial band of Fig. 3.6 (from offshore to onshore, from top to bottom).

3.6 Principle of TDAs used in this work

3.6.1 The TCA-TDA

In view of the limitations of DM-TDAs discussed above, in terms of minimum tsunami current magnitude, Grilli et al. (Grilli et al., 2016; Grilli et al., 2017) developed the TCA-TDA as a means of detecting an approaching tsunami by directly analyzing radar signal time series without having to invert those for a radial surface current. Recognizing that tsunami current effects were already included in phase modulations of the normalized radar signal $V_q(t)$, they postulated that a tsunami could be detected when a marked change occurred in correlations of time series of radar signal in pairs of radar cells. Indeed, according to first-order Bragg theory, the normalized complex back-scattered signal received at time t from a given radar cell q takes the form,

$$V_q(t) = \alpha^+ e^{-2\pi i f_B t} + \alpha^- e^{+2\pi i f_B t} \tag{3.8}$$

where $\alpha^{\pm}$ are complex constant coefficients functions of sea state, range, and radar calibration. The radial surface current generated by an approaching tsunami $U_{tr}(t)$, will cause instantaneous Doppler frequency shifts in the radar signal, of the form given by Eq. 3.2, whose cumulative effect can be expressed as the memory term,

$$\mathcal{M}(t) = \frac{1}{L_B} \int_{-\infty}^{t} U_{tr}(\tau) \mathrm{d}\tau \tag{3.9}$$

translating into instantaneous phase shifts. $\exp\left(2\pi i \mathcal{M}(t)\right)$ in Eq. 3.8, such that,

$$V_q(t) = \left(\alpha^+ e^{-2\pi i f_B t} + \alpha^- e^{+2\pi i f_B t}\right) e^{2\pi i \mathcal{M}(t)} \tag{3.10}$$

This approach was further optimized by observing that, according to linear long wave theory (Dean and Dalrymple, 1984), tsunamis propagate along wave rays that only depend on depth and hence can be pre-computed by solving the eikonal equation of geometric optics (with wave celerity being simply, $c = \sqrt{gh}$).

Fig. 3.2 shows examples of 6 wave rays computed over the Tofino radar sweep area from a variety of incident tsunami directions. Note, the linear long wave approximation holds, and wave rays are independent from tsunami period, when the local wavelength, $L_t = cT_t \gg 20h$ or $T_t \gg 20\sqrt{h/g}$. For the minimum period of tsunami sources considered here, $T_t = 5$ or 20 min, this applies when $h < 2,207$ or 35,316 m. Thus, all far-field seismic tsunamis are long waves that will propagate into the Tofino radar sweep area along the same wave rays. This also applies to shorter period near-field tsunamis, such as from SMF sources, generated in less than 2,207 m of depth.

Furthermore, for linear long waves, the tsunami travel time along wave rays can also be easily computed as a function of bathymetry; considering a pair of cells, say p and q, the travel time between these reads,

$$\Delta t_{pq} = t(\mathbf{R}_q) - t(\mathbf{R}_p) = \int_{\mathbf{R}_p}^{\mathbf{R}_q} \frac{\mathrm{d}r}{\sqrt{gh(\mathbf{R})}} \tag{3.11}$$

with $\mathbf{R}(x, y)$ the radial position vector form the radar location. A given tsunami current pattern occurring in cell p at time t should thus propagate to and occur in cell q at time $t + \Delta t_{pq}$. Such tsunami current time series in cells p and q should thus be highly correlated when time shifted by Δt_{pq}. This property was verified by Grilli et al. (Grilli et al., 2016; Grilli et al., 2017) for numerically simulated synthetic tsunamis.

The TCA assumes that, since tsunami surface currents modulate the radar signal through the memory term $\mathcal{M}(t)$ (Eq. 3.10), the same property should apply to correlations of radar signal time series measured at pairs of cells located on the same wave ray, when one of these is similarly shifted by the tsunami propagation time between the cells, i.e.,

$$C_{pq}(\tau; t) = \left| \frac{1}{T_c - \tau} \int_{I_t} V_p(t' + \tau) V_q^*(t' - \Delta t_{pq}) \mathrm{d}t' \right| \tag{3.12}$$

where the integration time interval is defined as, $I_t = [t - T_c, t - \tau]$ and $\tau \in [-T_l/2, T_l/2]$ is an additional time lag, with the length of the time window $T_l < T_c$, the correlation time, and the star indicates the complex conjugate. The correlation time T_c should be sufficiently large to capture a meaningful part of the incident tsunami current oscillations, i.e., be at least one-third to one-half the tsunami period T_t. Note that I_t decreases as τ increases, because the correlation computed at t does not depend on the future radar time series (i.e., when $t' + \tau > t$). This reduction of I_t is compensated by the normalization factor $1/|T_c - \tau|$, which ensures that the correlation of two uniform signals remains flat and prevents an artificial correlation peak near the zero time lag. The TCA thus aims at improving the detection ability of HF radars by eliminating the need for current inversion (and hence its limitations) while accounting for physical properties of tsunami waves, i.e., their large-scale spatial and temporal coherency and propagation properties along wave rays. Note that at far range, where detection is most desired, most wave rays can be assumed to be more or less directed towards the radar (e.g., see Fig. 3.2), so that the effect of projecting currents from the tangential direction to a ray to the radial direction is negligible.

Based on Eqs. 3.11 and 3.12, the maximum signal correlation should occur near $\tau = 0$. Therefore, a change in pattern of a previously computed correlation C_{pq} near $\tau = 0$ should indicate that a tsunami is propagating through the radar sweep area. Grilli et al. (Grilli et al., 2016; Grilli et al., 2017) showed that this approach worked well to detect synthetic tsunamis superimposed onto simulated radar data. By contrast, when using actual radar data, large pre-existing signal correlations were observed between neighboring radar cells, which resulted from the beam-forming and direction-finding algorithms used in the WERA radar system (Guérin et al., 2017); hence simply observing a marked increase in corre-

lation no longer worked to detect an approaching tsunami. However, Guérin et al. (Guérin et al., 2017) showed that an approaching tsunami still changed the pattern of signal correlations in a marked way, which could be quantified by a contrast function. They further noted that tsunami detection was improved when averaging up radar signal correlations computed between N pairs of cells located along a section of the same wave ray. Such correlations, $C_{p,p+K}(\tau;t)$, are computed with Eq. 3.12 between cell p and its Kth neighbor $p+K$, for $p = p_0, ..., p_0+N-1$, and their average scaled by its maximum value thus reads,

$$C_{p_0,N,K}(\tau;t) = \frac{1}{N}\sum_{p=p_0}^{p_0+N-1} \frac{C_{p,p+K}(\tau;t)}{\max_\tau\{C_{p,p+k}(\tau;t)\}} \tag{3.13}$$

The contrast function proposed by Guérin et al. compares this correlation with a *reference* correlation computed at an earlier time (e.g., 30 to 60 min before present), over the same cells and during a time interval $T_i/2$, i.e.,

$$\Gamma_{p_0,N,K}(t) = \frac{\int_{-T_i/4}^{T_i/4}\left(C_{p_0,N,K}(\tau;t) - C^{ref}_{p_0,N,K}(\tau;t)\right)\mathrm{d}\tau}{\int_{-T_i/4}^{T_i/4}\left(C_{p_0,N,K}(\tau;t) + C^{ref}_{p_0,N,K}(\tau;t)\right)\mathrm{d}\tau} \tag{3.14}$$

Guérin et al. (Guérin et al., 2017) showed that, for the SSZ and SMF tsunamis, as well as for the 10/14/16 meteo-tsunami candidate, this contrast function clearly increased when a tsunami was propagating along the selected wave ray, causing a change in pattern of the mean correlation over N cells, with respect to its reference value. They showed that, for the SSZ and meteo-tsunami that arrived from the far-field, the ray section of N cells could be selected in the far-range of the radar sweep area and hence an early detection could be issued. For the near-field SMF tsunami, the ray section needed to be closer to the radar, near the middle of the sweep area, but a fairly early warning could still be issued.

Guérin et al. (Guérin et al., 2017) proposed using an increase in contrast function beyond some threshold as the new detection criterion for the TCA-TDA

and run sensitivity analyses to estimate the best value of the treshhold that reduced the probability of false positives in the detection.

3.6.2 The Q-factor TDA

First Introduced by Lipa et al. (Lipa et al., 2012b) the Q-Factor TDA is based on an empirical method relying on physical properties of tsunami waves, consistent with linear long wave theory. Due to refraction, the crests of tsunami waves propagating in shallower water gradually bend to align with bathymetric contours (e.g., Fig. 3.4a). As previously noted, as depth decreases, surface currents associated with tsunami waves are stronger and hence increasingly measurable by a HF radar (e.g., Fig. 3.3). The Q-Factor is a pattern recognition algorithm that takes advantage of these spatial characteristics of tsunamis. The pattern being tested for is the detection of a steadily increasing or decreasing tsunami current along bathymetric contours located at increasing range from the radar. To do so, N spatial "bands" are defined as roughly parallel to bathymetric contours. Radial surface currents inverted by the radar are averaged across each individual band, thus creating time series of currents for each band, $\overline{U_{tr}^{n}}(t)$ ($n = 1, ..., N$; for increasing range).

The Q-factor algorithm tests for current fluctuations in band-averaged current time series that are consistent with an incoming tsunami. The algorithm considers inverted surface current time series in 3 successive bands range-wise, $(k, k{+}1, k{+}2)$, $[\overline{U_{tr}^{k}}(t), \overline{U_{tr}^{k+1}}(t + T_i), \overline{U_{tr}^{k+2}}(t + 2T_i)]$ (for $k = 1, ..., N - 2$). As noted, the band-averaged current time series are increasingly time-shifted as a function of the radar integration time T_i, when the distance to the radar increases. The Q-Factor value is then calculated as,

$$q(t) = V(t)\, D(t)\, C(t) \tag{3.15}$$

with $V(t)$ a Velocity Increment Function, $D(t)$ a Velocity Deviation Function, and

$C(t)$ a Correlation Function. The Velocity Increment Function quantifies temporal changes $\Delta u_n(t)$ in band-averaged current velocity for the 3 bands, as,

$$V(t) = \sum_{n=k}^{k+2} \Delta u_n(t) \quad \text{with} \quad \Delta u_n(t) = \overline{U_{tr}^n}(t) - \overline{U_{tr}^n}(t - 2T_i) \tag{3.16}$$

The Velocity Deviation function is a statistical representation of the real time current measurements, compared to the current recorded in the previous hour. It is defined as the product of Gaussian reduced variables, γ_n computed for three adjacent bands,

$$D(t) = \prod_{n=k}^{k+2} \gamma_n(t) \quad \text{with} \quad \gamma_n(t) = \frac{\overline{U_{tr}^n}(t) - \mu_n(t)}{\sigma_n(t)} \tag{3.17}$$

where $\mu_n(t)$ is the time-averaged band-averaged current over the previous hour, and $\sigma_n(t)$ is the corresponding standard deviation. Finally, if the band-averaged velocity increases or decreases across all three spatial bands at times $t, t - T_i$, and $t - 2T_i$ the Correlation Function, $C(t)$ is set to 100, otherwise it is set to unity.

This method was developed and tested on recorded radar data from 14 different radar sites in Japan and the US, all of which were operational during the Tohoku 2011 tsunami and shown to be able to issue an a posteriori tsunami detection (Lipa et al., 2012b).

3.7 Application of the TCA and Q-factor TDAs to synthetic tsunami detection

3.7.1 Radar data

As in earlier work (Guérin et al., 2017), the raw radar signal recorded by the Tofino HF radar system was obtained for Julian days 200, 227, 238, 287, 289 in 2016 plus October 14th, 2016, at a sampling rate of $\Delta t = 0.26$ s. The signal was processed in range and azimuth using software developed by Helzel Messtechnik GmbH, which produced time series of complex backscattered signal, $V_q(t)$ for each radar cell q along 6 tsunami wave rays selected in the radar sweep area (Fig.

3.2). The effect of synthetic tsunamis on radar data was simulated by multiplying these time series by the memory term computed as a function of the simulated cell-averaged tsunami radial current velocity U_{tr} (Eqs. 3.9 and 3.10). To avoid spurious values sometimes observed in actual radar signal time series, and to equalize their magnitude at different ranges, re-centered and normalized complex values of the radar signal time series were used in the TCA-TDA,

$$S_q(t) = \frac{V_q(t) - \overline{V_q}}{|V_q(t)|} \tag{3.18}$$

where $\overline{V_q}$ is the temporal mean of the signal in the window of observation. This re-centering and normalization of the complex values of the radar signal time series was not used in the Q-Factor application.

3.7.2 Application of the TCA-TDA

Guérin et al.(Guérin et al., 2017) applied the TCA to the two synthetic tsunamis, SSZ (Fig. 3.1) and SMF (Fig. 3.2), which in most selected days issued a detection at 1h48' and 6' after the start of each tsunami, respectively (using a contrast function threshold of 0.2; see this reference for detail, and particularly their Figs. 4 and 6). Without the superposition of the tsunami current, the contrast function kept a stable low value below the detection threshold. They also applied the TCA to the radar data of 10/14/16, which contained the potential meteo-tsunami event, and showed that this triggered a detection in the algorithm at 5 h 49 min UTC (see their Fig. 13). Results of applying the TCA-TDA to the 2 synthetic tsunamis are presented later.

3.7.3 Application of the Q-factor TDA

To apply the Q-factor TDA, 13 spatial bands were selected in a region of the sweep area with fairly regular and shore-parallel bathymetry (Fig. 3.6), each approximately following bathymetric contours for 10 km and located at average

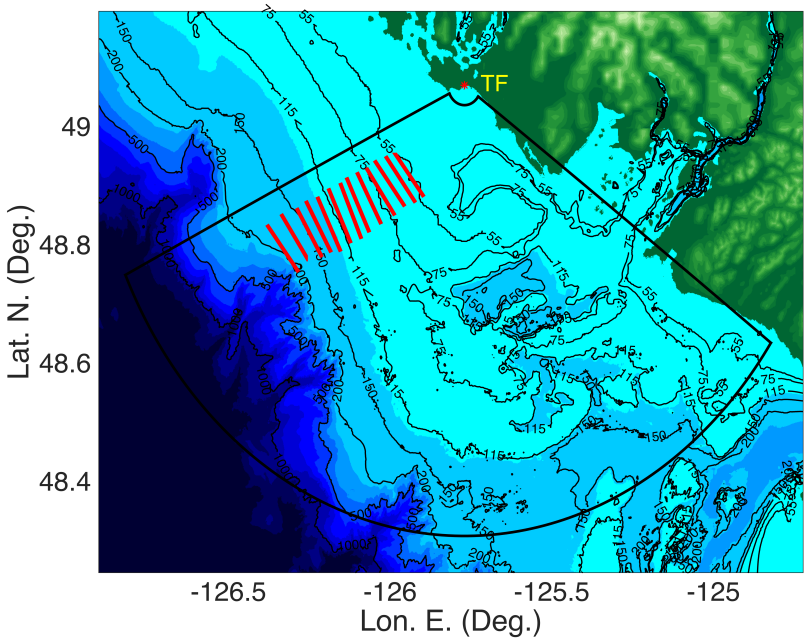

Figure 3.6: Spatial bands (red lines) used to apply the Q-factor TDA; 10 km long bands have been defined using bathymetry contours. Black lines mark the footprint of the radar sweep area, and the red start and TF label mark the radar location.

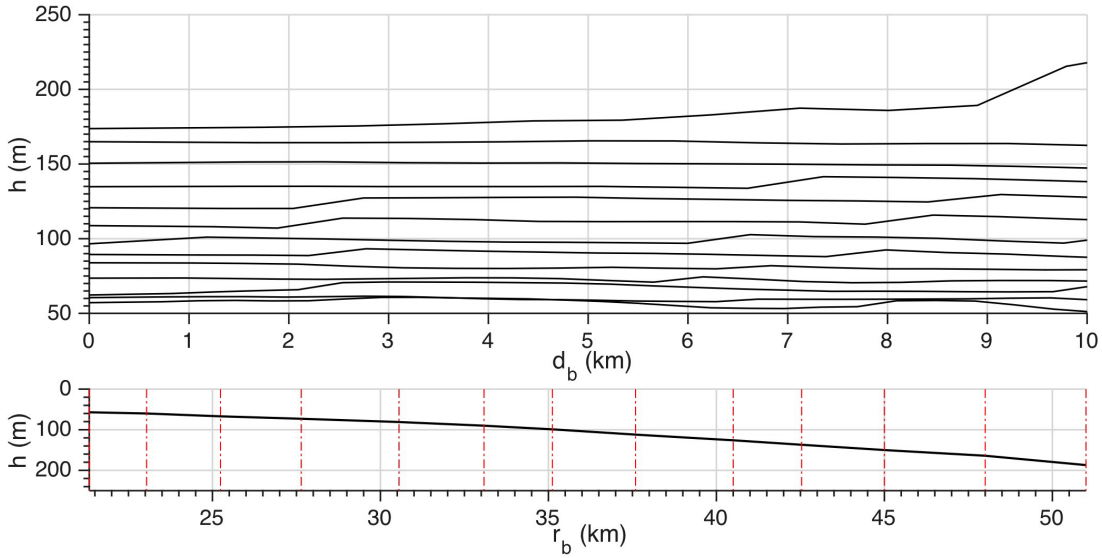

Figure 3.7: (top) Depth along 13 spatial bands (based on space-averaged bathymetry in corresponding radar cells; Fig. 3.6) used to apply the Q-factor TDA, as a function of distance d_b measured along each band (from south to north); and (bottom) averaged depth in each band, as a function of the average radial distance from the radar r_b (the band positions are marked by red dashed-dotted lines).

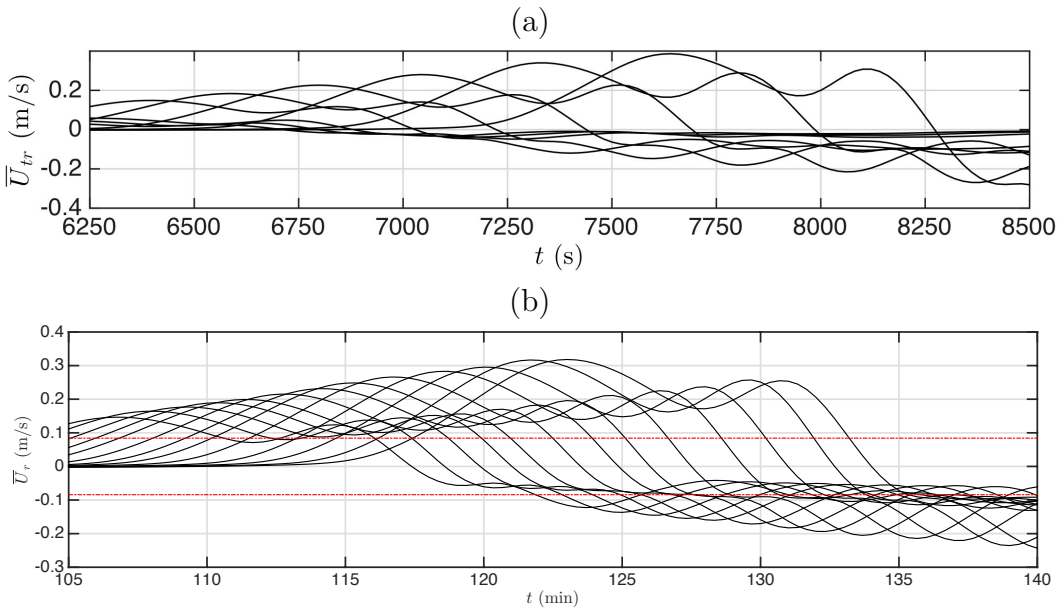

Figure 3.8: Tsunami radial current time series from SSZ simulations (Fig. 3.4): (a) cell-averaged at 9 stations along ray 225 (Fig. 3.2) used in the TCA-TDA (Grilli et al., 2017); and (b) averaged across bathymetry-defined spatial bands used in the Q-factor TDA (Fig. 3.6); red chained lines mark theoretical limits for minimum currents measurable with the Toffino HF WERA radar (~ 0.084 m/s).

radial distances $r_b = 21$ to 51 km from the radar. Other parts of the sweep area, e.g., southeast of the selected bands, have a more complicated bathymetry that would be less amenable for applying the Q-factor. Fig. 3.7 shows that depth is fairly constant along each selected band, except for the most distant one, which is located mostly over an extrusion of the continental shelf into deep water, with a portion lying over the steep drop-off; the average depth along each band varies from $\sim 60 - 180$ m.

With $N = 13$, the total number of triplets (i.e., made of three consecutive bands) on which to compute the Q-factor is $N - 2 = 11$. Note that bands in subsequent groups are overlapping in order to maximize the coverage of the Q-Factor. The Q-Factor TDA was applied to the same radar data as used in the TCA-TDA, on which both synthetic tsunamis, SSZ and the SMF, were successively superimposed, and its results compared to those of the TCA (see results below).

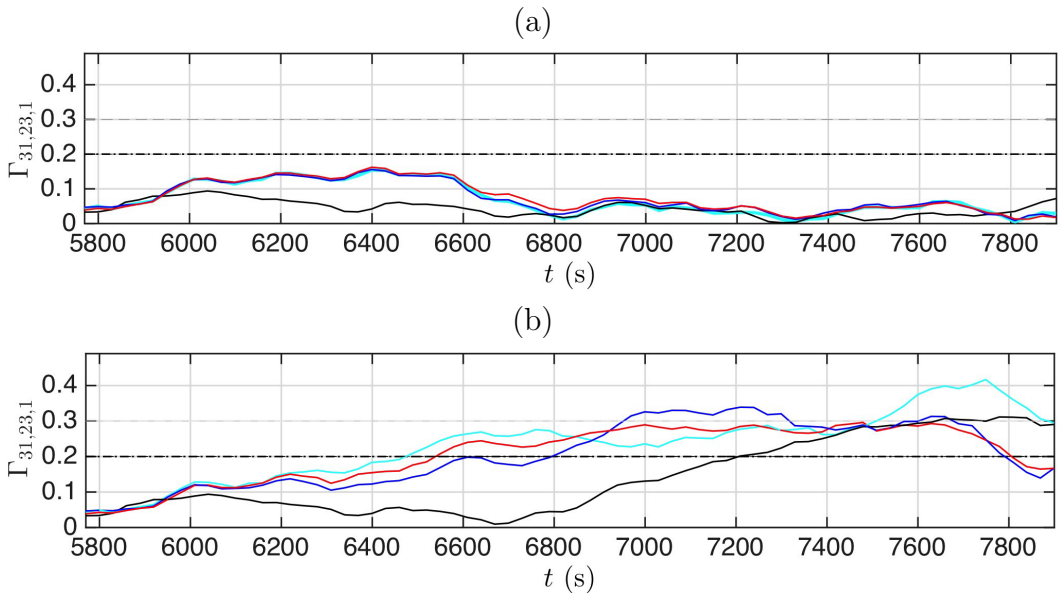

Figure 3.9: Application of the TCA-TDA to the SSZ tsunami. Time series of contrast function (Eq. 3.14) computed for Julian day 238 in 2016, using $T_c = 1,200$ s, for $p_o = 31$, $N = 23$ and $K = 1$, without (a) and with (b) the SSZ radial surface tsunami currents (e.g., Fig. 3.8a) superimposed to the radar signal (Eqs. 3.9 and 3.10), along rays (Fig. 3.2): (cyan) 160, (black) 180, (blue) 225, and (red) 285; based on a 0.2 contrast threshold (horizontal dashed lines), a first warning would be issued at 6,480 s (1h48') into the event (Guérin et al., 2017).

3.8 Comparison of the TCA and Q-factor TDAs for synthetic tsunami detection

3.8.1 The far-field SSZ co-seismic tsunami

Figures 3.8a,b show time series of cell- or band-averaged tsunami radial surface currents $\overline{U}_{tr}(t)$, computed at 9 stations along ray 225 (Fig. 3.2), as used in the TCA-TDA (Grilli et al., 2017; Guérin et al., 2017), or computed at 13 spatial bands (Fig. 3.6), as used in the standard Q-factor TDA, respectively. The average depth varies at the 9 stations from $\sim 50 - 1400$ m and $\sim 60 - 180$ m at the 13 spatial bands (Fig. 3.7).

As in Guérin et al. (Guérin et al., 2017), the TCA-TDA is first applied to the 5 Julian days of radar data (200, 227, 238, 287, 289 in 2016), on which the SSZ tsunami radial surface currents were superimposed (e.g., Fig. 3.8a) using Eqs. 3.9 and 3.10, for the hour of time series data under investigation, and not on the previous reference hour. Time shifted signal correlation $\mathcal{C}_{31,23,1}(\tau, t)$ and contrast function $\Gamma_{31,23,1}(t)$ time series were computed along wave rays 160, 180, 225, and 285 (Fig. 3.2), for $p_o = 31$, $N = 23$ and $K = 1$ (i.e., in radar cells 31 to 53 corresponding to ranges from 45 to 79.5 km, correlated with those in the neighboring cells range-ward), using an integration correlation window $T_c = 1,200$ s. Fig. 2.4 shows that the contrast function $\Gamma_{31,23,1}(t)$ computed for day 238 clearly increases as tsunami waves propagate into the radar sweep area (b); without the tsunami, no marked increase occurs (a). Based on a low contrast threshold of 0.2, a first warning would be issued at $t = 6,480$ s (1h48'). As noted by Guérin et al., the TCA tsunami detection based on the contrast function is effective even though the magnitude of tsunami-induced currents is quite small in cells 31 to 53 (less than 0.075 m/s from cells 34 to 53). Similar results and detection times (see Figs. 3.18, 3.19, and 3.20 in Appendix for Julian days 200, 227 and 289) were obtained using radar data for the other four selected days, even on day 289, which had a

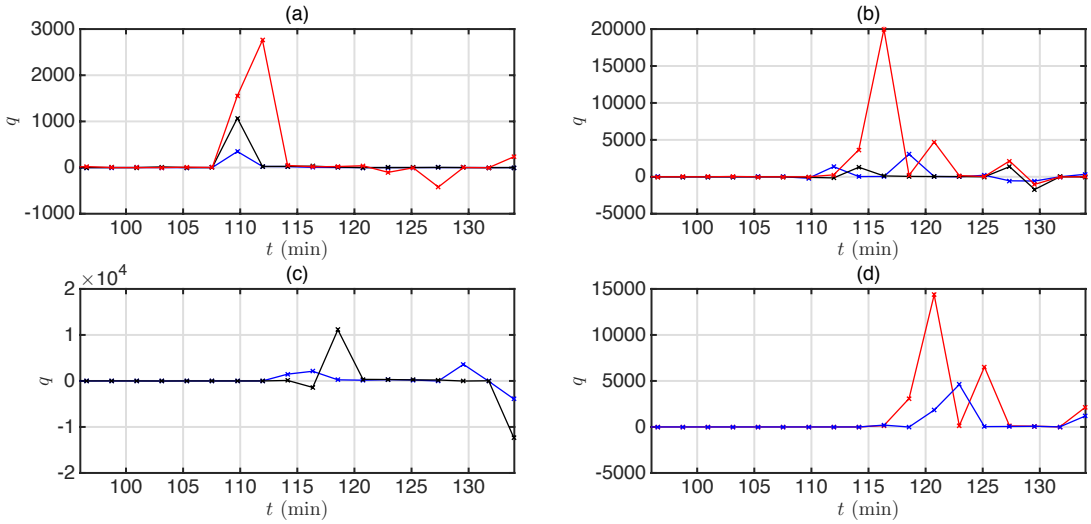

Figure 3.10: Application of the Q-factor TDA to the SSZ tsunami. Time series of Q-factor q values for Julian day 238 in 2016, using T_i = 132 s and spatial bands located at radial distances from the radar (Figs. 3.6 and 3.7) r_b = (a) 42-48 km (blue), 39-45 km (black), and 36-42 km (red); (b) 33-39 km (blue), 31.5-36 (black), and 30-33 km (red); (c) 27-31.5 km (blue) and 24-30 km (black); and (d) 22.5-27 km (red) and 21-24 km (blue).

strong swell.

The Q-factor TDA is applied next to the same days of radar data combined with the SSZ tsunami radial currents, for the 13 spatial bands of Fig. 3.6, which are separated in range by 1.5 - 3 km (1-2 radar cells), using T_i = 132 s. Radial surface currents are first computed using Eqs. 3.6 - 3.7, generating inverted radial surface currents at intervals of T_i = 132s, and combined to form the necessary current time series to operate the Q-Factor. Fig. 3.5 presents the time series of radially inverted currents from the northernmost cell in every third spatial band from Fig. 3.6, taken at every 33 s as opposed to the 132 s intervals used for algorithm operation. Fig. 3.10 shows time series of $q(t)$ values computed over groups of spatial bands for Julian day 238, located at radial distances r_b from the radar and with averaged depth shown in Fig. 3.7. Results are arranged in four sub-figures, from the far to the near ranges.

Assuming a q value threshold of 500, the earliest detection occurs at 110 min (or 1h50' into the event) for bands in the 39-45 km and 36-42 km ranges (Fig. 3.10a), with detection occurring later for bands located in range groups closer to shore. These additional detections as the range from the radar decreases could serve as a reinforcement of tsunami detection and increase confidence for warning dissemination. Day 238 provided the earliest detection, with other days detecting the tsunami at the same or later times (1h50' to 2h01') (see Figs. 3.18, 3.19, and 3.20 in Appendix for Julian days 200, 227 and 289). In particular for day 289, under strong swell conditions, tsunami detection still occurs but not until 2h01' in the 30 - 33 km and 22.5-27 km ranges from the radar. Tsunami detection is confirmed later at 2h07' in the 21-24 km range.

3.8.2 The near-field SMF tsunami

The comparison was repeated using the same radar data, spatial bands for the Q-factor and wave rays for the TCA, using currents simulated fo the near field SMF tsunami (Fig. 3.2). Figures 3.11a,b show time series of cell or band averaged tsunami radial surface currents $\overline{U}_{tr}(t)$ computed at 9 stations along ray 225 (Fig. 3.2), as used in the TCA-TDA ((Grilli et al., 2017; Guérin et al., 2017)), or along 13 spatial bands (Fig. 3.6), as used in the Q-Factor TDA, respectively. Average depth varies at the 9 stations from $\sim$ 50 - 1400 m and $\sim$ 60 - 180 m at the 13 spatial bands.

As before, the synthetic SMF tsunami radial currents were superimposed over 1h of radar data for 4 days (Julian days 200, 227, 238, and 289 in 2016), using Eqs. 3.9 and 3.10. For the TCA, time shifted signal correlation $\mathcal{C}_{31,23,1}(\tau, t)$ and contrast function $\Gamma_{31,23,1}(t)$ time series were computed along rays 160, 180, 225, and 285 (Fig. 3.2), for $p_0 = 31$, N=23 and $K = 1$, using an integration correlation window $T_c = 900$s. Fig. 3.12 shows an increase in the contrast function $\Gamma_{31,23,1}(t)$

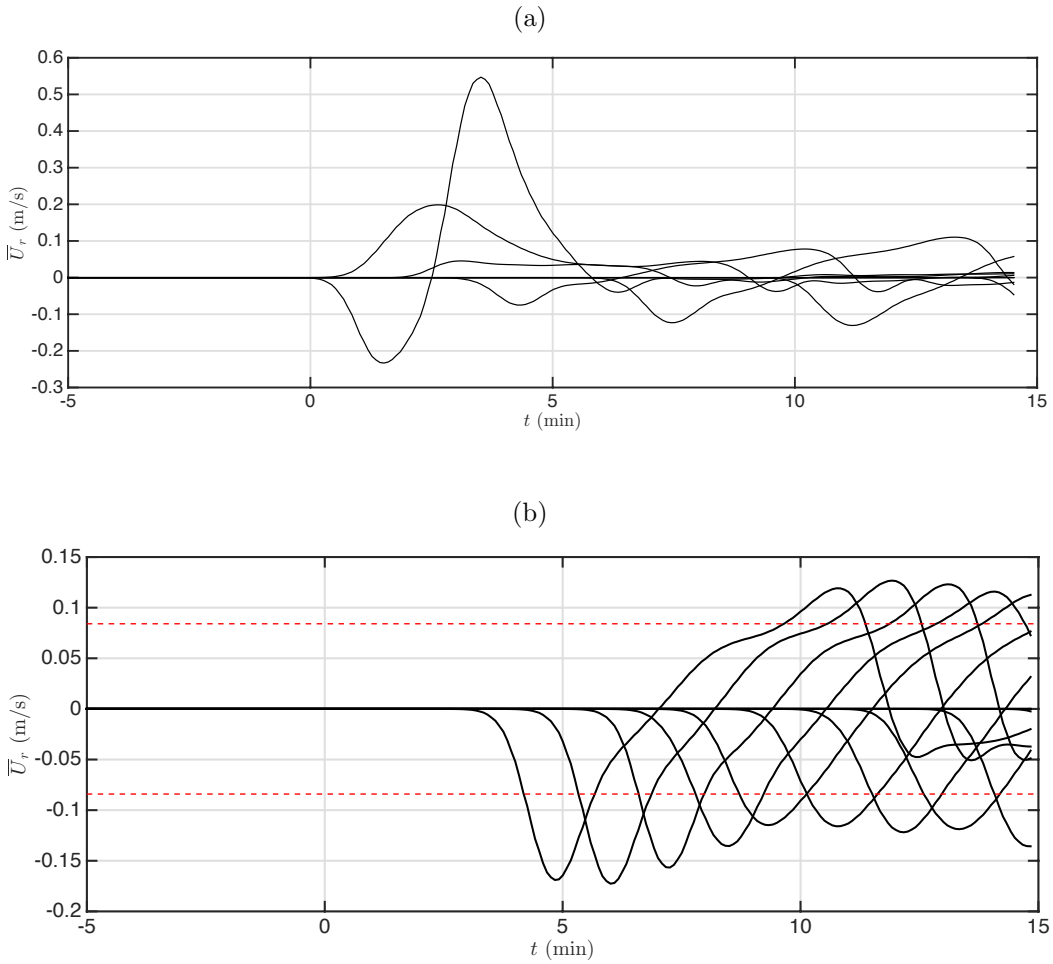

Figure 3.11: Radial currents of the synthetic SMF tsunami: (a) cell-averaged at 9 stations along ray 225 (Fig. 3.2) used in the TCA-TDA (Grilli et al., 2017); and (b) averaged along spatial bands (Fig. 3.6) used in the Q-Factor TDA; dash red lines mark theoretical limits for minimum currents measurable with the Tofino HF WERA radar (~ 0.084 m/s).

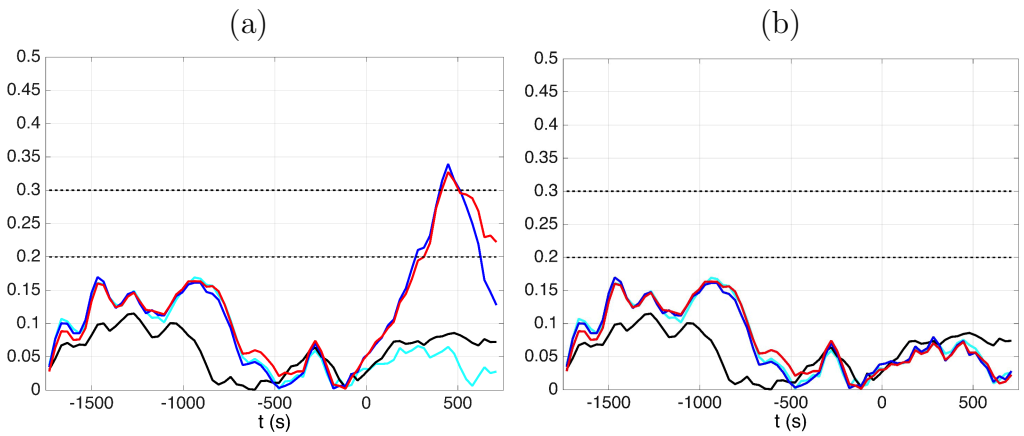

Figure 3.12: Time series of the contrast function $\Gamma_{31,23,1}$ computed as a function of time along rays (Fig. 3.2): (cyan) 160, (black) 180, (blue) 225, (red) 285, for the synthetic SMF source combined with radar data from day 238, with (a) and without (b) a superimposed tsunami; based on a low and high contrast threshold of 0.2 and 0.3, respectively (horizontal dashed lines), a first warning would be issued at 369 s (6 min 9 sec) into the event using rays 225 and 285, and a confirmation of this warning would be issued at 519 s (8 min 39 s).

as tsunami waves propagate through the radar sweep area, whereas without the tsunami no marked increase occurs. Based on a low contrast threshold of 0.2, an initial warning would be issued at 6 min 9 seconds, while a confirmation would be sent at 8 min 39 s.

The Q-factor TDA is applied to the same days of radar data combined with the SMF tsunami radial currents, for the 13 spatial bands of Fig. 3.6, separated in range by 3 to 1.5 km using $T_i = 132$ s. Radial surface currents are again computed using Eqs.3.6 to 3.7. Fig. 3.13 shows time series of $q(t)$ values computed over groups of spatial bands for Julian day 238, located at radial distances r_b from the radar and with average depth shown in Fig. 3.7. No detection occurred, assuming the same q value threshold of 500 as before. It is noted however that the tsunami simulations only propagated through the first 7 bands, corresponding to all of the spatial bands in Fig. 3.13a,b and the first range, 27 - 31.5 km in (c). It is also noted that the remaining ranges of spatial bands, namely in Fig3.13c,d (other than 27

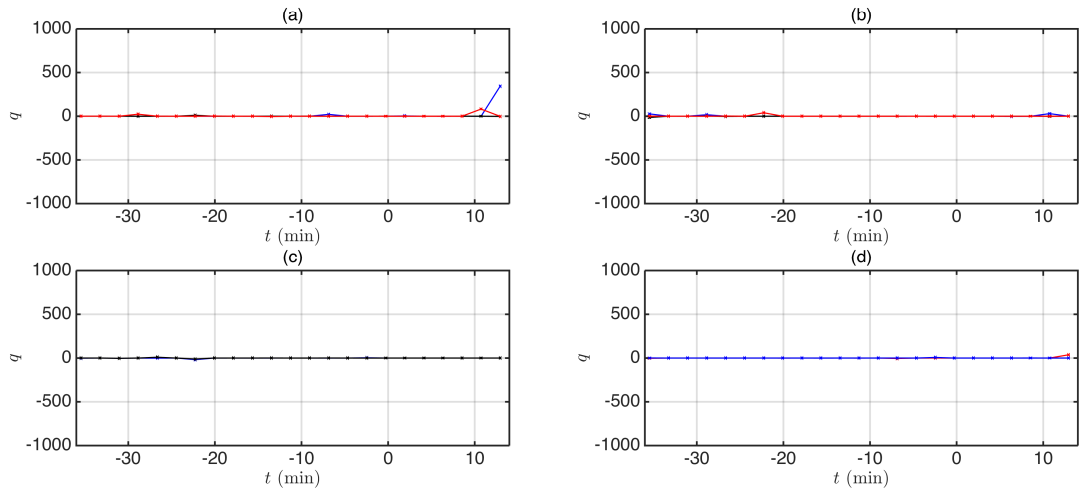

Figure 3.13: Application of the Q-factor TDA to the SMF tsunami. Time series of Q-factor q values for Julian day 238 in 2016, using $T_i = 132$ s and spatial bands located at radial distances from the radar (Figs. 3.6 and 3.7) r_b = (a) 42-48 km (blue), 39-45 km (black), and 36-42 km (red); (b) 33-39 km (blue), 31.5-36 (black), and 30-33 km (red); (c) 27-31.5 km (blue) and 24-30 km (black); and (d) 22.5-27 km (red) and 21-24 km (blue). Due to the nature of this source, tsunami time series were only present in the ranges depicted in (a) and (b); no detection occurred.

- 31.5 km), demonstrated the effective functioning of the Q-Factor TDA, as there was no sign of false alarms.

Currents generated by the near-field SMF are inherently different from those of the far-field SSZ source. The period of generated waves are much shorter due to the SMF generation mechanism, and waves near the source are initially similar to those of a dipole source that generates concentric waves traveling in all directions. The onshore propagating wave train has a leading depression wave and a leading elevation wave of varying magnitude in other directions. The wave train itself is also not immediately well-formed. Even in the near-shore region, which is still quite close to the source, waves are not yet fully refracted and hence do not follow well the expected long-rested long wave behavior that works best with the Q-factor. All of these factors affect the ability of the Q-factor TDA of detecting the SMF tsunami arrival. Fig. 3.14 shows the band-average time series of SMF

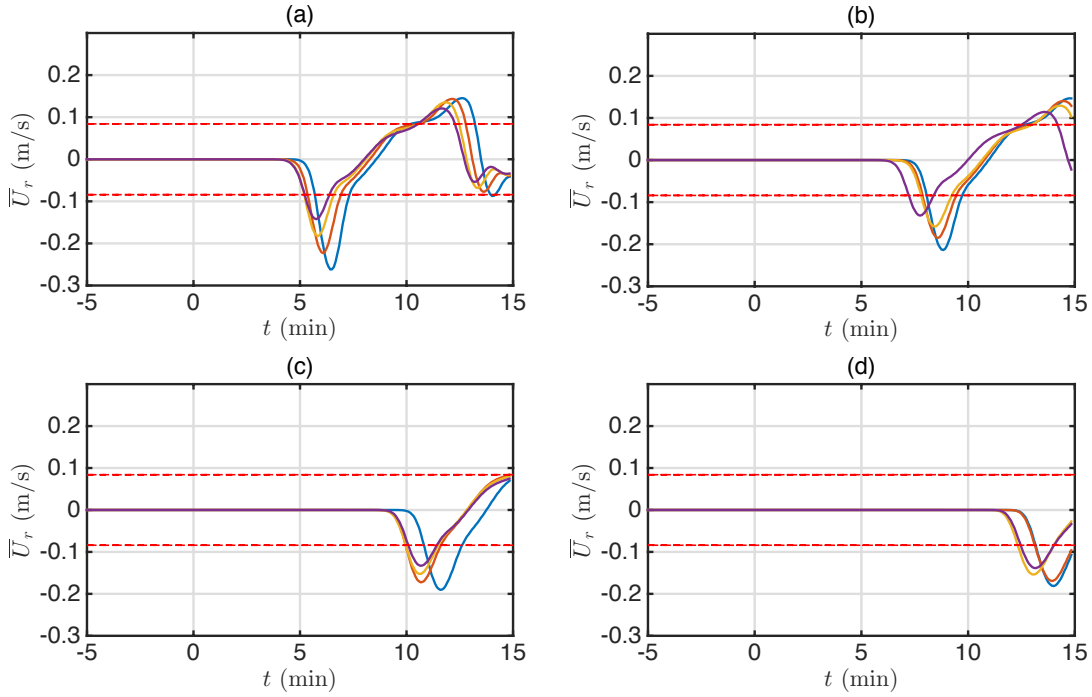

Figure 3.14: SMF tsunami radial currents averaged over 4 spatial bands used in the Q-factor TDA, located at ranges of: (a) 48 km (cell range 30), (b) 42 km (cell range 26), (c) 36 km (cell range 22) and (d) 31.5 km (cell range 19).

tsunami radial current. The time evolution of these currents across each band demonstrates that the wave packet is still evolving, and wave refraction has not yet fully occurred. Fig 3.14a shows currents for the band closest to the source location from Fig. 3.2 and has radial currents of the largest magnitude. Fig 3.14b-d show that currents decrease as the tsunami propagates onshore, due to its spatial spreading. These figures demonstrate the shorter period of the SMF tsunami wave train as compared to the SSZ wave train ($\sim$10 min vs. $\sim$30 min), which also yields a shorter peak current, above the detection threshold, to apply the algorithm. In the presence of such shorter period waves, the Q-factor TDA is much more sensitive to the accurate selection of the integration interval than the TDA.

3.9 Comparison of the TCA and Q-factor TDAs for the offline detection of a potential meteotsunami event

As detailed in Guérin et al. (Guérin et al., 2017), on October 14, 2016 at 6:06' UTC, the WERA HF radar installed in Tofino, whose system was running the standard tsunami detection software developed by Helzel Messetechnik GmbH (DM-TDA based), triggered a tsunami alert, which was attributed to effects of the remnant of typhoon Songda. As noted by (Dzvonkovskaya et al., 2017) long period sea level oscillations of 20 cm amplitude and the propagation of a strong low pressure front (of about 980 milibar) moving at an exceptionally high speed of 95 km/h were recorded by tide gauges and meteorological stations in the Pacific Northwest, near the radar station. The near matching of the speed of the pressure front with that of the long wave velocity on the shelf were indicative of a potential meteotsunami event. More detailed analyses of surface currents during the time of this event lend further support to this conclusion (Guérin et al., 2017). Here we compare the respective abilities of the TCA and Q-factor TDAs to detect this event based on the recorded radar data.

Data from the event was available from 4:00' UTC and 6:58' UTC, as power outages occurred as a result of the storm, which prevented further observations. Rather than using the standard Doppler method inversion, radial currents during this period were inverted using a Bayesian probabilistic method recently developed by the authors to process data originating from phase array systems (Guérin and Grilli, 2017), known as the "Maximum A Posteriori Probability Estimate" (MAPPE). This method was believed to perform better to retrieve currents from this event; details of MAPPE can be found in the referencet. Time series of the radial surface currents were generated along azimuth 70 (Fig. 3.2), at radar ranges 40-41, 30-31, and 20-21 showing large jumps in radial current magnitude by 25-30 cm/s at 96 (5:36' UTC), 110 (5:50' UTC) and 129 (6:09' UTC) min,

respectively (see Fig. 3.21 in Appendix).

Fig. 3.15 shows time series of the TCA contrast functions calculated along the 4 rays shown in Fig. 3.2, which cover the entire sweep area. Three relevant cell intervals were considered, namely for cells 20 to 30 (Figs. 3.15a,b), 30 to 40 (Fig. 3.15c,d) and 40 to 50 (Fig. 3.15e,f). Radar data in each cell within these ranges was correlated with that of its neighboring cell range-ward, yielding 21 correlations pairs ($C_{30-31}, C_{31-32}, ..., C_{50-51}$). Reference correlations were obtained from the same correlations computed one hour in the past. All correlations were computed with an integration window of $T_c = 900$ s. Figs 3.15a,c,e, and Figs 3.15b,d,f show 3 one-hour time series of contrast functions computed for: $\Gamma_{20,11,1}, \Gamma_{30,11,1}, and \Gamma_{40,11,1}$, from 5:00' to 6:00' and 6:00' to 7:00 UTC, respectively. Assuming contrast thresholds of 0.3-0.4 or 0.2-0.4, Fig 3.15 shows that, based on the contrast functions computed on rays 180, 225, and 285 over cells 30-40, a first warning could have been issued by the TCA-TDA at 5:49 UTC (Fig. 3.15c) and confirmed at 5:55' UTC (Fig. 11e). A second alert could have been issued at 6:35' from the increase in the contrast function on rays 160 and 180 over cells 40-50 (Fig. 3.15f) and the entire group of rays over cells 30-40 (Fig. 3.15d).

The Q-factor was then tested on the same data. Fig. 3.16 shows q values computed from 5:00' to 6:00' UTC, which corresponds to the same time series as used in Fig. 3.15a,c,e. By contrast with the TCA, here there is no discernible fluctuation or increase in the q value that could be considered indicative of a tsunami; there are slight increases though but nowhere near the standard threshold q value of 500. The Q-factor was again applied to the next hour of radar time series fromt 6:00' to 7:00' UTC, which corresponds to the same time series as used in Fig. 3.15b,d,f. A q value threshold of 500 was again used as a minimum for detection. Here, an initial detection is demonstrated at approximately 6:08' UTC at range

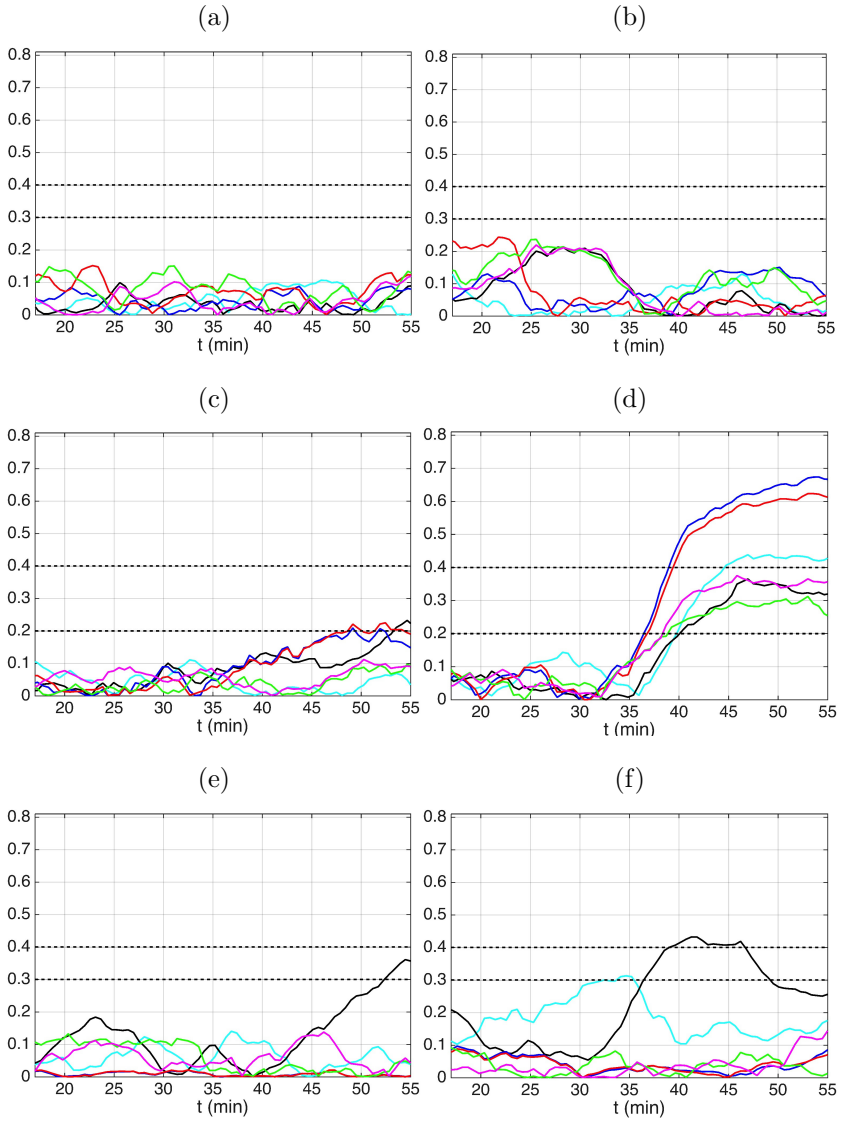

Figure 3.15: Zoom on 1h contrast function time series computed on October 14th, 2016 (day 288) with $T_c = 900$ s (in the past), along rays (Fig. 2): (cyan) 160, (black) 180, (blue) 225, (red) 285, (green) 165 (I) and (magenta) 165 (II). (a) and (b): $\Gamma_{20,11,1}$ (i.e., using the combination of gates (20:30)+1); (c) and (d) $\Gamma_{30,11,1}$; (e) and (f) $\Gamma_{40,11,1}$. The origin of time is 5h 00 min UTC in the leftward column (a, c and e) and 6h 00 min UTC in the rightward column (b, d and f). Arbitrary contrast threshold values have been marked by black dashed lines.

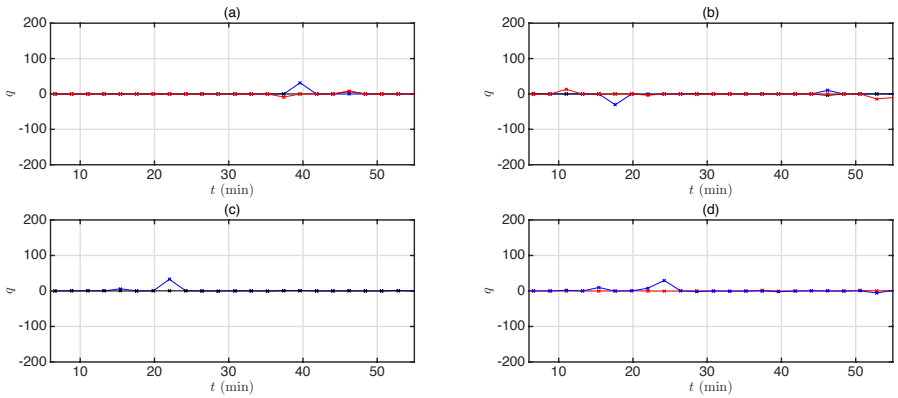

Figure 3.16: Results from applying Q-Factor to the meteorological events of October 14, 2016 (day 288), with the time origin of 5:00' UTC. Same bathymetry bands as Fig. 3.10

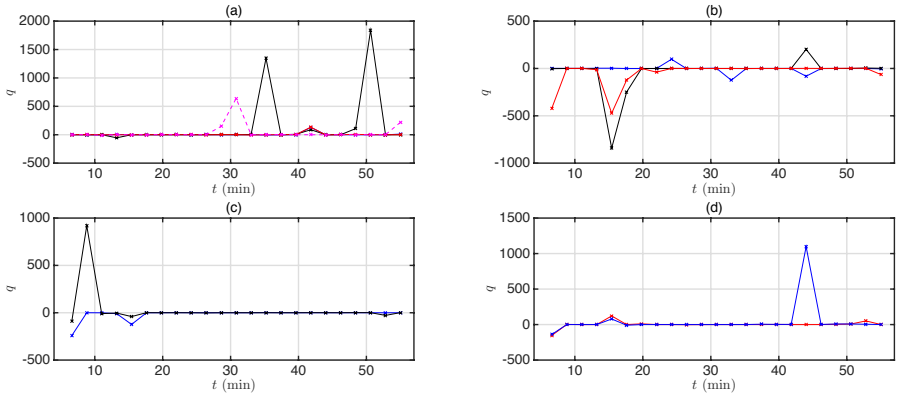

Figure 3.17: Results from applying Q-Factor to the meteorological events of October 14, 2016 (day 288), with the time origin of 6h00 min UTC. Same spatial ranges as Fig. 3.10 except for (a), where 45 - 51 km is included in dashed pink.

24-30 km (Fig. 3.17c), which matches up well with the sudden jump in current calculated using the MAPPE method, in both time and space, as evidenced by the large current increase at ranges 30-31(46.5- 48 km) (Fig. 3.21b) at approximately 6:00' (2 hours after the origin of 4h 00 UTC), and at ranges 20-21 (31.5 - 33 km) at 6h09' (Fig. 3.21c). Detection also occurred at a ranges 51-45 km at 6:31 UTC, 39-45 km at 6:35' and 6:51' (Fig. 3.17a); ranges 31.5-36 km at 6:15' (Fig. 3.17b), and 22.5-27 km at 6:44' (Fig. 3.17d).

3.10 Conclusions

In this study two methods of tsunami detection, the Q-factor and the TCA TDAs were investigated and directly compared on two synthetic and one actual tsunami events. The analysis was done using real radar data recorded from a WERA HF radar station located in Tofino BC,which for the two synthetic tsunamis was combined with realistic synthetic tsunami simulations using a state-of-the-art long wave model. While both methods use a form of pattern recognition derived from a radar signal, their operation is inherently different. The Q-factor uses inverted radial currents derived from the radar signal Doppler Spectra, which is standard procedure in ocean surface current remote sensing, while the TCA-TDA uses a change in pattern of time correlation computed directly on the radar signal. The focus of this comparison is based on detection range, time, and source types, with all three factor driving the development of a detection method that can reach further, issue a warning earlier, and detect any plausible tsunami threat.

Doppler spectra inversion is dependent on the strength of both currents and radar signal, with the measurement resolution function of radar parameters. The TCA-TDA has no clearly established limits in resolution nor on the strength of ocean surface currents and signal. As such, the TCA detection range is not as clear as for the Q-factor. The goal of such methods is to detect tsunamis off the continental shelf, where their currents are weak and can be hidden among environmental noise such as background currents or noise within the radar signal. In earlier work, the authors proposed and showed to some extent that the TCA should perform better in this respect than DM-based TDAs. We aimed here at confirming these properties.

The different tsunami sources compared here represented realistic and variable threats to the area, and were an initial foray into a more thorough and complete

performance versus threat analysis. For the far-field SSZ, we showed that the range and detection time of the two methods was quite similar, given proper sea and atmospheric conditions. The Q-factor algorithm issued a later detection than the TCA for the meteo-tsunami and was unable to detect the SMF tsunami. On the most favorable days the detection time for the TCA-TDA for the SSZ was 1h48' while that of the Q-factor was 1h50'. The Q-factor performed nearly as well as the TCA on days 238 and 200, while it performed less well on days 227 and 289. This indicate as a higher sensitivity of the Q-factor to atmospheric and oceanic conditions, which is related to the need for a relatively strong SNR for accurate current inversion (approximately 6 dB). Additionally the Q-factor needs a wide and shallow continental shelf, which leads to strong currents and sufficient tsunami refraction (for wave crests to align well with bathymetry). Conditions that can yield a weak radar signal are low to nonexistent wind, strong surface attenuation, weak signal emission, or electromagnetic interference, which can come from many different sources. It is not clear to which extent the SNR plays a role on the TCA, but clearly without a sufficiently strong signal the method is expected to perform poorly.

When applied to the SMF tsunami, the TCA-TDA demonstrated detection, while the Q-factor did not. Further inspection of the current time series for individual radar cells across spatial bands demonstrated that the tsunami wave train did not have sufficient time to refract and follow the bathymetry contours in order for the Q-factor to function properly. This shortcoming of the Q-factor makes it preferable for use in detecting far field sources as opposed to near-field tsunamis such as caused by SMFs. Characteristics such as this must be well understood in order to properly choose a detection method in a site specific basis. While the Q-factor was unable to detect an extremely close SMF generated tsunami (with

respect to the radar station), installation at another location with a wider continental shelf, such as on the east coast of the US, may still consider this algorithm as part of a comprehensive warning system. With a wider shelf SMF tsunamis would occur much further from the coastline, giving the tsunami wave train more time to refract and align with bathymetry contours.

Both methods were able to detect the potential meteotsunami event of October 14, 2016. The TCA, however, had an earlier detection time, yielding the conclusion that a lower threshold of 0.2 can be applied as an adequate initial warning threshold. The Q-factor did not detect the meteotsunami with the same regularity in terms of ranges and times, particularly when compared with its performance on the SSZ source. Therefore, in order to incorporate the detection of such an event into a tsunami detection system, algorithms must be adequately robust to false detections, yet sensitive enough to identify the event.

The effect of a strong swell was tested on both methods through the use of signal data measured on Julian day 289. Both methods did experience some interference with the strong swell that hindered their detection capabilities. With the TCA, strong swell interference results most likely from effects of infragravity waves that occur in a well-developed sea state. These waves can have periods of several minutes and, as demonstrated earlier (Grilli et al., 2017), have a visible effect on the TCA contrast function. With the Q-factor, the presence of strong background currents caused by swells and infragravity waves most likely masked the presence of weaker tsunami currents, increasing the overall average background current and making it more difficult for tsunami currents to be identified at farther ranges among the strong sea state. This can be seen in Fig. 3.20, as the detection range is reduced to shallower waters. In the shallower waters, shoaling causes tsunami elevations to grow and in turn currents grow stronger, becoming measurable against

the strong background currents.

Installing each detection algorithm on existing radar systems would include different levels of modifications and specialization of the radar software. The TCA-TDA would need to generate long time series of processed radar data that typically would not be generated or stored in a standard system. The Q-factor would require direct access to the current measurements at frequent intervals, as well as a running history of the current statistics and time series. While neither algorithm would be particularly computationally taxing, their efficient incorporation into radar operations is highly important in governing their overall effectiveness.

3.11 Appendix: Application of TDAs on other days

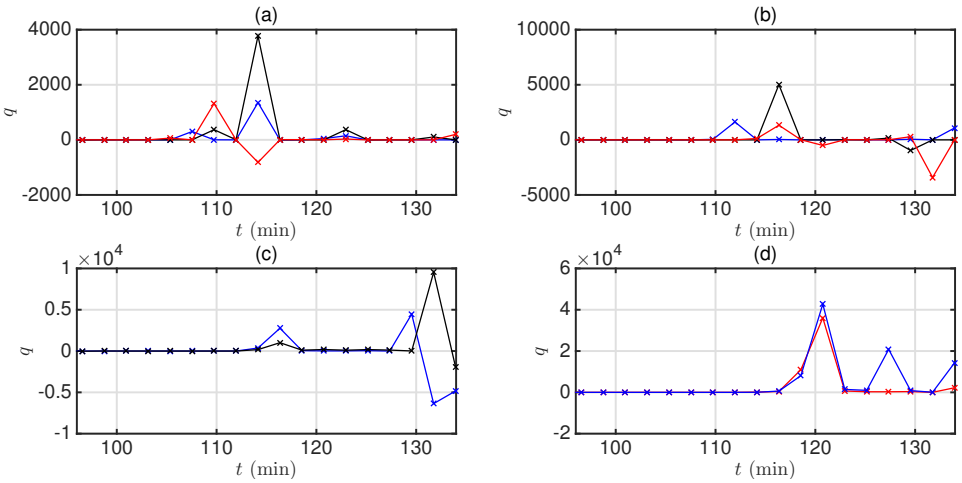

Figure 3.18: Application of the Q-factor TDA to the SSZ tsunami detection. Same results as Fig. 3.10 for day 200.

List of References

Abadie, S., Harris, J. C., Grilli, S. T., and Fabre, R. (2012). Numerical modeling of tsunami waves generated by the flank collapse of the Cumbre Vieja Volcano (La Palma, Canary Islands) : tsunami source and near field effects. *J. Geophys. Res.*, 117:C05030.

Barrick, D. (1979). A coastal radar system for tsunami warning. *Remote sensing of Environment*, 8(4):353 – 358.

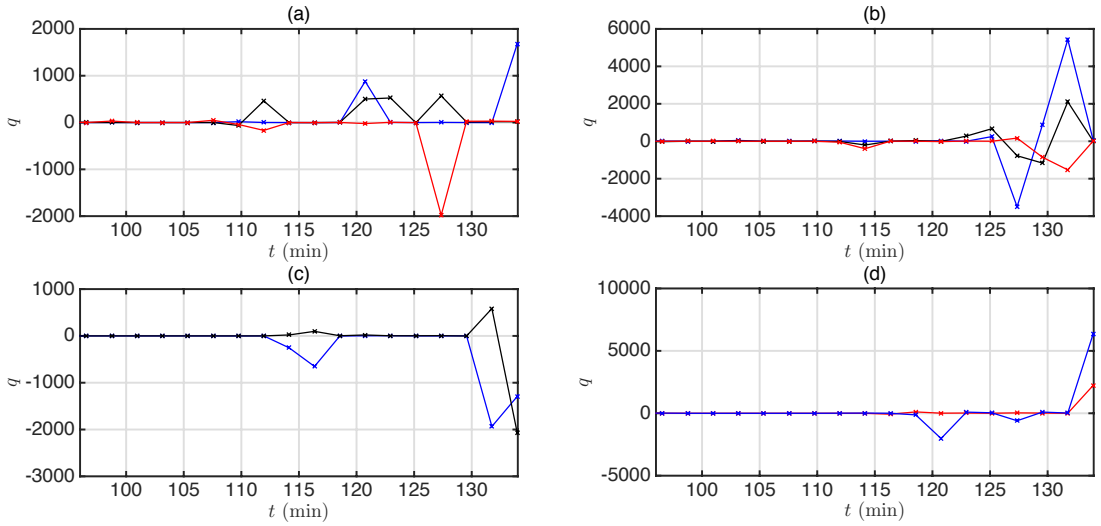

Figure 3.19: Application of the Q-factor TDA to the SSZ tsunami detection. Same results as Fig. 3.10 for day 227.

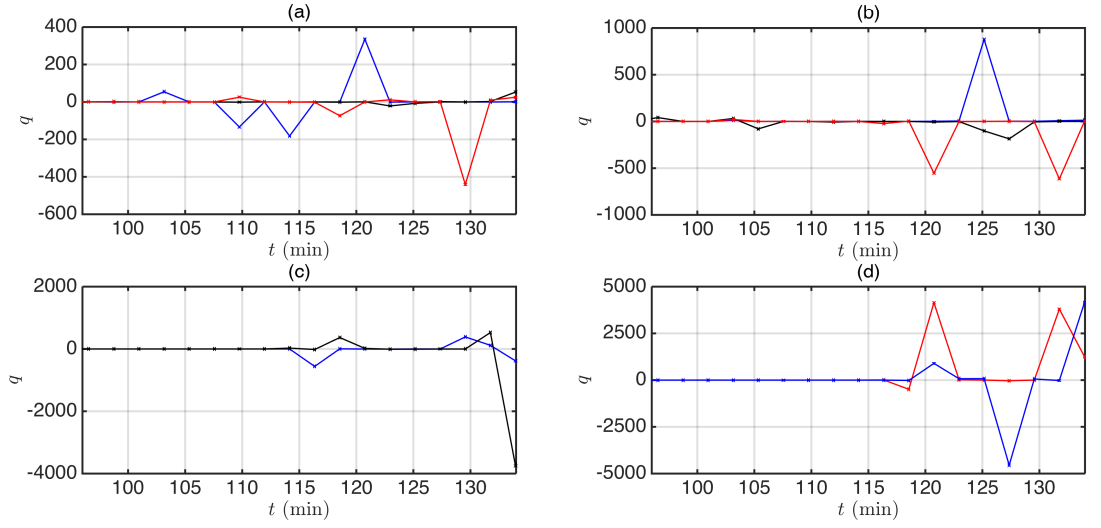

Figure 3.20: Application of the Q-factor TDA to the SSZ tsunami detection. Same results as Fig. 3.10 for day 289.

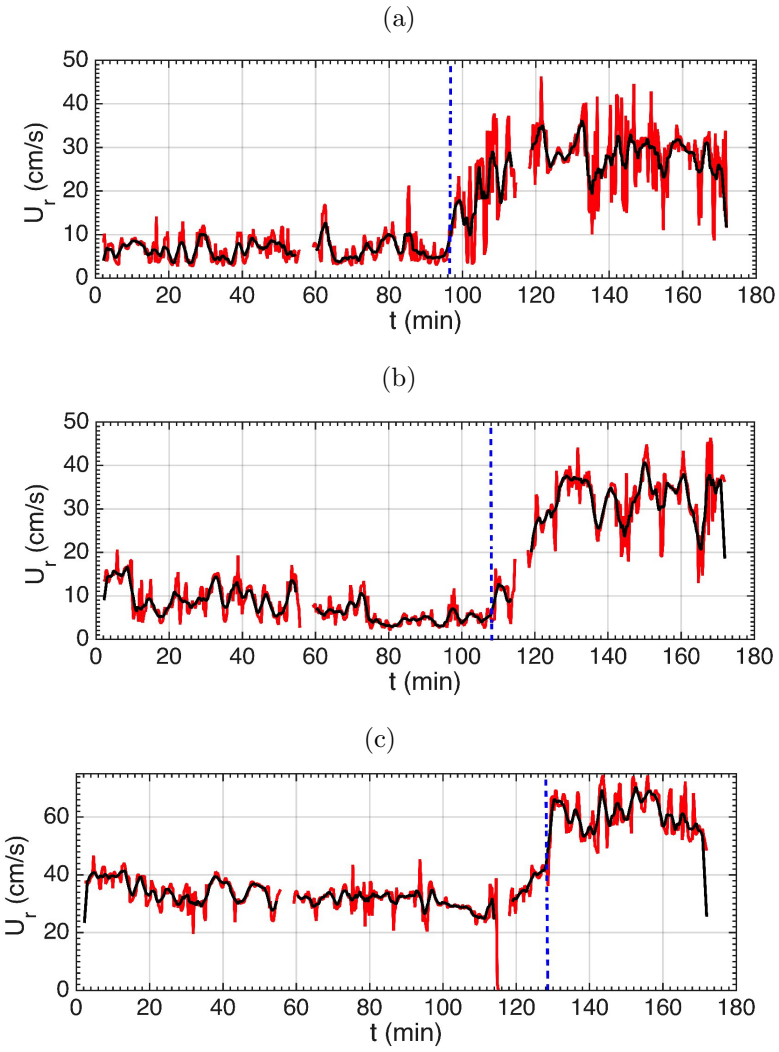

Figure 3.21: Time series of inverted radial surface currents (red lines), and smoothed currents (black lines) computed on October 14th, 2016 (day 288) along azimuth 70 (Fig. 2), averaged over cells/ranges: (a) 40-41; (b) 30-31; and (c) 20-21 (the time origin is at 4h 00 min UTC). Radial currents are estimated every 16 s using the MAPPE method (Guérin and Grilli, 2017), for overlapping intervals of 512 points (133 sec). The occurrence of a jump in current magnitude is clearly visible in figures (a-c), at 96 (5h 36 min UTC), 108 (5h 48 min UTC) and 129 (6h 09 min UTC) min, respectively (marked by a vertical dashed line), which propagates from ranges 40, to 30 and 20.

Barrick, D. E. (1972a). Remote sensing of sea state by radar. In *IEEE International Conference on Engineering in the Ocean Environment, Ocean 72*, pages 186–192. IEEE.

Barrick, D. E. (1972b). Remote sensing of sea state by radar. In *Remote sensing of the Troposphere*, volume 12. VE Derr, Editor, US Government.

Barrick, D. E. (1972c). Remote sensing of the troposphere. *Remote Sensing of Sea State by Radar*, pages 1–46.

Benjamin, L. R., Flament, P., Cheung, K. F., and Luther, D. S. (2016). The 2011 Tohoku tsunami south of Oahu: high-frequency Doppler radio observations and model simulations of currents. *J. Geophys. Res. (publ. online)*, pages 1–29.

Bernard, E. and Titov, V. (2016). Evolution of tsunami warning systems and products. *Phil. Trans. R. Soc. Lond. A*, 373(2053):20140371.

DD, C. Doppler spectrum of sea echo at 13.56 mc/s. *Nature*, pages 681 – 682.

Dean, R. G. and Dalrymple, R. A. (1984). *Water Wave Mechanics for Engineers and Scientists*. Prentice-Hall.

Dzvonkovskaya, A., L, P., and IT, L. (2017). Real-time capability of meteotsunami detection by wera ocaean radar system. page 10, Prague, Czech Republic.

Fine, I., Rabinovich, A., Bornhold, B., Thomson, R., and Kulikov, E. (2005). The Grand Banks landslide-generated tsunami of November 18, 1929: preliminary analysis and numerical modelling. *Mar. Geol.*, 215:45–57.

Grilli, S.T., S. M. K. O. D. G. N. D. M. G. K. J. and Shi, F. (2017). Modeling coastal tsunami hazard from submarine mass failures: effect of slide rheology, experimental validation, and case studies off the us east coast. *Natural Hazards*, 86(1):353–391.

Grilli, S. T., Grosdidier, S., and Guérin, C.-A. (2016). Tsunami detection by High Frequency Radar beyond the continental shelf. I. Algorithms and validation on idealized case studies. *Pure Appl Geophysics*, 173(12):3,895–3,934.

Grilli, S. T., Guérin, C.-A., Shelby, M., Moran, P., Grosdidier, S., and Insua, T. L. (2017). Tsunami detection by High Frequency Radar beyond the continental shelf: II. Extension of algorithms and validation on realistic case studies. *Pure and Applied Geophysics*, 174(1):3,003–3,028.

Grilli, S. T., Harris, J. C., Tajalli-Bakhsh, T., Masterlark, T. L., Kyriakopoulos, C., Kirby, J. T., and Shi, F. (2013). Numerical simulation of the 2011 Tohoku tsunami based on a new transient FEM co-seismic source: Comparison to far- and near-field observations. *Pure Appl Geophysics*, 170:1333–1359.

Grilli, S. T., Ioualalen, M., Asavanant, J., Shi, F., Kirby, J. T., and Watts, P. (2007). Source constraints and model simulation of the December 26, 2004 Indian Ocean tsunami. *J Waterway Port Coastal Ocean Eng*, 133(6):414–428.

Grilli, S. T., O'Reilly, C., Harris, J., Tajalli-Bakhsh, T., Tehranirad, B., Banihashemi, S., Kirby, J., Baxter, C., Eggeling, T., Ma, G., and Shi, F. (2015). Modeling of SMF tsunami hazard along the upper US East Coast: Detailed impact around Ocean City, MD. *Natural Hazards*, 76(2):705–746.

Guérin, C.-A. and Grilli, S. (2017). A probabilistic method for the estimation of ocean surface currents from short time series of HF radar data. *Ocean Modelling*. in revision.

Guérin, C.-A., Grilli, S., Moran, P., Grilli, A., and Lado, T. (2017). Tsunami detection by High Frequency Radar using a Time-Correlation Algorithm: performance analysis based on data from a HF radar in British Columbia. In *Proc. 27th Offshore and Polar Engng. Conf. (ISOPE17, San Francisco, USA. June 2017) (to appear).*

Gurgel, K.-W., Dzvonkovskaya, A., Pohlmann, T., Schlick, T., and Gill, E. (2011). Simulation and detection of tsunami signatures in ocean surface currents measured by HF radar. *Ocean Dynamics*, 61(10):1495–1507.

Heron, M. L., Prytz, A., Heron, S. F., Helzel, T., Schlick, T., Greenslade, D. J., Schulz, E., and Skirving, W. J. (2008). Tsunami observations by coastal ocean radar. *Intl J Remote Sensing*, 29(21):6347–6359.

Hinata, H., Fujii, S., Furukawa, K., Kataoka, T., Miyata, M., Kobayashi, T., Mizutani, M., Kokai, T., and Kanatsu, N. (2011). Propagating tsunami wave and subsequent resonant response signals detected by HF radar in the Kii Channel, Japan. *Estuarine, Coastal and Shelf Science*, 95(1):268–273.

Kirby, S., Scholl, D., Von Huene, R., and Wells, R. (2013). Alaska earthquake source for the SAFRR tsunami scenario. Technical Report USGS Report, 2013, U.S. Geological Survey Open-File . http://pubs.usgs.gov/of/2013/1170/b/, The SAFRR (Science Application for Risk Reduction) Tsunami Scenario.

Lipa, B., Barrick, D., Diposaptono, S., Isaacson, J., Jena, B. K., Nyden, B., Rajesh, K., and Kumar, T. S. (2012a). High frequency (HF) radar detection of the weak 2012 Indonesian tsunamis. *Remote Sensing*, 4(10):2944–2956.

Lipa, B., Barrick, D., and Isaacson, J. (2016). *Tsunami*, chapter Chapter 5: Coastal Tsunami Warning with Deployed HF Radar Systems, pages 73–112. Environmental Sciences. InTech.

Lipa, B., Barrick, D., Saitoh, S.-I., Ishikawa, Y., Awaji, T., Largier, J., and Garfield, N. (2011). Japan tsunami current flows observed by HF radars on two continents. *Remote Sensing*, 3(8):1663–1679.

Lipa, B., Isaacson, J., Nyden, B., and Barrick, D. (2012b). Tsunami arrival detection with high frequency (HF) radar. *Remote Sensing*, 4(5):1448–1461.

Lipa, B. J., Barrick, D. E., Bourg, J., and Nyden, B. B. (2006). HF radar detection of tsunamis. *J Oceanography*, 62(5):705–716.

Lipa, B. J., Barrick, D. E., Diposaptono, S., Isaacson, J., Jena, B. K., Nyden, B., Rajesh, K., and Kumar, T. (2012c). High frequency (HF) radar detection of the weak 2012 Indonesian tsunamis. *Remote Sensing*, 4:2944–2956.

Lipa, B. J., Parikh, H., Barrick, D. E., Roarty, H., and Glenn, S. (2014). High frequency radar observations of the June 2013 US East Coast meteotsunami. *Natural Hazards*, 74:109–122.

Ma, G., Shi, F., and Kirby, J. T. (2012). Shock-capturing non-hydrostatic model for fully dispersive surface wave processes. *Ocean Modeling*, 43-44:22–35.

Monserrat, S., Vilibić, I., and Rabinovich, A. B. (2006). Meteotsunamis: atmospherically induced destructive ocean waves in the tsunami frequency band. *Natural Hazards and Earth System Science*, 6:1035–1051.

Shi, F., Kirby, J. T., Harris, J. C., Geiman, J. D., and Grilli, S. T. (2012). A high-order adaptive time-stepping TVD solver for Boussinesq modeling of breaking waves and coastal inundation. *Ocean Modeling*, 43-44:36–51.

Tappin, D. R., Grilli, S. T., Harris, J. C., Geller, R. J., Masterlark, T., Kirby, J. T., Shi, F., Ma, G., Thingbaijamg, K., and Maig, P. (2014). Did a submarine landslide contribute to the 2011 Tohoku tsunami ? *Marine Geol.*, 357:344–361.

Tappin, D. R., Watts, P., and Grilli, S. T. (2008). The Papua New Guinea tsunami of 1998: anatomy of a catastrophic event. *Natural Hazards and Earth System Sciences*, 8:243–266.

Tehranirad, B., Harris, J., Grilli, A., Grilli, S., Abadie, S., Kirby, J., and Shi, F. (2015). Far-field tsunami hazard in the north Atlantic basin from large scale flank collapses of the Cumbre Vieja volcano, La Palma. *Pure Appl Geophysics*, 172(12):3,589–3,616.

Thomson, R. E., Rabinovich, A. B., Fine, I. V., Sinnott, D. C., McCarthy, A., Sutherland, N. A. S., and Neil, L. K. (2009). Meteorological tsunamis on the coasts of British Columbia and Washington. *Physics and Chemistry of the Earth Parts A/B/C*, 34(17):971–988.

Titov, V., Rabinovich, A., Mofjeld, H., Thomson, R., and Gonzalez, F. (2005). The global reach of the 26 December 2004 Sumatra tsunami. *Science*, 309(5743):2045–2048.